Light-Field Driven Charge and Spin Transfer

Florian Andreas Siegrist

München 2019

Light-Field Driven Charge and Spin Transfer

Florian Andreas Siegrist

Dissertation
an der Fakultät für Physik
der Ludwig–Maximilians–Universität
München

vorgelegt von
Florian Andreas Siegrist
aus Heilbronn

München, den 11.12.2019

Erstgutachter: Prof. Ferenc Krausz
Zweitgutachter: Prof. Markus Münzenberg
Tag der mündlichen Prüfung: 06. Februar 2020

to my parents

"300 Prozent!"

Zusammenfassung

Diese Dissertation erforscht die Wechselwirkung von Licht und Materie mithilfe der Attosekunden-Spektroskopie, die es ermöglicht, die Bewegung von Elektronen in Festkörpern in Echtzeit zu studieren. Diese Untersuchung auf der natürlichen Zeitskala der Elektronendynamik gibt Einblicke in den Ursprung der zugrundeliegenden Effekte, erlaubt deren Verständnis und ermöglicht ihre Kontrolle. Die Steuerung dieser Prozesse ist unter anderem Voraussetzung für die Entwicklung neuartiger optoelektronischer Geräte, die Datenspeicherung und -verarbeitung mit Petahertz-Wiederholraten ermöglichen.

Als zentrales Beispiel wird in dieser Arbeit der magnetische Zustand einer ferromagnetischen Schicht mit zirkular polarisierten Attosekundenpulsen untersucht. Die dadurch erhaltene Spin-Sensitivität ermöglicht erstmals, Magnetisierungsdynamiken mit der außergewöhnlichen Zeitauflösung der Attosekundenphysik zu bestimmen. Diese erstmalige Demonstration von Attosekunden-Zirkulardichroismus als neuer Spektroskopiemethode erlaubt es einen vom oszillierenden elektrischen Feld eines ultrakurzen und intensiven Laserpulses angetriebenen, kohärenten Ladungsträger- und Spintransport über die Grenzfläche eines ferromagnetisch-paramagnetischen Schichtsystems hinweg zu beobachten. Der Abfluss der Spins schwächt das magnetische Moment in der ferromagnetischen Komponente des Schichtsystem ab und führt zu einer effektiven Entmagnetisierung derselben. Diese Änderung des magnetischen Moments wird direkt durch das elektrische Feld des Lichtpulses verursacht, obwohl das elektrische Feld nicht an die Spins der Elektronen koppelt und verläuft damit etwa zwei Größenordnungen schneller ab, als die bisher schnellsten beobachteten Magnetisierungsphänomene.

Ein weiterführendes Experiment untersucht Nanopartikel, die wie hier gezeigt wird trotz ihres Durchmessers von weniger als 10 nm ein magnetisches Moment ausbilden können. Attosekunden-Spektroskopie an Nanopartikeln bietet die Möglichkeit, die beeindruckende Zeitauflösung mit extremer räumlicher Beschränkung zu kombinieren, um zeitaufgelöste Einblicke auf der Nanometer-Skala zu erhalten. Hierfür wird die Absorption der Nanopartikel im statischen Fall sowie in Anwesenheit eines intensiven Laserpulses gemessen und der zeitliche Verlauf der Änderung der elektronischen Eigenschaften und der Besetzungsverteilungen aus der Messung rekonstruiert.

Zum Abgleich der beobachteten magnetischen Änderungen mit der rein elektronischen Materialantwort in Experimenten mit ultrakurzen Laserimpulsen werden Ergebnisse

einer weiteren experimentellen Methode vorgestellt, welche es ermöglicht, die Polarisation eines Mediums mit Petahertz-Abtastraten zu vermessen. Diese Technik wird verwendet, um nichtlineare Effekte in einem Halbleiter zu analysieren, die durch einen ultrakurzen Lichtpuls, der nur aus etwas mehr als einem optischen Oszillationszyklus besteht, hervorgerufen werden. Das Experiment erlaubt es Rückschlüsse auf die elektronische Antwort des Systems und ihre zeitliche Struktur zu ziehen, sowie über den dynamischen Energieaustausch während der Wechselwirkung der Probe mit dem starken elektrischen Feld des Laserpulses. Aufgrund der kleinen Bandlücke von Halbleitern werden vergleichsweise niedrige elektrische Feldstärken benötigt, um nichtlineare Effekte hervorzurufen und die Messung erlaubt erste Einblicke in die Rolle elektronischer Kohärenzen in der Starkfeldpyhsik.

Abstract

This thesis examines the light-matter interaction. Electronic processes are tracked in real-time using attosecond solid state spectroscopy. Understanding and controlling electronic motion on its natural timescale is an essential prerequisite for the creation of a new class of optoelectronic devices, enabling data processing and storage at petahertz clock rates.

This work reports on changing the magnetic moment of matter with unprecedented speed by equipping attosecond transient absorption spectroscopy with spin sensitivity and measuring magnetic circular dichroism in the extreme ultraviolet spectral domain. This novel approach allows for tracking of coherent carrier and spin migration across a tailored multilayer interface, triggered by the strong electric field of a near-single-cycle waveform. The spin transfer leads to a loss of magnetic moment in one of the constituents of the multilayer. This manipulation of the magnetic state of matter is directly driven by the laser pulse, although the electric field of light and spins do not couple to each other.

A closely related experiment studies a series of magnetic nanoparticles, which, despite their size of sub-10 nm can exhibit a magnetic moment. Attosecond spectroscopy of nanoparticles offers the possibility to combine the unique temporal resolution with extreme spatial confinement in order to get time-resolved information on the nanometre scale. The nanoparticles' absorption is recorded for the static case, as well as in the presence of the strong laser field, the temporal evolution of the change of their electronic structure as well as the population distribution is reconstructed from the measurement.

To compare the observed magnetic changes with the purely electronic material response of experiments with ultrashort laser pulses, results from an additional experimental method will be presented. This method allows to sample the polarisation of a medium with Petahertz sampling rates. The technique is used to analyse nonlinear effects in a semiconductor, which are driven by a near-single-cycle light pulse. The measurement of the nonlinear polarisation gives direct access to the response time of the system and the energy transfer dynamics during the strong-field interaction with the medium. Semiconductors are particularly interesting, due to their small band gap, as the field strengths needed to drive nonlinear processes are much smaller and therefore easier

to reach. Additionally the measurement gives first insights into the role of electronic coherence in strong-field physics.

List of Publications and Conference Contributions

Contributions to Peer Reviewed Journals

F. Siegrist, J. Gessner, M. Ossiander, C. Denker, Y.-P. Chang, M. Schröder, J. Walowski, U. Mertens, A. Guggenmos, Y. Cui, U. Kleineberg, J.K. Dewhurst, M. Münzenberg, S. Sharma and M. Schultze, *Light-Field Coherent Control of Magnetism*, *Nature*, **571**, 240, (2019).
I designed and led the experiment, evaluated the data, discussed the results with the collaborators, prepared the figures and contributed to the manuscript.

S. Sederberg, D. Zimin, S. Keiber, **F. Siegrist**, M. Wismer, V. Yakovlev, I. Floss, C. Lemell, J. Burgdörfer, M. Schultze, F. Krausz, N. Karpowicz, *Attosecond optoelectronic field measurement in solids*, *Nature Communications* (accepted).
I performed the attosecond streaking measurement to benchmark the new technique.

O. Razskazovskaya, M. Ossiander, **F. Siegrist**, V. Pervak, M. Schultze, *Carrier frequency tuning of few-cycle light pulsesby a broadband attenuating mirror*, *Applied Optics*, **56**, 89798 (2017).
I performed the measurements and evaluated data.

M. Ossiander, **F. Siegrist**, V. Shirvanyan, R. Pazourek, A. Sommer, T. Latka, A. Guggenmos, S. Nagele, J. Feist, J. Burgdörfer, R. Kienberger, M. Schultze, *Nature Physics*, **13**, 280 (2017).
Together with M. Ossiander I performed the experiment, analysed the data and prepared the figures for the manuscript.

Contributions to Conferences

F. Siegrist, J. Gessner, M. Ossiander, C. Denker, Y. Chang, M. C. Schröder, A. Guggenmos, Y. Cui, J. Walowski, U. Martens, J. K. Dewhurst, U. Kleineberg, M. Münzenberg, S. Sharma, and M. Schultze, *Light-Wave Driven Magnetization Dynamics*, Conference on Attosecond Science and Technology, 2019

J. Gessner, **F. Siegrist**, M. Ossiander, C. Denker, Y. Chang, M. C. Schröder, A. Guggenmos, Y. Cui, J. Walowski, U. Martens, J. K. Dewhurst, U. Kleineberg, M. Münzenberg, S. Sharma, and M. Schultze, *Petahertz Magnetization Dynamics*, Conference on Lasers and Electro-Optics Europe and European Quantum Electronics Conference, 2019

F. Siegrist, A. Sommer, M. C. Schröder, T. Boolakee, K. Golyari, F. Krausz, M. Schultze, *Attosecond energy transfer dynamics in band-gap materials*, SPIE Photonics Europe: Advances in Ultrafast Condensed Phase Physics, 2018

Contents

List of Figures

Chapter 1

Introduction

Modern electronic devices, despite their computational power, still rely on classical charge transport, a fully incoherent process. The rapidly growing field of spintronics, that is often considered an alternate route for future signal processing, relies on incoherent phenomena as well. The lack of coherence leads to charge transport scattering and thus to energy dissipation and heat. which limits the scalability. Decoherence was no problem in the past, where computational power still followed Moore's Law and doubled its potency every two years [1]. However, we currently observe technology reaching fundamental limits, where further downsizing of integrated circuits is no longer possible.

Progress in ultraviolet and extreme ultraviolet spectral regime lithography made transistors with a size of 5 nm [2] possible and might even enable it to go down to 3 nm, as announced by Samsung a year ago [3]. However, classical downsizing is limited when the structure size approaches the interatomic distance, because quantum mechanical effects have to be considered. Another path is enhancing the computational speed of electronics. Computational speed is limited by the dissipated energy that is converted into heat. Without taking additional measures to cool the system, the clock rate of electronic devices is limited to a few Gigahertz.

An entirely new route to faster and more efficient computational devices could be realised by coherent control, where the quantum state of a system is manipulated and exploited. However, the coherent state of a system is fragile: after the excitation by a short laser pulse an electron is in a coherent state. This state, however, is then quickly destroyed by thermalisation or scattering.

Modern day efforts to build quantum computers also rely on the coherent control of entangled quantum states. Only recently, Google reported the successful operation of a quantum computer consisting of a 53 qubit-processor which outperforms state-of-the-art supercomputers, with billions of bits, by orders of magnitude [4]. However, the coherence that is needed for quantum computers is frail, and it takes much effort to protect it from its environment. That is one of the reasons why quantum computing is

still far away from replacing conventional computers. Therefore, the improvement of the existing technology and the development of new approaches is deemed necessary.

The field of spintronics offers a such a novel approach away from conventional charge-based electronics. In spintronic devices not only the electron as a charge carrier holds the information, but also the spin of the electron is relevant. This additional degree of freedom enables a whole new class of devices based on spin-dependent effects resulting from the interaction with the magnetic properties of the components [5]. The field of spintronics was propelled by the discovery of the giant magnetoresistance (GMR) in 1988 [6, 7], which was awarded the Nobel Prize in 2007. GMR showed that a conductor fully capped by a ferromagnetic layer experiences a different resistivity depending on the magnetisation direction of the capping, showing a direct link between the electrons charge and its spin.

It was known long before the discovery of GMR that electricity and magnetism are connected: Hans-Christian Ørstedt discovered a connection between electronic motion and magnetic fields already in 1820. He found that a compass needle changes its pointing direction in the vicinity of a current-conducting wire [8]. This work inspired Michael Faraday for his studies on electromagnetic induction. In 1846 he published his work *"On the magnetisation of light and the illumination of magnetic lines of force"* that describes the rotation of the polarisation of an electromagnetic wave upon transmission through a magnetised medium [9]. Driven by these achievements, James Clerk Maxwell developed his famous equations, which describe classical electromagnetism and the interplay of electric and magnetic fields [10].

More than 100 years later, electromagnetic waves, described by these very equations, were used to change the magnetic state of matter at unprecedented rates [11]. Beaurepaire *et al.* focused a laser pulse on a nickel thin-film and measured the magnetisation using the magneto-optical Kerr effect. This experiment is often considered the cornerstone of modern ultrafast magnetism and was followed by many experiments changing the understanding of ultrafast magnetism [12–16].

Although most experiments focus on bulk materials, interesting ultrafast laser-driven magnetisation dynamics have been seen in a heterostructure [17, 18]. Many demagnetisation processes occurring at interfaces were proposed and experimentally confirmed, such as superdiffusive spin transport [19, 20], spin-transfer-torque switching [21, 22] and spin tunnelling through MgO [23]. Another process, spin accumulation at the interface that leads to demagnetisation, is still debated [24, 25].

One seminal experiment in the context of ultrafast magnetism was the demonstration of all-optical switching [26]. Magnetic bits, without any external magnetic field, were switched by a single laser pulse ($\tau \simeq 40\,\mathrm{fs}$), where the helicity of the light determined the state of the bit. Applying this technique to real-world devices would outperform the speed of any existing memory device.

From a technological as well as from a scientific point of view, the advances in ultrafast magnetism are compelling. Technologically, the knowledge can be used to design devices in which ultrafast all-optical switching is implemented. Scientifically, the underlying physical phenomena that, e.g. determine the switching speed or limit the up-scaling, have to be found. The studies conducted in the field of ultrafast magnetism, despite the numerous breakthroughs, still have not yet entered the attosecond regime, the natural timescale of electron dynamics.

Since its birth, about 20 years ago, attosecond science has allowed the study of electronic motion in atoms, molecules and solids in real-time [27,28]. One of the first achievements was the direct recording of the oscillating electric field of light [29,30]. The new methods were then first applied to scrutinise the dynamics of atomic and molecular systems [31–34]. The first study of the dynamics of a solid-state system was done in 2007, by looking at the photoemission delay of photoelectrons from a surface [35].

At the beginning of this decade, attosecond tools were applied to bulk materials. Transient absorption measurements allow the tracking of electron excitation with attosecond time resolution [36–38]. Complementary to this, high-harmonics from solids give insights into electronic motion in and between valence and conduction bands [39–41]. At the same time, time-dependent density functional theory (TD-DFT) was able to model these systems, due to the accessibility to supercomputers, which are needed to perform the expensive computations. Attosecond spectroscopy, in tandem with TD-DFT, reveals the elementary electronic motion that controls physical properties and processes.

Attosecond spectroscopy and time-resolved magnetic studies are brought together by utilising magnetic circular dichroism (MCD). MCD is typically studied at the characteristic absorption L-edges, however also M-edges exhibit MCD. M-edge absorption of the $3d$ transition metal elements can be probed by XUV light, driving the optical transition from the $3p$ core levels to the $3d$ valence states. These transitions lie in the energy region between $50 - 70\,\mathrm{eV}$, where isolated attosecond pulses from a table-top source can be generated. This enables the study of MCD with the unique temporal resolution of attosecond science.

However, a prerequisite for the detection of MCD is circular polarisation of the probing light. Inspired by an idea that turned XUV synchrotron radiation from linear to circular polarisation, we designed a device for the application on isolated attosecond pulses [42]. A similar device was used before for high harmonic radiation but without temporal characterisation of the radiation and with almost an order of magnitude smaller transmission [43].

Laser light provides coherent light. Together with the ultrashort character of the few-cycle laser pulses, which are a prerequisite for attosecond science, the bursts of light serve an excellent base for coherent control of matter at unprecedented clock rates. Within the scope of this thesis, these ultrashort coherent laser pulses are not only used for coherent control over the spin state of matter but are also be applied to a semiconductor, where they trigger charge-carrier injection. This small band gap material serves as a

prototypical experiment to test coherent excitation and how long the coherent excitation exists.

This work demonstrates for the first time how the oscillating electric light-field can directly manipulate the magnetic properties of a ferromagnetic layer stack. This marks a decrease of magnetic response time of almost two orders of magnitude, entering the regime of attosecond magnetism. The study unveils light-field coherent control of spin dynamics. The manipulation happens in the initial non-dissipative temporal regime and might pave the way towards coherent spintronic applications.

Descriptive Outline

The second chapter gives a brief overview of the theoretical foundation on which this thesis is based. Ferromagnetism, detectable by MCD, is described using the band picture introduced by Stoner. The XUV absorption will be introduced phenomenologically by using Beer-Lambert's law. Afterwards the transition probabilities for the XUV absorption are calculated, as they are needed for the description of the MCD effect. Additionally, sum rules for MCD, which allow the prediction of the spin orbital angular momentum of a magnetic material, will be introduced.

The attosecond manipulation of the magnetic moment of matter is presented in the third chapter. The design of the transmissive waveplate for the XUV, which equips attosecond spectroscopy with spin sensitivity, is introduced. Electronic excitation triggered by the intense laser pulse, enables the measurement of the arrival time of the few-cycle near-infrared laser pulse. The change in XUV transmission allows following electron dynamics in the metal. After that, the sub-femtosecond quenching of the magnetic moment in a ferromagnetic-paramagnetic multilayer sample is presented, and, in addition, a pure ferromagnetic thin-film is manipulated in the same way, not showing sub-femtosecond quenching. The underlying physical effect of optically induced intersite spin transfer is introduced and time-dependent density functional theory is performed to back this up. To get further insights into the demagnetisation process, MCD sum rules are used to track the time evolution of the spin and orbital angular momentum.

The experimental technique introduced in chapter three is then applied to nanoparticles. Three different types of nanoparticles are investigated, all of them containing nickel, which allows the comparison with the bulk-like samples. The nanoparticles' absorption in the absence and presence of a strong external laser field as well as their dichroic behaviour is studied.

In chapter four, light-matter interaction of a semiconductor and an intense laser pulse is discussed. Attosecond polarisation sampling is applied to look at the strong-field response of silicon. This experiment investigates how dissipation-free, coherent control of electrons in a semiconductor can be realized.

Every chapter has a short summary and outlook. A last chapter summarizes the main findings, followed by an outlook on the impact of the results on ongoing and future work and emerging research opportunities.

Chapter 2

Magnetic Circular Dichroism in the Extreme Ultraviolet

A possible way to measure the magnetic moment of a medium and track magnetisation dynamics is magnetic circular dichroism (MCD). This effect is mostly studied in the x-ray regime but can also be observed in the extreme ultraviolet (XUV).
The underlying physical effects that are important for the understanding of MCD are ferromagnetism and XUV absorption. Ferromagnetism is introduced using the band model developed by Stoner. XUV absorption is presented in a phenomenological way first and then treated quantum mechanically. This will give the necessary framework to qualitatively and quantitatively describe the MCD effect afterwards. The last section presents the sum rules for the spin and orbital angular momentum, and their applicability for time-resolved studies at the M-edges.

2.1 Band-Ferromagnetism

Magnetic phenomena were aready observed and described in ancient Greece by Thales of Miletus [44]. The commonly used term of magnetism relates mostly to the effect of ferromagnetism. Ferromagnetic materials exhibit an intrinsic microscopic magnetisation, with different domains, which are arbitrarily oriented. By applying an external magnetic field, these domains align in one direction and lead to a uniform magnetisation of macroscopic extent. Although ferromagnetism has been known for centuries and has been studied intensely, so far, no unified theory exists [45]. One successful way to describe it is band-ferromagnetism, which will be explained in the following.

In general, the response of an object, e.g. an atom or a solid to an external magnetic field, can be expressed by the magnetic moment $\vec{m}$, which describes the strength and orientation. In atoms the magnetic moment $\vec{m}$ is given by integer multiples of the Bohr magneton μ_B $\vec{m} = (2s + l)\mu_B/\hbar$, where s is the spin quantum number, l is the

orbital quantum number, and $\hbar$ is the reduced Planck constant. In the atomic case, this description works, as the electrons are fully localised and fully described by quantum numbers. For example, a nickel atom with the electron configuration, as shown in Fig. 2.1, possesses the spin magnetic moment $m_s = 2\mu_B$. The electron configuration follows Hund's second rule, which states that the total spin of the system is maximised, meaning that the spin of unpaired electrons align parallel.

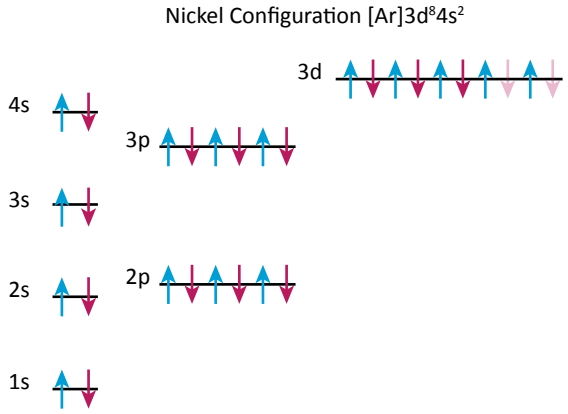

Figure 2.1: The electron configuration of nickel. Following Hund's second rule, in nickel, the two unpaired electrons in the $3d$ state align such that the total spin is maximised, ergo in the parallel direction. The faint arrows indicate the empty states in the $3d$ level. This representation also shows that the electrons from the $3d$ level are responsible for the magnetisation of nickel, as all other states are filled and paired spins do not have a net magnetic moment.

In solids, electrons are not fully localised. Hence the description with quantum numbers is no longer possible. This even holds for deeply bound core electrons. The delocalisation can be seen in the fact that the magnetic moment is no more an integer multiple of μ_B, e.g. for nickel, it is $0.616\,\mu_\mathrm{B}$. The delocalisation is also reflected in the band model of solids that was introduced by Felix Bloch [46].
In the band model, the discrete energy levels of atoms are replaced by a bandstructure. The bands originate from the periodic potential inside a solid and are formed by the allowed energetic states in reciprocal space depending on the wavevector $\vec{k}$. An often-used quantity that is derived from the band structure is the density of states (DOS). For the DOS, the band structure is integrated over all $\vec{k}$-states of the Brillouin zone. This provides the number of available states that can be occupied within a specific energy range.
The band structure model was first applied to describe the properties of magnetic materials by Mott and Slater in the 1930s [47, 48]. Another description was proposed by Stoner a few years later [49]. This model is illustrated here.
A ferromagnetic medium has an intrinsic splitting of the band structure for the spin-

up and the spin-down states without an external magnetic field, as it is energetically beneficial for the system, as illustrated in Fig. 2.2.

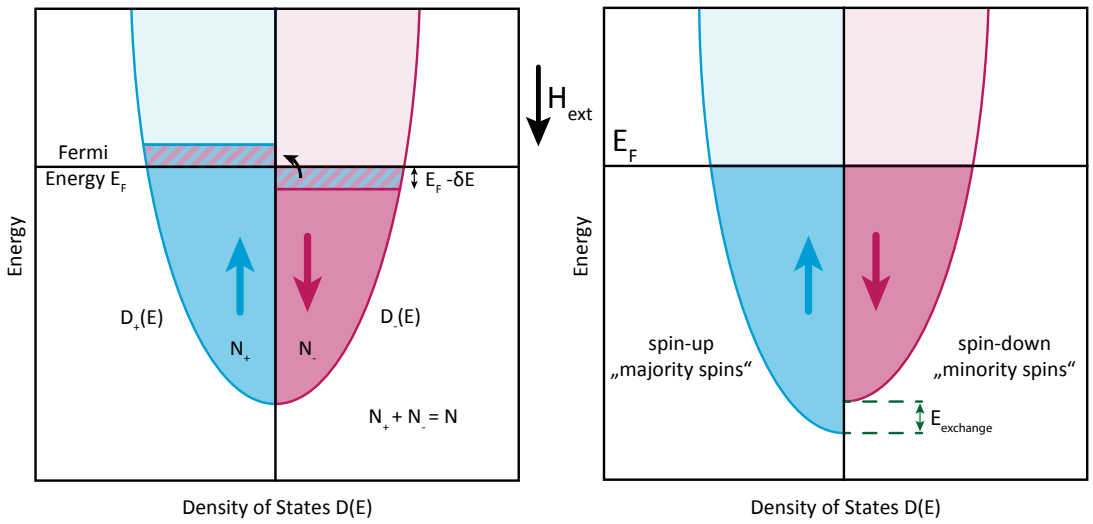

Figure 2.2: Both panels show the energy dependent DOS, for spin-up and spin-down. The left panel illsutrates the origin of band-ferromagnetism. Initially the DOS is the same for spin-up and spin-down $D_+ = D_-$. Therefore, also the population is the same. Then one electron changes its spin and the population changes by $D(E_F) \cdot \delta E$ (striped area). The calculations show that this can be energetically beneficial for the system. The splitted bands in a ferromagnet are illustrated in the right panel. The population number of spin-up electrons is larger than spin-down, this gives them the name *majority* spins and *minority* spins. The magnetic moment of the ferromagnet aligns with the external magnetic field. The magnetic moment is antiparallel to the majority spins. The levelling at the Fermi Energy leads to a difference in unoccupied states and an energy offset, called exchange energy E_{exchange} (dashed green line). The external field is not necessary for the band splitting to happen. However, the external field aligns the spins and leads to an unidirectional macroscopic magnetisation.

In a system where there is no intrinsic magnetisation, the density of states $D_\pm$ for the spin-up (+) and spin-down (-) are the same, and they level at the Fermi Energy.

$$\begin{aligned} D_+(E_F) &= D_-(E_F) \\ N_+ &= N_- \end{aligned} \tag{2.1}$$

Now consider that one electron from the spin-down side changes its spin direction. This modifies the occupation and is described by:

$$D_+(E_F)\delta E = \frac{1}{2} D(E_F)\delta E, \tag{2.2}$$

with D the total density of states and δE being the energy that the spin-up side gained. As all states up to the Fermi energy are occupied, the electron that changed its spin state has higher energy. This leads to an increase in the kinetic energy of the system that is equal to:

$$\Delta E_{kin} = \frac{1}{2} D(E_F) \delta E \delta E. \tag{2.3}$$

At the same time, the parallel alignment of the spins leads to a decrease in potential energy. A mean-field is created by the magnetic field of the residual electron spins. This mean-field generates a magnetisation, which can be calculated and is attributed to the difference of the number of spin-up and spin-down electrons. The mean-field can be expressed as $B = \lambda \mu_0 M$, where λ is a parameter for the strength of the mean-field, μ_0 the vacuum permeability and M the magnetisation. Moreover, the magnetisation can be expressed in terms of the difference of the spin-dependent electron densities $N_{\pm}$.

$$\begin{aligned} M =& \mu_B \Delta N = \mu_B (N_- - N_+) \\ =& \mu_B \left(\frac{1}{2} N + \frac{1}{2} D(E_F) \delta E - \frac{1}{2} N + \frac{1}{2} D(E_F) \delta E \right) \\ =& \mu_B D(E_F) \delta E = \frac{1}{\lambda \mu_0} B. \end{aligned} \tag{2.4}$$

From thermodynamics it is known that the free energy F is given by $F = U - TS$ and that it relates to the magnetisation through $\mathrm{d}F = -M \mathrm{d}B$ [50]. Here U is the potential energy, T the temperature of the system and S its entropy. Assuming no change of the second term of the free energy, the gain or loss of the potential energy can then be calculated by:

$$\Delta E_{pot} = -\int_0^M M' \mu_0 \lambda \mathrm{d}M' = -\frac{1}{2} \mu_0 \lambda M^2 = -\frac{1}{2} U D(E_F) \delta E^2 \tag{2.5}$$

with the strength of the mean-field $U = \mu_0 \mu_B^2 \lambda$. The total change of energy is given by:

$$\begin{aligned} \Delta E =& \Delta E_{kin} + \Delta E_{pot} = \frac{1}{2} D(E_F) \delta E \delta E - \frac{1}{2} U D(E_F) \delta E^2 \\ =& \frac{1}{2} D(E_F) \delta E^2 (1 - U D(E_F)). \end{aligned} \tag{2.6}$$

This describes the change of energy of the system caused by a spin flip. For $\Delta E \leq 0$ the energy of the system will be reduced or remain the same. This means it is beneficial for for system, that one electron changes its spin and causes an imbalance of spin-up and spin-down electrons. As this is the requirement for ferromagnetism, a criterion can be derived so that $\Delta E \leq 0$ is true:

$$U D(E_F) \geq 1. \tag{2.7}$$

This is known as the *Stoner criterion*. The derivation above describes the origin of the band splitting in ferromagnets.

The Stoner band splitting is illustrated in Fig. 2.2. The situation at $T = 0\,\mathrm{K}$, where all states up to the Fermi Energy E_F are filled, is shown. The terms *majority* and *minority* become clear when looking at the the right panel of the figure. More spin-up states are populated, giving them the name *majority* and respectively the spin-down are named *minority* carriers. The orientation of the magnetic moment is opposite to the majority spin alignment $\vec{m}_s = -g\mu_B\vec{s}$, this means that the external magnetic field is also antiparallel to the majority spin direction. As the DOS of minority and majority carriers differ also their number of unoccupied states above the Fermi Energy is different. This is one of the reasons for the appearance of MCD.
While the understanding of the Stoner model is intuitive, it is also incomplete as it only looks at the DOS and ignores the $\vec{k}$-dependence of the bandstructure. For a qualitative description and the basic understanding of ferromagnetism and later MCD, it is sufficient.

2.2 XUV Absorption

A phenomenological way to describe frequency-dependent absorption of an electromagnetic wave inside a medium is the Beer-Lambert law; it is illustrated in the left panel of Fig. 2.3. The intensity I_0 of the impinging electric field decays exponentially inside the medium. The strength of the attenuation is given by the absorption coefficient μ. The frequency-dependent transmitted intensity $I(\omega, z)$ after a medium of length z is:

$$I(\omega, z) = I_0(\omega)e^{-\mu(\omega)z}, \tag{2.8}$$

where ω denotes the angular frequency of the oscillating electric field. The element-specific absorption coefficient has the unit of [1/length]. Beer-Lambert's law is a simple model, however, widely applicable.
The light-matter interaction can also be described in terms of the dimensionless complex refractive index. This description is valid for the whole range of the electromagnetic spectrum and is dependent on the frequency ω. Here, the following form is used:

$$n(\omega) = 1 - \delta(\omega) + i\beta(\omega), \tag{2.9}$$

where $\delta(\omega)$ denotes the frequency-dependent real part of the complex refractive index, which is attributed to refraction, while $\beta(\omega)$ is the imaginary part that describes the absorption. This notation is commonly used in x-ray spectroscopy, in the visible range usually the notation $n = \tilde{n} + i\kappa$ is used, where $n > 1$ is the real part and κ the absorptive imaginary part. This description explains not only the absorption, but also an induced phase shift between the unperturbed and the transmitted electromagnetic wave. For non-isotropic media, the polarisation state of the electromagnetic wave can also influence the light-matter interaction, leading to effects such as *birefringence* and *dichroism*. The first is caused by a polarisation-dependent real part δ, the latter by a polarisation-dependent imaginary part β.

The attenuation coefficient relates the intensity of an electromagnetic wave that enters a medium to the transmitted intensity and the medium's length. It is also possible to

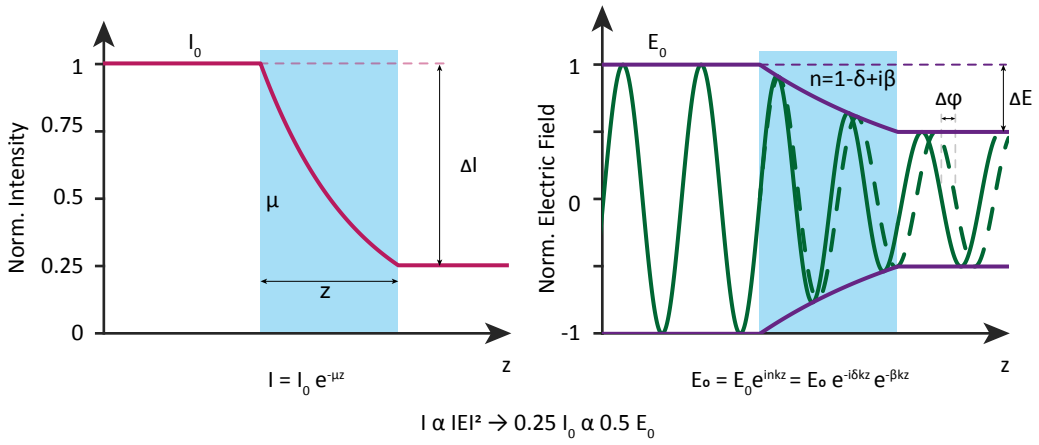

Figure 2.3: The left panel illustrates Beer-Lambert's law. A monochromatic electromagnetic wave with intensity I_0 is transmitted through a medium (blue) with a characteristic absorption coefficient μ. The attenuation of the wave is given by $I(z) = I_0 e^{-\mu z}$ where z is the propagation length inside the medium. The same light-matter interaction can also be described in terms of the electric field of the electromagnetic wave and the complex refractive index $n = 1 - \delta + i\beta$. In this description, not only the absorption, but also the phase evolution of the electromagnetic wave, caused by the real part of the refractive index, is described. The amplitude of the oscillating electric field inside the medium is attenuated (purple line), and the oscillation appears at smaller wavelength inside the medium (green line) compared to the same wave in vacuum (dashed green line), which leads to a phase shift $\Delta\varphi$ at the exit of the medium. The attenuation introduced by the medium is equal in both cases.

define an absorption cross-section, which is a measure for the probability for a photon of a certain energy to be absorbed within a specific length inside a medium. The number of photons $\mathrm{d}N$ which is absorbed within a length $\mathrm{d}x$ is given by

$$\frac{\mathrm{d}N}{\mathrm{d}x} = -Nn\sigma \tag{2.10}$$

where σ is the absorption cross-section, N is the number of impinging photons, and n is the number of absorbing atoms in the penetrated volume.
In a more descriptive way, the absorption cross-section can be expressed in the following way:

$$[\sigma_{abs}] = \left[\frac{\#\text{ absorbed photons} \times \text{illuminated area}}{\#\text{ incident photons} \times \#\text{ atoms}}\right] = \frac{\text{length}^2}{\text{atom}}. \tag{2.11}$$

The attenuation coefficient describes the ratio of absorbed photons, incident photons and the atoms in the volume. The density is given by the atomic number density ρ_A. So, in other words, the absorption cross-section is the quotient of the attenuation coefficient

and the atomic number density, which give the number of atoms in a specified volume. Moreover, the atomic number density can be expressed in terms of the mass density ρ_m, Avogadro's constant N_A and the molar mass A:

$$\sigma_{abs} = \frac{\mu}{\rho_a} = \frac{A}{N_A \rho_m}\mu. \tag{2.12}$$

To relate the absorption cross-section and the absorption coefficient with the complex refractive index, it is used that:

$$I \propto |E|^2 \tag{2.13}$$

As depicted in Fig. 2.3, the modified electric field after the interaction with the medium can be written as:

$$E = E_0\ e^{inkz} = E_0\ e^{-i\delta kz}\ e^{-\beta kz}, \tag{2.14}$$

where E_0 is the amplitude of the incident electric field, the second term is the phase shift due to the real part of the refractive index, and the last term is the absorption induced by the imaginary part.
With Eq. (2.13) the square modulus of the electric field can be related to the intensity:

$$|E|^2 = |E_0|^2 e^{-2\beta kz} \propto I \tag{2.15}$$

The comparison of Eq. (2.8) and (2.15) gives a direct relation between the complex part of the refractive index and the linear absorption coefficient:

$$\beta = \frac{\mu}{2k} = \frac{\rho_a}{2k}\sigma_{abs} \tag{2.16}$$

with k being the wavevector $k = 2\pi/\lambda$.

Absorption, the optical transition between an initial and a final state, can not only be treated classically but also quantum mechanically. In the quantum mechanical approach the polarisation state of the electric field manifests directly in the expressions. A modified version of Fermi's Golden Rule gives the transition rate from an initial state $|i\rangle$ to a final state $|f\rangle$ upon absorption of a photon with energy $\hbar\omega$:

$$I_{i\to f} = \frac{2m}{\hbar}\frac{(E_f - E_i)^2}{\hbar\omega}|\,\langle f|\vec{e}\cdot\vec{r}|i\rangle\,|^2 \tag{2.17}$$

here $\vec{r}$ are the electron's coordinates, while $\vec{e}$ is the polarisation vector of the driving photon, $E_f - E_i$ gives the energy difference between initial and final state. The scalar product $\vec{e}\cdot\vec{r}$ already indicates that the polarisation state of the photon plays a role in the transition. A second order term, which describes transitions through intermediate states, is neglected, as these transitions are unlikely and not studied in this work.
Using Cartesian coordinates the normalized electric field vector for a right circular polarised photon is given by $\vec{e} = -1/\sqrt{2}(\vec{e}_x + i\vec{e}_y)$, for a left polarised photon $\vec{e} = 1/\sqrt{2}(\vec{e}_x - i\vec{e}_y)$ respectively. This simplifies Eq. (2.17) to:

$$I_{i\to f} = \frac{2m}{\hbar}\frac{(E_f - E_i)^2}{\hbar\omega}|\,\langle f|x \pm iy|i\rangle\,|^2 \tag{2.18}$$

The dipole operators can be expressed in terms of Racah's spherical tensors [51]. The spherical tensors $C^{(l)}_{ml}$, can be further decomposed into spherical harmonics $Y_l^{m_l}(\theta, \phi)$, with $l = 1$ and $m_l = \pm 1$ due to the photon spin.
This leads to the dipole operators P in terms of spherical harmonics with the quantum numbers l and m_l.

$$P_1^{(1)} = \frac{1}{\sqrt{2}}(x + iy) = rC_1^{(1)} = r\sqrt{\frac{4\pi}{3}}Y_1^1 \tag{2.19}$$

$$P_1^{(-1)} = \frac{1}{\sqrt{2}}(x - iy) = rC_1^{(-1)} = r\sqrt{\frac{4\pi}{3}}Y_1^{-1} \tag{2.20}$$

With the dipole operators it is now possible to calculate the polarisation dependent transition intensities from an initial state $|i\rangle$ to a final state $|f\rangle$.

2.3 Magnetic Circular Dichroism

The description of the MCD effect combines the Stoner model and x-ray absorption. First, a quantum mechanical approach is chosen to calculate transition probabilities, afterwards a model is introduced the illustrates that MCD effect - the so-called two-step model.

Quantum Mechanical Description

The magnetic circular dichroism can be calculated from the transition probabilities, between an initial state $|i\rangle$ and a final state $|f\rangle$. In the case of $M_{2,3}$-edge absorption, the transition happens between states of the spin-orbit split $3p$ level and the $3d$ valence states. In this discussion, the magnetisation of the sample is chosen parallel to the spin-up direction. Moreover, right-handed polarisation has helicity +1, while left-handed polarisation has helicity -1. For the qualitative description, it is convenient to use a one-electron picture, where only one vacancy in the $3d$ level exists, see the upper panel of Fig. 2.4. In the case of a magnetic field parallel to spin-down, this vacancy has spin-down. The assumption of only one vacancy simplifies the calculations. This description is the atomic equivalent to the Stoner picture and the band splitting [52].

As all spin-up states are occupied, the respective band picture shows no vacancies above the Fermi energy, on the contrary there is one vacancy for the spin-down state. Note that the two green circles in Fig. 2.4 only indicate that electrons from both core levels can occupy that state, it does not say anything about the number of empty states.
As this description uses an atomic approach, quantum numbers can be used for the description of the electronic states. In this one-electron picture the transitions happen from the $3p_{1/2}$ and the $3p_{3/2}$ state to the $3d$ valence states. The $3d$ states are degenerate and the hole can be in any of the states ($m_l = -2, -1, 0, 1, 2$), therefore the transition probability has to be calculated to each of these states and then averaged.
Transitions are calculated using the wavefunctions in the $|l, m_l, s, m_s\rangle$ basis. As the

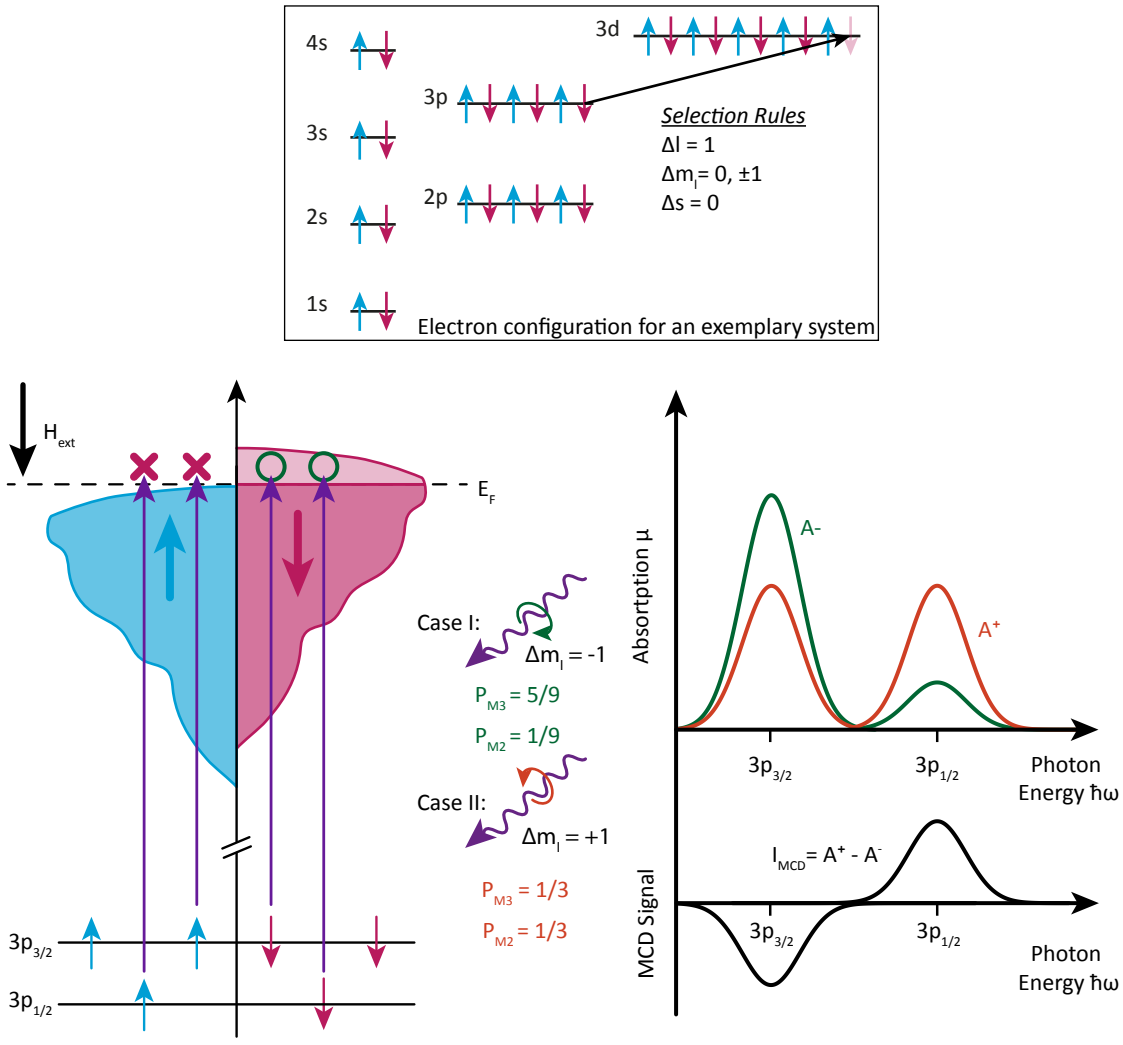

Figure 2.4: Top: Exemplary system, with only one vacancy. This electron configuration is considered for the calculations of the transition probabilities. The lower part of the figure illustrates the MCD effect. Left panel: The two-step model. Circularly polarised light excites electrons independent of their spin direction or core level. Depending on whether there are empty states above the Fermi Energy E_F (indicated by red crosses, no empty states and green circles, empty states), the excitation can happen. From this, the resulting transition probabilities can be calculated. Right panel: the absorption for the two cases. The resulting MCD signal here is shown below and is symmetrical, however, due to final state selection rules, the actual MCD signal is not symmetrical, but has larger amplitude at lower photon energy.

dipole operator does not act on m_s and s, only the angular part of the transition matrix element will be considered. The initial and final states have the same n, m_s and s and can therefore be simplified to:

$$|i\rangle = |l, m_l\rangle \tag{2.21}$$

for spin-up:

$$|f\rangle = |n, l+1, m_l+1\rangle \tag{2.22}$$

and for spin-down:

$$|f\rangle = |l-1, m_l-1\rangle \tag{2.23}$$

The dipole operators for the transitions were derived in the previous section 2.2, Eq. (2.19) and Eq. (2.20).
Putting all the above together, one can calculate the strength of the optical oscillator driving transitions between the initial and final state for the spin-up electrons:

$$\langle n, l+1, m_l+1|P_1^{(1)}|n, l, m_l\rangle = -\sqrt{\frac{(l+m_l+2)(l+m_l+1)}{2(2l+3)(2l+1)}}R \tag{2.24}$$

and for spin-down electrons:

$$\langle n, l+1, m_l-1|P_-^{(1)}1|n, l, m_l\rangle = -\sqrt{\frac{(l-m_l+2)(l-m_l+1)}{2(2l+3)(2l+1)}}R. \tag{2.25}$$

Here the work from Bethe and Salpeter was used to evaluate the matrix elements [53]. The radial matrix element R, the integral over the overlap of the initial and final state wavepacket, is assumed to be constant for all transitions, as the wavepackets for all the spin split states are assumed to be the same.
From the oscillator strengths it is also straightforward to show that switching the magnetisation is equivalent to changing the polarisation direction of the light source.

$$\langle n, l+1, -m_l+1|P_1^{(1)}|n, l, -m_l\rangle = \langle n, l+1, m_l-1|P_{-1}^{(1)}|n, l, m_l\rangle \tag{2.26}$$

This is important for the experiment as switching the magnetisation can be realized much more easily.
General selection rules for dipole transitions are $\Delta l = \pm 1$ and $\Delta m_l = 0, \pm 1$. The discussion only considers $p \to d$ as they are 20 times more likely, meaning that $p \to s$ i.e. $\Delta l = -1$ is excluded [52]. The convention used is that right-handed circular polarisation has $m_l = +1$ and left-handed circular polarisation has $m_l = -1$. Linear polarisation is equivalent to $\Delta m_l = 0$ and is not considered.
In the simplified one electron picture all spin-up states are occupied and only one spin-down state is empty (see Fig. 2.4). Thus, only transitions of spin-down electrons have to be considered and only the spin-down wavefunctions have to be evaluated. Starting from the p orbital with spin-down electrons, the wavefunctions are given by:

$$|i\rangle = a_{m_l}\left|l = 1, s = \frac{1}{2}, m_l, \beta\right\rangle = a_{m_l}Y_l^{m_l}\beta, \tag{2.27}$$

where a_{m_l} are coefficients to normalize the wavefunctions, the coefficient can be found here [52]. β represents the spin-down part of the wavefunction.
For the final d states 5 spin-down wavefunctions are used and the spin-orbit splitting is neglected as it has no influence on the result. They then take the form:

$$|f\rangle = \left| l = 2, s = \frac{1}{2}, m_l, \beta \right\rangle = Y_2^{m_l}\beta, \tag{2.28}$$

with the values for the magnetic quantum number m_l ranging from $-l$ to l. The strength of the transition can be calculated by:

$$I_{M_k}^{\pm} = \sum_{i,f} |\, \langle f|P_{\pm 1}^{(1)}|i\rangle \,|^2, \tag{2.29}$$

with the sum over all initial states i and final states f, where $k = 2, 3$ and ± 1 indicates the helicity of the photon or the direction of magnetisation, as demonstrated above. The calculation gives the following transition probabilities from the $3p_{3/2}$ core level to the $3d$ valence states:

$$A_{3p_{3/2}}^{+} = \frac{1}{3}R^2; \qquad A_{3p_{3/2}}^{-} = \frac{5}{9}R^2 \tag{2.30}$$

and for the transition from the $3p_{1/2}$ core level:

$$A_{3p_{1/2}}^{+} = \frac{1}{3}R^2; \qquad A_{3p_{1/2}}^{-} = \frac{1}{9}R^2. \tag{2.31}$$

The transition probabilities are also written in the right panel in Fig. 2.4. The strength for the optical transition from $3p_{3/2}$ and $3p_{1/2}$ driven by right circular light is the same, for left circular light it differs.
This result gives the strength of the optical transition. Band ferromagnetism and XUV absorption were put together to arrive at this point and now allows the calculation of the dichroic signal. The dichroism is defined as $I_{\mathrm{MCD}} = A^{+} - A^{-}$, where $A^{\pm}$ are the absorptions for opposite helicities. They can also denote the absorption for reversed magnetisation of the medium while keeping the helicity the same. Calculating the dichroism separately for the two spin-orbit split initial states, gives the following:

$$I_{\mathrm{MCD}}^{M_3} = -\frac{2}{9}R^2 \qquad \text{and} \qquad I_{\mathrm{MCD}}^{M_2} = \frac{2}{9}R^2. \tag{2.32}$$

Surprisingly, the magnitude for both edges is the same. This is the result for the one-electron picture, where only one empty state is considered. Hence only one spin direction can contribute. If the non-magnetised case is considered, the result exhibits the 2:1 branching ratio that corresponds to the sublevels. Also, the very first work on MCD by Erskine and Stern arrived at 1:1 as they used the one electron picture [54]. However, as it is known even from the very first experiments at the K-edge of iron or the M-edge of gadolinium and terbium [55, 56], the magnitude of the dichroism signal for the two absorption edges differs, and is close to the 2:1 ratio. This is due to spin-orbit coupling in the final state. The stronger the spin-orbit coupling is, the more selective the excitation becomes. This selectivity then reflects in the branching ratio, which tends to be in the order of 2:1.

Two-Step Model for Magnetic Circular Dichroism

In the two-step model, the excitation process is split into two subsequent events. The first step is the excitation of an electron, independent of its spin orientation. However, in the second step, the transition can only be completed if there is an empty state with the right spin orientation.
As the initial excitation process is spin-independent, light of both helicities can excite electrons with spin-up or spin-down. The transition probabilities, Eq. (2.30) and (2.31), allow the quantitative prediction of the excitation probability. Eq. (2.26) shows that the dichroic signal is identical whether the magnetisation direction of the sample is changed or the helicity is changed. Hence, the absorption spectra look the same, e.g. for magnetisation in up-direction with right circularly polarised light or magnetisation down with left circularly polarised light. This circumstance tells that the transition probabilities calculated above contain complementary information.
In the above calculations, it was considered that the helicity is changed, but the valence state vacancy always has the same spin orientation. Now it is considered that both spin orientations have a vacancy and the helicity is kept the same. Using Eq. (2.26) and Eq. (2.30), the probabilities to excite an electron with spin-up or spin-down with light of the same helicity (here right circularly polarised) are:

$$A_{3p_{3/2}}^{down} = \frac{1}{3}R^2; \qquad A_{3p_{3/2}}^{up} = \frac{5}{9}R^2. \tag{2.33}$$

In other words, 62.5% of the electrons excited by right circularly polarised light have spin-up and 37.5% have spin-down, as illustrated in Fig. 2.5. The same can be done for the initial state $3p_{1/2}$. There the shares are 25% spin-up and 75% spin-down. For left circularly polarised light the situation is inverse. As there is no spin selection in the final states, the excitation from each level is the same for each helicity. Therefore, the lack of final state selectivity removes the dichroic signal.
However, in a ferromagnet, the final states are spin-sensitive due to the Stoner band-splitting. This spin-selectivity of the final state is the second step to the two-step model. Fig. 2.5 illustrates how the restrictions of the final state remove one excitation path per level and therefore lead to the dichroic signal. Interestingly, the number of excited electrons in the model is the same for each helicity.
The sensitivity of the detection of the final state depends on the degree of magnetisation. If there are exclusively empty spin-up states, only spin-up electrons can be excited and the dichroism signal gets maximised. For partial magnetisation, the dichroism signal is weaker. For aligned photon-spin direction and magnetisation, the magnitude of the dichroic signal is given by the difference in holes for spin-up and spin-down, and proportional to the magnetic moment m [57].

$$I_{\mathrm{MCD}} = N_h^+ - N_h^- \propto m \tag{2.34}$$

Therefore the amplitude of the MCD signal is a direct measure for the magnetic moment of the medium [55].

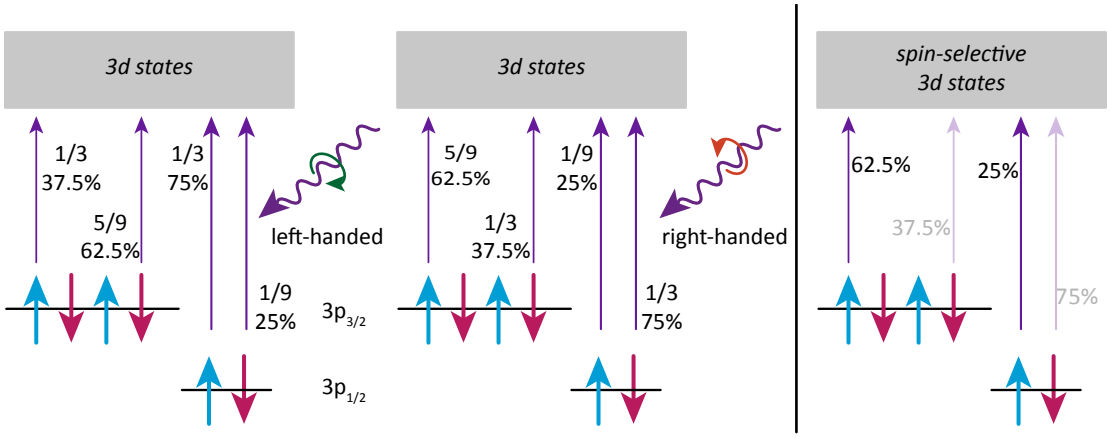

Figure 2.5: The Left and middle panel show the transition probability of the optical transition with a specific spin state driven by a left or right circularly polarised electromagnetic wave. The percentage describes the proportion that this path contributes to the total transition from this level; e.g. $\frac{1}{3}$ of $\frac{8}{9}$ $\left(=\frac{1}{3}+\frac{5}{9}\right)$ corresponds to 37.5%. Changing the helicity does not influence the total amount of excited electrons. Spin-selective final states, which only allow one spin direction for the transition, lead to a suppression of the other direction (opaque lines and numbers). Changing the helicity yields the dichroic signal in the absorption difference.

2.4 Sum Rules for Spin and Orbital Momentum

In 1992 Thole *et al.* proposed a way to determine the orbital part m_l of the total magnetic moment m_0 of a material from an x-ray MCD measurement [58]. Only one year later, Carra *et al.* developed this method further, also allowing the determination of the spin part m_S of the magnetic moment [59]. The magnetic moment is of fundamental interest as it determines the properties of magnetic materials. In their initial form, the sum rules were derived in a localised picture with only a single ion and tested at the $L_{2,3}$-edges of the $3d$-transition metals. This approach will be presented here, followed by a discussion of the applicability of the sum rules to the $M_{2,3}$-edges of the $3d$-transition metals.
Using the picture derived in Fig. 2.4, a typical MCD spectrum for an L-edge of a $3d$ transition metal qualitatively looks as shown in the lower-left panel of Fig. 2.6 (green line). Thole and Carra came up with a systematic approach to use this characteristic trace to retrieve the spin and orbital momentum, using the absorption for right circularly (μ_+), left circularly (μ_-) and linear polarised light (μ_0). μ_0 is also called white-line and can be determined by the mean of μ_+ and μ_-, $\mu_0 = \frac{1}{2}(\mu_+ + \mu_-)$. The sum rule for the expectation value of the orbital angular momentum $\langle L_z \rangle$ is given by

$$\frac{\int_{j_+ + j_-} dE(\mu_+ - \mu_-)}{\int_{j_+ + j_-} dE(\mu_+ - \mu_- + \mu_0)} = \frac{1}{2}\frac{l(l+1)+2-c(c+1)}{l(l+1)(4l+2-n)}\langle L_z \rangle \tag{2.35}$$

and for the expectation value of the spin momentum $\langle S_z \rangle$ with the expectation value of the magnetic dipole operator $\langle T_z \rangle$:

$$\frac{\int_{j_+} dE(\mu_+ - \mu_-) - \frac{c+1}{c} \int_{j_-} dE(\mu_+ - \mu_-)}{\int_{j_+ + j_-} dE(\mu_+ - \mu_- + \mu_0)}$$

$$= \frac{l(l+1) - 2 - c(c+1)}{3c(4l + 2 - n)} \langle S_z \rangle \tag{2.36}$$

$$+ \frac{l(l+1)[l(l+1) + 2c(c+1) + 4] - 3(c-1)^2(c+2)^2}{6lc(l+1)(4l + 2 - n)} \langle T_z \rangle \, .$$

Here, c and l are the initial and final state's orbital quantum number and n is the number of valence electrons. j_+ corresponds to the spin-orbit split level at lower binding energy, whereas j_- sorreponds to the one at higher binding energy.
Another version of the sum rules was proposed by Wu *et al.* [60, 61]. They suggest considering only the ratio of the orbital momentum L_z and the sum of the spin S_z and T_z.

$$\frac{\langle L_Z \rangle}{2 \langle S_z \rangle + 7 \langle T_z \rangle} = \frac{2}{3} \frac{\int_{j_+ + j_-} dE(\mu_+ + \mu_-)}{\int_{j_+} dE(\mu_+ - \mu_-) - 2 \int_{j_-} dE(\mu_+ - \mu_-)} \tag{2.37}$$

However, this does not eliminate the treatment of T_z. Stöhr and König came up with an approach to measure the magnetic dipole moment T_z: the magnetic dipole moment becomes of significant magnitude in materials with large anisotropies. Therefore their approach is an orientation-averaged sum rule, calculated from a series of measurements at different orientations [62]. However, the contribution of the magnetic dipole operator for an isotropic medium e.g. iron, cobalt and nickel is usually on the order of 10% [59, 63, 64]. It can be neglected, as will be done in the scope of this work.
In the past, the sum rules have been tested against theoretically obtained values for the orbital and spin momentum. It turned out that the agreement was within 10% for the orbital momentum. In contrast deviations of up to 50% from the calculated values appeared for the spin momentum sum rule [60, 61].
In theory, the application of the sum rules is straightforward. The contribution from the absorption at, e.g. the L-edge from the $2p_{1/2}$ and from the $2p_{3/2}$, can be separated and independently integrated. Experimentally the situation is not always that clear: the chosen integration range can change the results significantly. It will be shown later that uncertainties of the integration range have a much stronger impact on the expectation value of the spin moment than on the angular orbital momentum. Furthermore, the removal of the background and experimental noise can contribute to a discrepancy between the experimental data and the theoretically predicted values.
Nevertheless, the sum rules are established tools, e.g. for the use at the L-edges of $3d$-transition metals (Fe, Co, Ni) [65]. Moreover, they are applied to time-resolved

measurements to observe the evolution of $\langle L_z \rangle$ and $\langle S_z \rangle$ during and after laser excitation [14, 66].
The sum rules were derived under many assumptions [67]. These assumptions must be considered when applying them.

2.4.1 Applicability of Sum Rules to M-edges

Although the first prediction of magnetic dichroism in 1975 by Erskine and Stern was made for the nickel M-edges [54], MCD at that very absorption edge is rarely studied [68]. Moreover, the sum rules have not been applied to M-edges of the $3d$-transition metals yet, as they were derived for systems with large spin-orbit coupling such as $L_{2,3}$-edges of the $3d$-transition metals and the $M_{4,5}$-edges of the $4f$ rare-earth elements. This raises the question, if the sum rules can also be applied to the M-edges of the $3d$-transition metals. Looking at the assumptions that were made for their derivation and transferring them, an estimation about their validity will be given.
The sum rules cannot be applied when two transition channels compete, in the case of M-edges, those are $3p \rightarrow 3d$ and $3p \rightarrow 4s$. However, the oscillator strength of the $3p \rightarrow 3d$ transition is much larger, as the electronic levels have the same principal quantum number [69], which means that $3p \rightarrow 4s$ transition can be neglected.
Another crucial point for the validity of the sum rules is the normalisation of the integrals. Only when this normalisation is done correctly, the numeric value that results from the sum rules is meaningful. The assumption is that the normalisation factor N cancels the radial matrix element. However, this is not always true, as the radial matrix element is spin- and energy-dependent [70] and can change up to 30% within the d-band of nickel [61, 71]. But this is only a problem for the validation of the spin sum rule. The orbital momentum is proportional to the spin-orbit coupling energy, which is not affected by the radial matrix element [72].
One more assumption that is made for the sum rules is that spin-orbit coupling is the dominant interaction. At M-edges, this is not the case. The exchange interaction between $3p$ and $3d$ is much larger than the $2p$ and $3d$, and as the spin-orbit coupling is much smaller, this assumption does not hold. However, this also does only act out on the spin sum rule [73, 74].
The above indicates that the orbital sum rule can be used for also for the $M_{2,3}$ of the $3d$-transition metals. The case of the spin sum rules is more difficult, the assumptions, already lead to severe deviations from the actual result at the L-edges [58, 75–77]. This becomes even more severe when going to the M-edges.

The following section will show how the sum rules are applied to spectra, where the spin-orbit coupling is smaller than the linewidth of the core levels, despite of the problems that arise from the assumptions that do not necessarily hold for small spin-orbit coupling. Later-on, this approach will be applied to time-resolved measurements.

2.4.2 Evaluating Absorption Spectra Using the Sum Rules

The two cases of L- and M-edges are schematically illustrated in the upper panels of Fig. 2.6, focusing on their different spin-orbit splitting.
In this idealised scenario, the following assumptions are made: (i) no background contribution; (ii) absorption only resonant from the core states with a finite width; and (iii) no competing absorption channels. In this case, the integration range is unambiguously defined. The slightly bulky equations (2.35) and (2.36) can be condensed using the following notation:

$$\Delta Q_i = \int_{j_i} \Delta_{\mathrm{MCD}} dE; \qquad Q_i = \int_{j_i} \mu_0 dE \tag{2.38}$$

where j_i denotes the spin split core-levels, $\Delta_{\mathrm{MCD}} = \mu_+ - \mu_-$ is the MCD signal and $\mu_0 = \frac{1}{2}(\mu_+ - \mu_-)$ is the white-line absorption, of a non-magnetised sample. Within this notation, the sum rules for the orbital momentum becomes:

$$\langle L_z \rangle = \frac{2}{3} \frac{H_h}{P_c cos\theta} \frac{\Delta Q_3 + \Delta Q_2}{Q_3 + Q_2} \tag{2.39}$$

and for the spin momentum:

$$\langle S_z \rangle = \frac{1}{2} \frac{H_h}{P_c cos\theta} \frac{\Delta Q_3 - 2\Delta Q_2}{Q_3 + Q_2} - \frac{7}{2} \langle T_z \rangle , \tag{2.40}$$

where H_h denotes the number of holes, P_c the ellipticity of the circularly polarised light. θ is the angle between the magnetisation of the sample $\vec{m}$ and the k-vector of the incident light $\vec{k}$.

The equations are illustrated in Fig. 2.6. In the upper panels, the absorption μ at the two spin-orbit split levels $p_{1/2}$ and $p_{3/2}$ is shown, for light of opposite helicities $\pm$ together with the white-line absorption. Additionally, the integral over the white-line absorption is plotted and labelled $Q_3 + Q_2$. In the lower-left panel, the two integral build-ups for S_z and L_z are shown, the integral over the sum of the two levels $\Delta Q_3 + \Delta Q_2$ (solid red line) and integral over the difference of the two $\Delta Q_3 - 2\Delta Q_2$, including the factor of 2 for Q_2 (dashed red line). These formulas can be understood in terms of the $l - s$ and $l + s$ notation: The sum of both removes the s-component, and isolates the l-component. The difference achieves the opposite. The factor of two corrects for the ratio of the electron content in the respective level. So adding the two will remove the s-component while subtracting will only leave the s-part.
The right panels in Fig. 2.6 contain the situation as it occurs at the M-edges. In this simplified description, the absorption peaks are only split by 0.8 eV so that they energetically overlap. When integrating the sum of the two absorption peaks, as is done for L_z, the final value of the integral does not change. However, the integral for S_z heavily depends on the selection of the integration ranges, as is indicated by the purple lines.
The main message here is that the value of L_z does not depend on the size of the spin-orbit splitting, as long as the prerequisites for the application of the sum rules, as

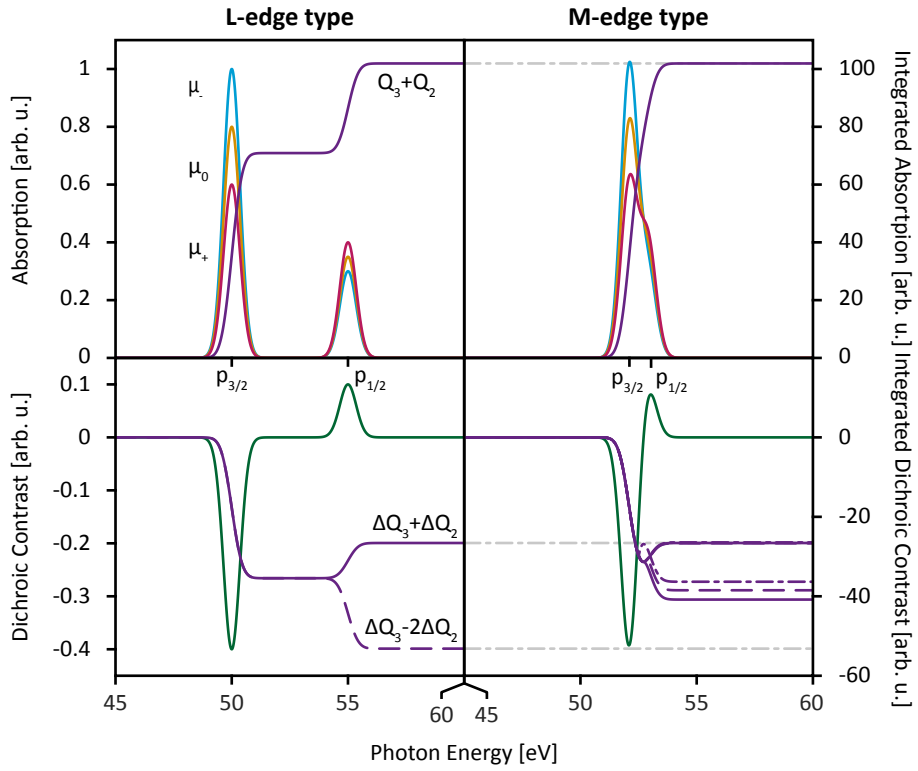

Figure 2.6: The upper panels show the absorption spectra for an exemplary system with large and small spin-orbit splitting, corresponding to absorption at the L- and M-edge. The integral over the white-line absorption is plotted in purple. Its final value does not depend on the exchange splitting. In the lower panel, the MCD difference signal is plotted (green). The purple lines represent the numerator of S_z (dashed line) and L_z (solid line), respectively.

discussed in 2.4.1, are met.
Looking at experimental data from L-edges, e.g. [14, 78] shows that in the presence of background and satellite peaks, the evaluation is not completely straightforward. Discrepancies could be caused, for example, by slightly varying integration ranges or different background subtraction. At the M-edges, an additional challenge arises from the energetic overlap of the spin-orbit split core-levels, which is problematic for the determination of S_z. However for L_z these restrictions do not apply, even the overlap of the absorption lines, do not influence the value of the integral.
To summarize, the application of the sum rule for L_z seems to not bear many problems; one has to be careful when applying it for S_z, especially for statements about the magnitude. Nevertheless, for time-resolved studies the evolution of the signal and its quantitative value are two different observables. Even if the value is not accurate, its time evolution still holds information.

Additionally modern theoretical tools and TD-DFT calculations can support the efforts. Calculated spectra allow to partially disentangle contributions from the $3p_{1/2}$ and $3p_{3/2}$ level. Given that calculations can provide that information, this can be applied to experimental data as well.
In the following, one has to aware of the restrictions due to the assumptions made in the derivation of the sum rules. However, it seems worthy to use the achievements of the last 25 years and advance the use of sum rules.

Chapter 3

Attosecond Magnetisation Dynamics

The change of the magnetic state of matter by light has been demonstrated by several experiments in the past two decades [11, 12]. All of these experiments show that laser pulses trigger a sequence of effects that lead to demagnetisation. Such effects are e.g. spin-orbit coupling, electron-phonon coupling or spin-lattice relaxation.
However, all these studies did not provide insight into the very early stage of demagnetisation. In particular, sub-femtosecond resolution yielding information on whether the electric field of light can directly manipulate the magnetic moment of matter is missing. In the course of this thesis, an experimental scheme was developed which is capable of tracking changes in magnetisation with sub-femtosecond resolution. For this, the polarisation of an attosecond pulse is turned circular to probe magnetic circular dichroism (MCD) in a transient absorption type experiment. A phase-stabilised few-cycle near-infrared laser pulse excites the sample, and triggers electronic and magnetic dynamics. The following chapter will describe the experimental procedure, as well as, the underlying physics that made it possible to detect the theoretically proposed light-induced spin-transfer across an interface [79, 80].

3.1 Basic Idea

A circularly polarised XUV attosecond pulse is transmitted through a magnetised sample consisting of a ferromagnetic and a paramagnetic domain. The transmitted attosecond pulse is then sent into a spectrometer, see Fig. 3.1. By applying the Beer-Lambert law

$$\mu(\omega) = \ln \frac{I(\omega)}{I_0(\omega)} \tag{3.1}$$

the sample specific absorbance $\mu(\omega)$ can be calculated.

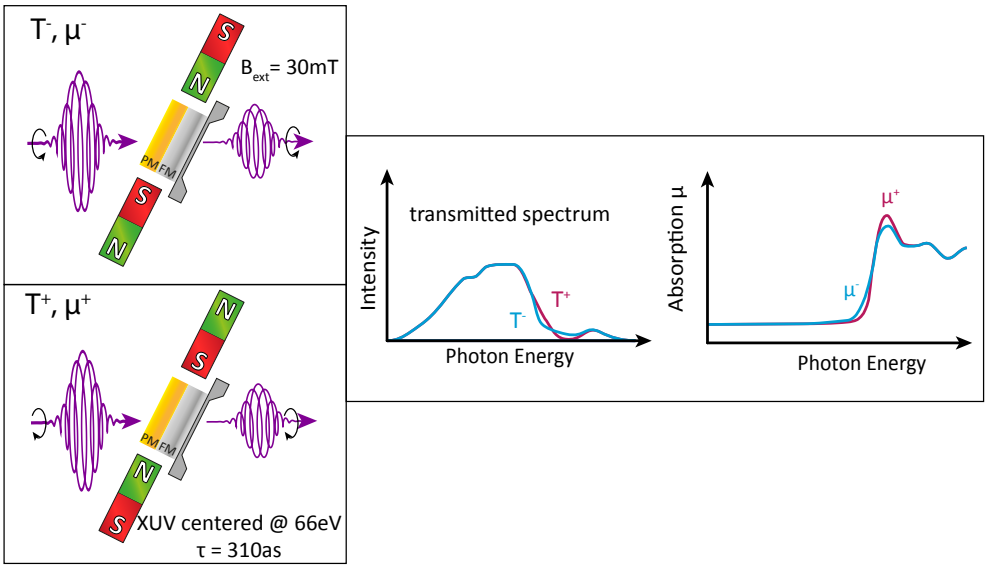

Figure 3.1: A circularly polarised XUV light pulse is transmitted through a magnetised sample. The sample consists of ferromagnetic and paramagnetic layers. The transmitted spectrum is recorded, and the absorbance $\mu^{\pm}$ is calculated. Due to magnetic circular dichroism the transmitted spectra for opposite magnetisation are different. This difference is the dichroic signal. The effect can be studied looking at the transmission only or calculating the absorption.

In conventional MCD spectroscopy the signal is the subtracted absorbance of left- and right-circular polarisation.

$$\Delta_{\mathrm{MCD}}^{conv}(\omega) = \mu^{+}(\omega) - \mu^{-}(\omega) \tag{3.2}$$

In the experiment and study conducted here, a different convention is used. In the case of atto-MCD the contrast Δ_{M} is given by:

$$\Delta_{\mathrm{M}}^{atto}(\omega) = T^{+}(\omega) - T^{-}(\omega) = \Delta_{M} \tag{3.3}$$

where $T^{+}(\omega)$ is the frequency dependent transmitted spectral intensity for right circular polarised light and respectively $T^{-}(\omega)$ for left-circular polarised light.

In Fig. 3.2, both definitions are plotted, to justify the use of atto-MCD. It is safe to say that the two compare quite well, the main peak feature is slightly shifted in energy and the pre-edge is not as pronounced in the conventional definition. Nevertheless, both signals provide direct access to the magnetic dichroism and therefore, to the magnetisation of the sample.
Later-on where the time-evolution of the magnetisation will be investigated, the two definitions will be compared again. The agreement is not surprising, as $I_0(\omega)$ in the case of conventional MCD is a constant factor and only the natural logarithm changes the

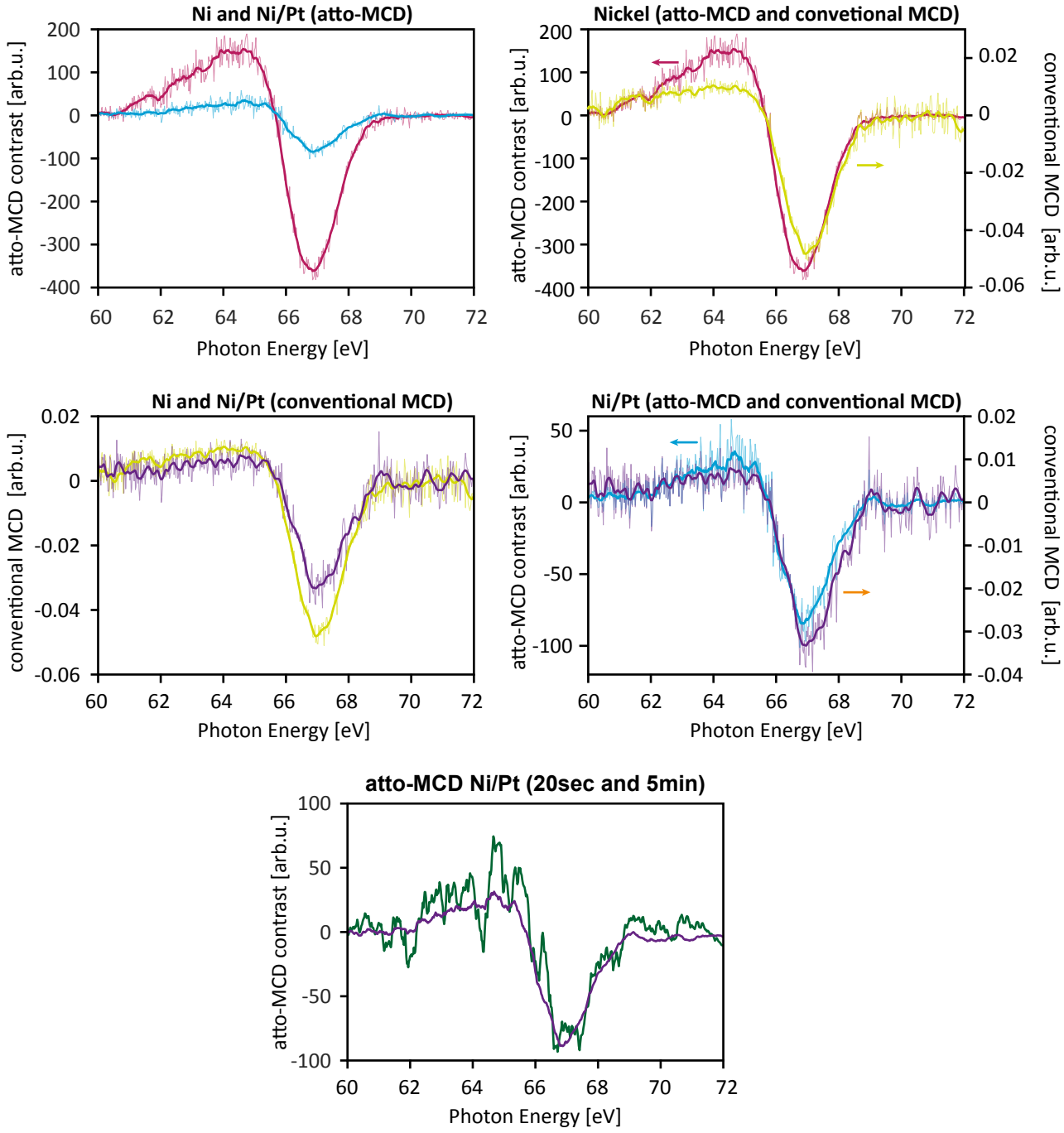

Figure 3.2: The panels in this figure compare the different ways of evaluation of the data as well as the signals from the different samples. Each colour represents one sample and evaluation method. Ni atto-MCD (red), Ni/Pt atto-MCD (blue), Ni conventional MCD (yellow), Ni/Pt conventional MCD (purple). The atto-MCD signal for Ni and Ni/Pt differs in magnitude, as the absorption in platinum lowers the overall transmission and leads to a decreased dichroic signal. Atto-MCD and the conventional MCD evaluation are for Ni and Ni/Pt very similar, justifying the use of the atto-MCD evaluation. The panel at the bottom shows the comparison of short (20 s) and long (5 min) integration times. The dichroic signal is clearly visible after 20 s, longer integration time suppresses the noise.

shape slightly. From now on throughout the thesis, the atto-MCD contrast, according to Eq. (3.3), will be used.

A strong electric field that coincides with the attosecond pulse triggers electronic processes in the sample. These processes include carrier excitation from valence states to above the Fermi energy or spin migration and flips that lead to a change in magnetisation. This is where attosecond transient absorption spectroscopy can show its strengths. All these processes manifest themselves in changes in the XUV absorption of the sample. The electrons' actions can be mapped with sub-femtosecond resolution, owing to the temporal confinement of only a few hundreds of attoseconds.
As the amplitude of the atto-MCD contrast provides information on how strongly magnetised the sample is, tracking its temporal evolution gives insights into how fast the change of magnetisation happens and therefore allows to reconstruct the underlying processes.

3.2 Experimental Setup

The experiment was carried out at the AS2 beamline. A few-cycle near-infrared phase-stabilised laser pulse ($\tau_{\mathrm{NIR}} < 4\,\mathrm{fs}$) generates high-harmonic radiation (for details about the beamline and the lasersystem, see Appendix A.1). The fundamental and the high-harmonics are then spatially separated into a Mach-Zehnder-type interferometer. A thin metal foil (150 nm aluminium) blocks the residual laser light while the XUV radiation is transmitted. After this, the attosecond pulse is sent through an XUV phase retarder that changes its polarisation to elliptical. Further spectral filtering is achieved by a multilayer mirror designed to reflect at 66 eV with a bandwidth of 8 eV. In the other arm of the interferometer, the NIR pulse is delayed by a piezo stage.
Subsequently, the two beams are recombined and focused by a toroidal mirror under grazing incidence onto the sample. The sample is magnetised by two static neodymium magnets which are mounted on a motorised wheel, enabling to switch the direction of the magnetic field within fractions of a second. Behind the target, a metal plate with a 200 μm slit serves as a beam block for the NIR to reduce stray-light on the camera and also serves as an entrance slit for the spectrometer. The spectrometer consists of a platinum-coated toroidal grating (Jobin Yvon HORIBA, 2105 lines/mm) and an XUV sensitive CCD camera (Princeton Instrument, PIXIS XO400B).
The focused dimension of the spectrum covers approximately 8-10 pixels (160-200 μm) of the chip of the camera. Integrating over these columns of the chip yields the spectral intensity as a function of energy.

3.2.1 Quarter-Wave Phase Retarder for XUV Attosecond Pulses

To measure magnetisation dynamics on atto- or sub-femtosecond timescales, circularly polarised attosecond pulses are required. To turn the polarisation of an attosecond pulse circular, an idea that was originally proposed for sychrotron radiation is used [42].

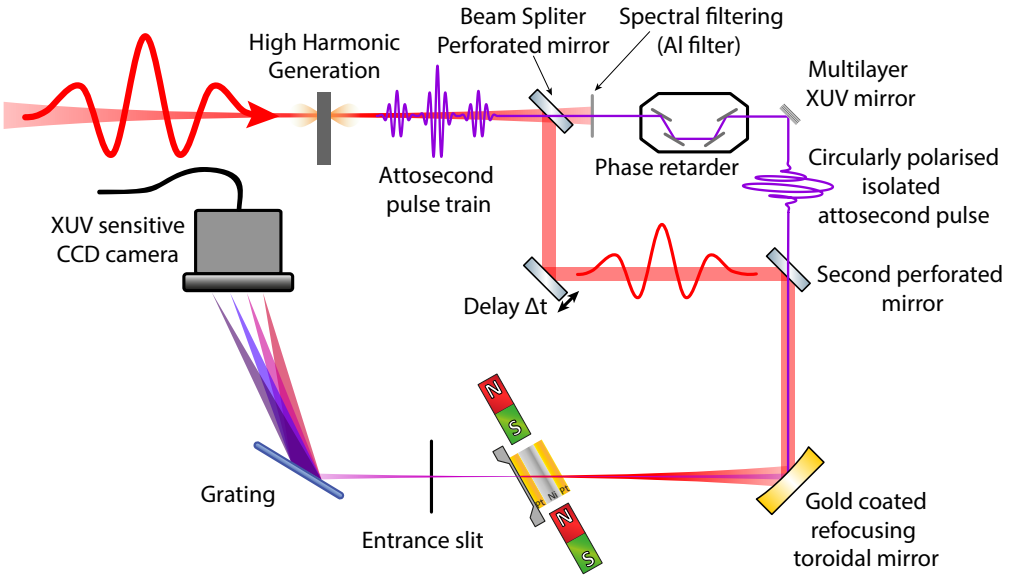

Figure 3.3: The attosecond transient absorption setup in the AS2 beamline. A few-cycle laser pulse generates high-harmonic radiation. Spectral filtering is done by an aluminium filter and a multilayer mirror, providing isolated attosecond pulses. The phase retarder makes the pulse circularly polarised. A delay is introduced in the NIR arm of the Mach-Zehnder-type interferometer. After the recombination, the beams get focused on the magnetised sample. The transmitted spectrum is recorded by a self-built spectrometer. Initial publication in [81].

The idea is to orient four mirrors in such a way that the reflections lead to a total phase shift between s- and p-polarisation of a quarter of a wave, resulting in circular polarisation. However being designed for the use at synchrotrons with comparably long bursts of XUV radiation, the requirement for the mirrors are higher when dealing with attosecond pulses. For the use in an attosecond experiment, special care has to be taken regarding the temporal phase these mirrors introduce.
This idea was already taken up in 2011 for the use with XUV from a high-harmonic source [82], however this source did not provide isolated attosecond pulses but attosecond pulse trains and the phase retarder had a transmission of a few percent only. Therefore, further development of the idea was necessary.
The design of reflective optics for attosecond pulse follows two main considerations, (i) no significant increase of the pulse duration, (ii) high reflectivity for high photon flux. For the design of the device, which changes the polarisation, another consideration was important: the phase for s- and p-polarisation and that the beam must not propagate in a different direction when changing the polarisation state by rotating the apparatus.

The polarisation state after reflection off a mirror can be expressed by the Fresnel equations. They provide a term for the reflected s- and p-polarised part and therefore the phase difference can be calculated from [83]:

$$\tilde{r}_s = r_s e^{i\delta_s} = \frac{\cos\theta_i - \sqrt{\varepsilon_r - \sin^2\theta_i}}{\cos\theta_i + \sqrt{\varepsilon_r - \sin^2\theta_i}} \tag{3.4}$$

$$\tilde{r}_p = r_p e^{i\delta_p} = \frac{\varepsilon_r\cos\theta_i - \sqrt{\varepsilon_r - \sin^2\theta_i}}{\varepsilon_r\cos\theta_i + \sqrt{\varepsilon_r - \sin^2\theta_i}} \tag{3.5}$$

It becomes clear that upon reflection the phase shift between s- and p-polarised light is not the same. This leads to a difference of

$$\Delta_\varphi = \delta_s - \delta_p \tag{3.6}$$

which then can be exploited to tailor the phase shift as desired. From Eq. (3.4) and (3.5), it is clear that Δ_φ can be manipulated by the incidence angle θ_i on the mirrors and ϵ_R which is given by the material of the mirror.

However, two angles can be varied, see Fig. 3.4. The incidence angle θ_i that is the angle between the surface normal of the mirror and the incoming beam and the rotation angle θ_{pa} of the mirror setup. The latter one does not influence r_s and r_p and therefore, the phase shift. However, it does determine the amplitude ratio of s and p. As not only the phase shift determines the ellipticity but also the intensity of the two polarisation states. In order to be perfectly circularly polarised s- and p-polarisation need to have the same amplitude.
The polarisation state of the light emerging from the phase retarder is analysed with a Rabinovitch setup [84]. An XUV multilayer mirror is placed in the beam reflecting under 45°. The intensity of the reflected beam is recorded by a reverse-biased XUV sensitive photodiode (AXUV100G, OptoDiode Corp.). The 45° mirror, together with the photodiode, can be rotated around the beam axis. The resulting intensity vs rotation angle data gives the polarisation state and is shown in Fig. 3.5. In the top panel, the theoretical predictions are shown. For the case of $\theta_{pa} = 90°$ the signal becomes a sine-like curve.

For completely polarised light the ellipticity can be determined from the measured intensities. It is given by [84]:

$$\epsilon = \sqrt{\frac{I_{min}}{I_{max}}}, \tag{3.7}$$

where I_{max} is the maximum intensity and I_{min} the minimal intensity for a specific rotation of the phase retarder. From the above formula follows that for an ellipticity $\epsilon = 0$ the light is either completely s- or p-polarised and 1 for perfectly circular polarised. Perfect circular polarised would yield a flat line of the intensity as a function analyser rotation, as shown in Fig. 3.5.
For the case of this setup a maximum ellipticity of $\epsilon \approx 0.5$ was achieved for a rotation

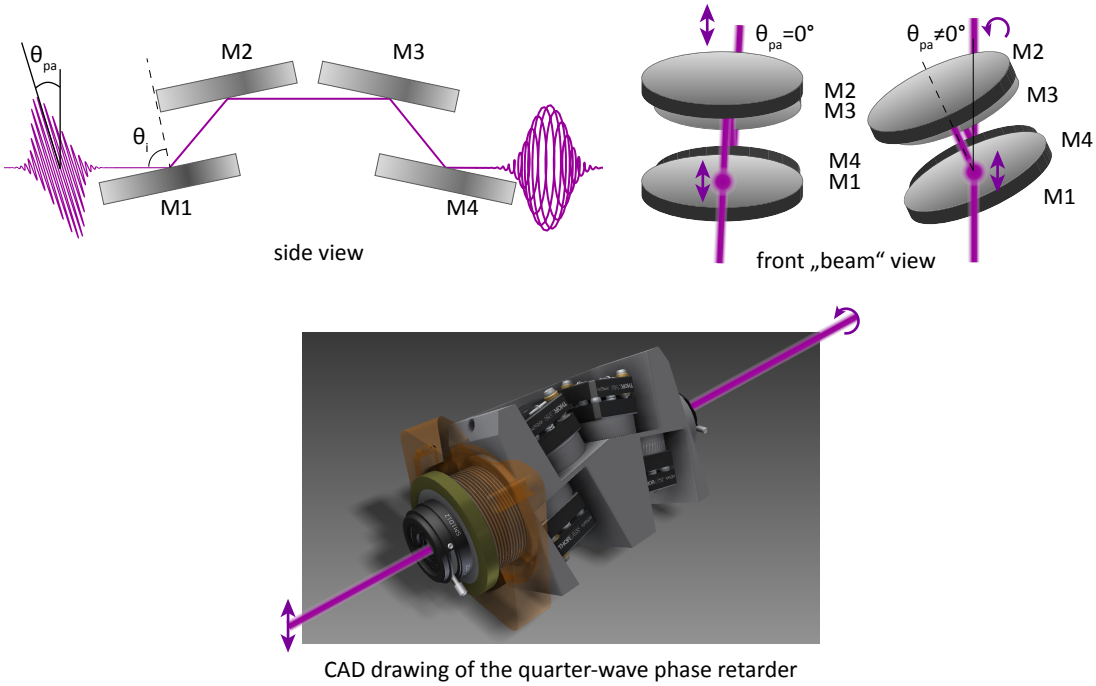

Figure 3.4: The quarter-wave phase retarder that is used to turn the polarisation of the attosecond pulse circular. It has two angles that can be tuned to achieve that. The incident angle θ_i and the angle under which it is hit θ_{pa}. The panels illustrate how this is done. The incident angle is fixed by the construction of the device. The polariser angle, which is the angle between the linear polarisation direction of the incident electromagnetic wave and the projected surface normal of the mirrors, can be changed by rotation of the quarter-wave phase retarder. M1-M4 indicate the order in which the mirrors are illuminated. The lower panel shows a CAD drawing of the phase retarder, the mirror holders are mounted in an aluminium block, fabricated by the MPQ workshop.

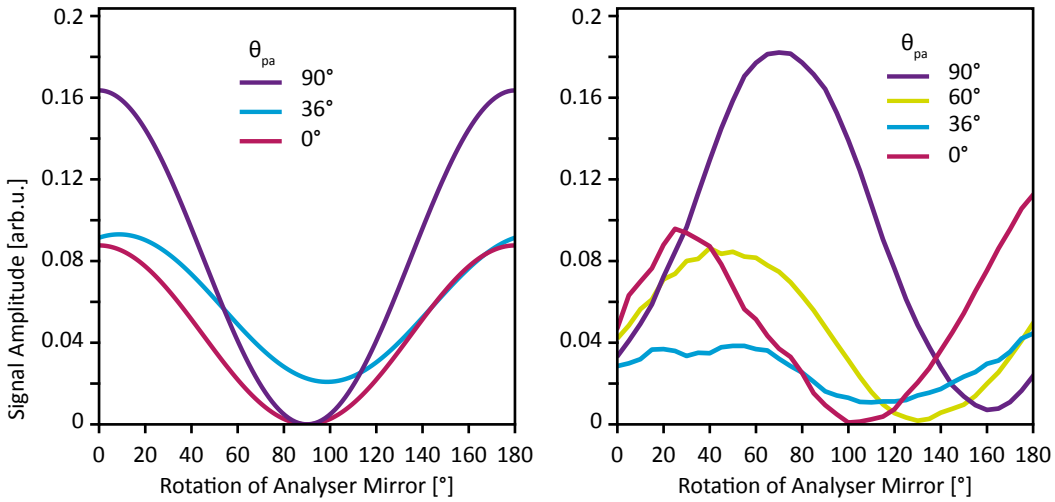

Figure 3.5: The left panel shows the calculated signal amplitude of the photodiode as a function of the rotation angle of the analyser mirror for three orientations of the phase retarder. Maximal ellipticity is achieved for $\theta_{pa} = 36°$. Fully circular polarisation would give a constant line in this diagram. The right panel shows the experimental results for four orientations of the polariser, confirming the predicted values.

angle of $\theta_{pa} = 54°$ of the phase retarder . This is in good agreement with the theoretical predicted value of $\epsilon_{theo} = 0.549$ at 66 eV, for details see [85].
After the confirmation that the XUV radiation when emerging from the polarising device is indeed elliptically polarised, it still has to be verified that the attosecond pulse does not lose its temporal structure. For this reason, attosecond streaking was performed. Details about the technique can be found in chapter 5. As expected, the attosecond pulse was not affected a lot by the four mirror reflections, due to their flat spectral phase. A FROG like retrieval algorithm was used to retrieve a duration of $\tau_{\mathrm{XUV}} = 310 \pm 20$ as. Fig. 3.6 shows the raw streaking spectrogram and the retrieved electric field.

3.2.2 Data Acquisition and Evaluation

The data is recorded with an XUV sensitive CCD camera (Princeton Instruments PIXIS XO 400B). This camera is controlled by a custom LabView Software. Typical integration times for the measurement were 15-20 seconds.
The software is capable of controlling the rotation of the magnets as well as a beam block in the NIR beam path. This allows the measurement of the following sequence for one delay step: magnetisation 1 with NIR pump light - magnetisation 1 without NIR pump light - magnetisation 2 with NIR pump light and magnetisation 2 without NIR pump light. This sequence was then repeated for every delay step, leading to a duration of maximum 1.5 minutes for one delay step. As drifts of the beamline and CEP locking make measurement durations of more than 3 hours unreliable, this set an upper limit to

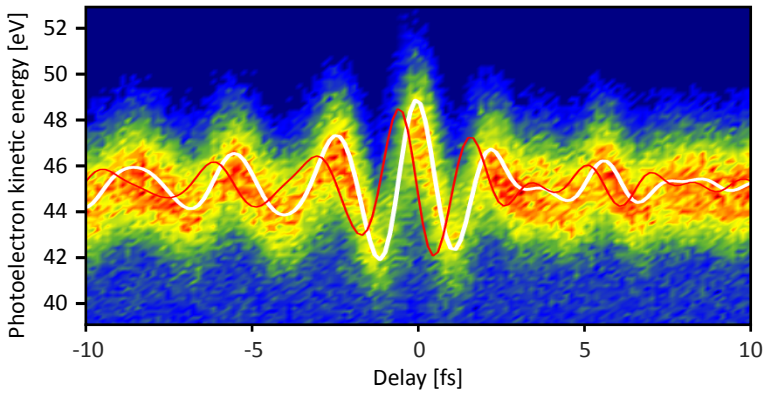

Figure 3.6: Attosecond streaking with a circularly polarised attosecond pulse. The retrieved pulse duration is $\tau_{\mathrm{XUV}} = 310\,\mathrm{as}$. The retrieved vector potential (white) and the electric field (red) are plotted.

the total investigated delay range. Data evaluation was performed using a self-written MATLAB GUI, which allowed for quick comparison of the measurements, with many adjustable parameters.

3.3 Electronic Response of a Metallic System

The XUV absorption gives access to the electronic structure of a medium around the Fermi energy. In the case of interaction between a strong laser electric field and a specimen it is possible to make deductions about the response of the electrons to the strong external field. This was previously shown for semiconductors and dielectrics [36–38]. The first metallic system was studied only recently [86]. The experiment presented here, intrinsically designed to track magnetisation dynamics, is also capable of measuring light-induced electron dynamics manifesting themselves as changes in the XUV absorption.
As described in section 3.2.2, each measurement consists of the acquisition of four spectra per delay step. For both magnetisation directions, one spectrum is taken in the presence of the intense laser field and one in its absence. Each set for one of the magnetisation directions itself contains the information on how the electric field of the laser changes the electronic structure and therefore the XUV absorption.
In general, there are two options to evaluate the measured data. The first one is to use the spectrum of the incident beam and calculate the frequency-resolved absorption and see how it changes with the delay. This is in analogy to the conventional MCD definition presented in section 3.1. The second option, the option used here, is to simply use the frequency-resolved transmitted spectrum and compare the spectra with and without strong-field interaction. The change in XUV transmission is given by:

$$\Delta T(\omega) = \frac{T_{\mathrm{pump}}(\omega)}{T_0(\omega)} \tag{3.8}$$

where T_{pump} describes the transmitted spectral intensity. The evaluation of the transmitted spectra only, has the big advantage that drifts in the XUV spectrum do not manifest themselves in the results, as all spectra suffer from it. These small slow drifts do occur and originate from, e.g. beamline drifts or small fluctuations of the pressure in the high harmonic target.

Fig. 3.7 illustrates the transmitted spectra through an 8 nm thick nickel film for the unperturbed case (red) before the NIR laser pulse triggers electronic excitation and slightly after the passage of the strong field interaction (blue). At a laser pulse intensity of $I = 5 \times 10^{12}\,\mathrm{W/cm^2}$, the increased absorption appears as a shift of the absorption edge of up to 150 meV, or a decrease in transmission of up to 5% at the $M_{2,3}$ absorption edge.
A possible reason for this change of the XUV absorption is that electrons around the Fermi edge get promoted to above the Fermi energy, where they occupy previously unoccupied states. The emptied states now become available for core-transitions from the $M_{2,3}$ edges, leading to an increased absorption at energies below the ones corresponding to the resonant excitation from $3p_{1/2}$ and $3p_{3/2}$.
Although previously seen [12], in this study, no pronounced increase in the transmission is observed. The rise of transmission at higher photon energies is supposedly present, however, very small and spread over a larger bandwidth. This can be seen as direct

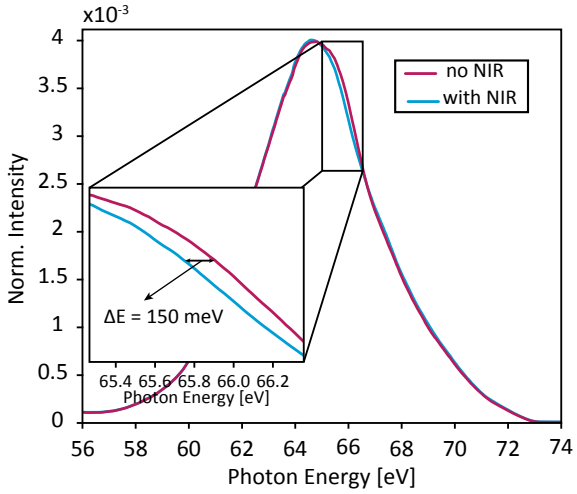

Figure 3.7: The transmitted XUV spectrum through an 8 nm thick nickel film in the absence of an external perturbation and slightly after the interaction with a few-cycle NIR laser pulse. The onset of the absorption is shifted by 150 meV towards lower photon energies indicating that the laser pulse frees states below the Fermi energy, enabling core-level transition to lower energetic states.

evidence that the electrons that get excited are subsequently accelerated in the bands and promoted into higher bands.
Recording the change of the XUV transmission over time, Fig. 3.8 shows a rapid drop during the interaction with the strong laser electric field and a quick recovery < 1 ps.

For different pump energies, the induced absorption change varies. In Fig. 3.8, the change for three different values ranging from 1×10^{12} W/cm^2 to 5×10^{12} W/cm^2 is shown and time constants of the recovery are determined. The retrieved relaxation times based on fitting an exponential recovery to the data, varies between 289 ± 79 fs for the low intense case and 319 ± 65 fs for the high intense one in pure nickel and is 376 ± 103 fs for the nickel/platinum multilayer sample. The value gives the time after which the signal has recovered half its amplitude. Within the experimental errors, the recovery for different pulse energies is on the same scale. Additionally Fig. 3.8 shows the comparison of a pure nickel sample and a nickel/platinum multilayer stack. Their responses are fairly identical only the change in magnitude differs slightly. In the next section, that covers the magnetisation dynamics, the reason for the two samples will be explained.
Using the full power of the attosecond beamline and zooming into the time interval where the laser pulse is present one gets a trace as shown in Fig. 3.9. The decrease in transmission around 66 eV does not appear homogeneously over the duration of the laser pulse, as Fig. 3.8 might suggest. It happens in a step-like fashion. The steps are in synchrony with the oscillation period of the NIR pump pulse (green line). The exact phase relation between the steps and the driving field is not yet known. Here it is arbitrarily chosen to guide the eye.

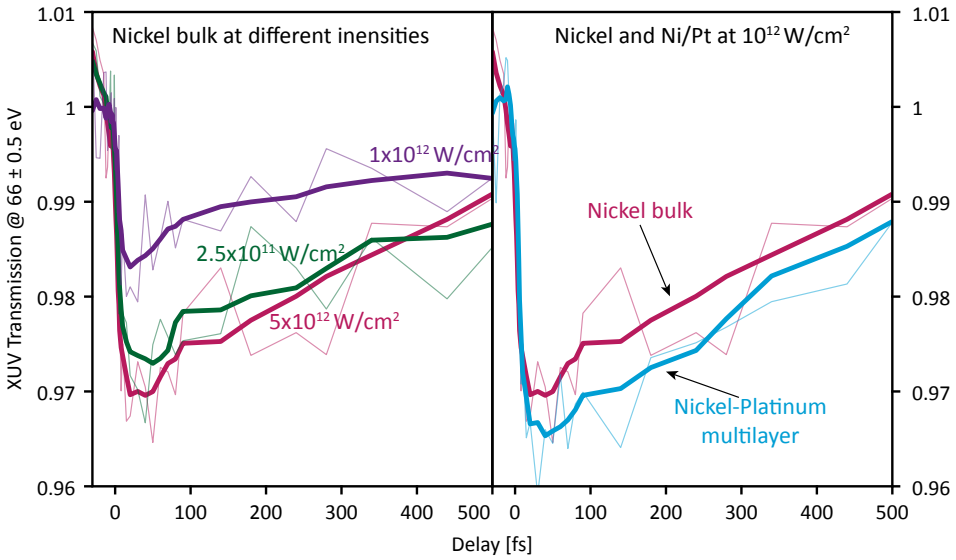

Figure 3.8: Temporal Behaviour of the change in XUV transmission. The left panel shows the XUV transmission of nickel for three different intensities. The right panel compares the response of a nickel thin-film and the Ni/Pt multilayer sample. The multilayer sample exhibits a deeper drop, the recovery looks similar in both samples. Thin lines represent the raw data for lineouts taken at 66±0.5 eV, thick lines depict an adjacent average along the time axis.

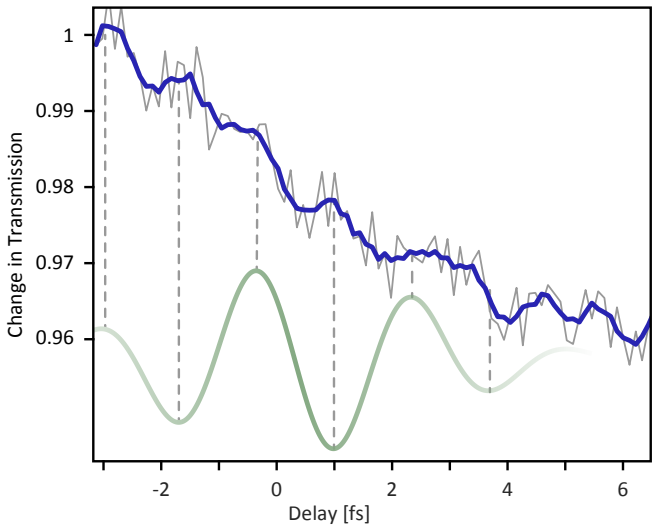

Figure 3.9: The XUV transmission at 66±0.5 eV as a function of time. The raw data (grey) shows a step-like decrease which is more pronounced when a moving average filter is applied (blue). These steps are in synchrony with the field evolution of the laser pulse (green line, as a guide to the eye). After the laser pulse has passed the XUV transmission stays changed.

The synchrony of the oscillating electric field and the changes in the material's properties is of great interest for multiple reasons. The first one is that this behaviour has been discovered in semiconductors and dielectrics before [36, 37]. Another very important point is that it allows the determination of the arrival time of the laser pulse. As these oscillations can be resolved, it is direct evidence that the response time of the system to the external perturbation must be shorter than a half-cycle duration of the laser pulse. If the electronic excitation was delayed, the effect would integrate over the oscillations of the laser pulse, and the step-like structure would vanish. Therefore the sub-cycle response of the XUV transmission provides confinement of time-zero to about 1 fs.
The presence of the sub-cycle structure equips the measurement of the magnetic moment with a marker for the arrival of the electric field, meaning that a delayed response of the magnetic moment could be tracked.

3.4 Attosecond Magnetic Circular Dichroism

The finding of the above-described effect is a fortunate result of the initial experiment to study the early time dynamics of the magnetic moment in ferromagnetic systems. It buries the prospect of underlying fundamental physics. Moreover, in tandem with the already existing results from a small and wide band gap material a unified concept for light-matter interaction might be possible. However, in the scope of this thesis, the focus lies on the study of time-resolved changes of magnetisation.

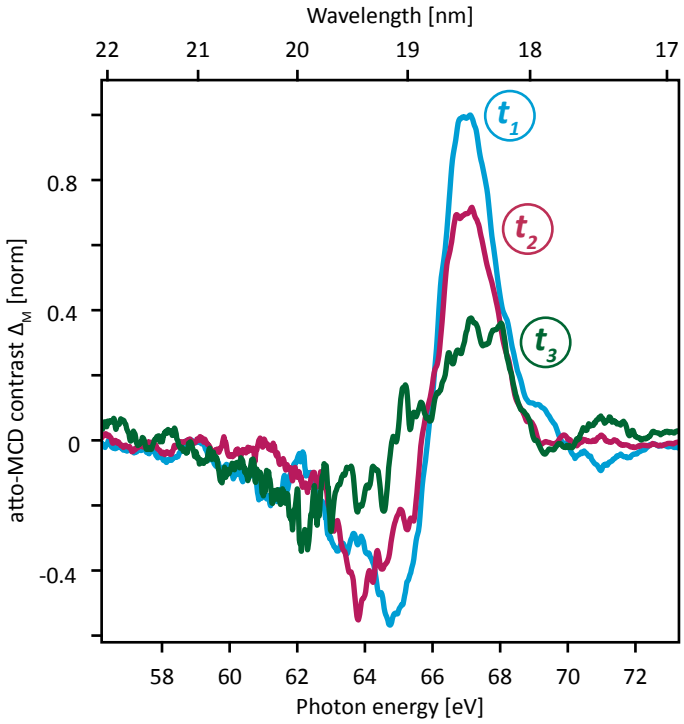

Figure 3.10: Atto-MCD contrast for the nickel/platinum multilayer at three different pump-probe time delays. The curves are normalised to the unperturbed spectrum at t_1 (blue). At $t_2 = 20\,\text{fs}$ (red) the atto-MCD contrast is already reduced by almost 30%, after several hundred femtoseconds $t_3 = 200\,\text{fs}$ (green) the atto-MCD contrast has lost more than half of its amplitude. Initial publication in [81].

The experiment was conducted in a way that in a first step, the atto-MCD contrast as defined in Eq. 3.3, was recorded at three different delay times between the NIR pump and the XUV probe pulse, see Fig. 3.10. The first instant is in the absence of NIR laser light t_1. A second trace is recorded about $t_2 = 20\,\text{fs}$ after the interaction of the sample with the pump pulse followed by a third measurement at a delay of $t_3 = 200\,\text{fs}$. This proves the technique's capability to track fast variations in the magnetic moment of the studied species.
In Fig. 3.10, it is evident, that nickel, within a Ni/Pt multilayer system, changes its

magnetic moment already within the first 20 fs. The atto-MCD contrast is normalised to the unperturbed case indicating a reduction of the magnetic moment of 30% after 20 fs and up to 70% after the laser pulse has passed. As the signal amplitude gets weaker for longer delays, the noise becomes more pronounced, making exact quantitative statements unreliable.
These results demonstrate the capability of the measurement technique of mapping element-specific changes in the magnetic moment in a time-resolved manner.

3.4.1 Sub-fs Quenching of the Magnetic Moment

To get a better understanding of the involved effects and to distinguish them, a closer look has to be taken at the early time evolution during and right after the light-matter interaction. Due to the long timescale instabilities of the measurement, as mentioned above, the investigated time window is limited to 9 fs. In Fig. 3.11, the main findings of this work are shown. The dashed red line represents the light-induced change in XUV transmission, as explained before. The sub-cycle evolution is clearly visible and indicates the arrival time of the driving laser pulse.
In blue the atto-MCD contrast Δ_{M} is shown, the value is taken from the peak region of Δ_M, as shown in Fig. 3.10 at around 67 eV. The laser pulses used for these measurements had a duration of $\tau_{\mathrm{NIR}} < 4$ fs and a peak intensity of $I = 4 \times 10^{12}\ \frac{\mathrm{W}}{\mathrm{cm}^2}$. The shaded areas represent the standard deviation, 95% confidence interval. This graph clearly shows that even in the first sub-10 fs, the atto-MCD contrast, hence the magnetic moment of nickel is quenched by up to 40% when looking at the delay of -3 fs it might even quench on a sub-fs time scale. The synchrony of light-induced electron redistribution, manifesting in XUV transmission change, and the reduction of magnetic moment indicate a manipulation of magnetism that is driven by photons. As there is no first-order coupling of photons and spins, a different effect has to be responsible for this effect. The Δ_{M} signal shows some oscillatory behaviour. However, commenting on these oscillations is pure speculation as they lie outside the experimental certainty.

In the course of finding the responsible process leading to the rapid change of magnetisation, a control experiment with a different sample, however, otherwise exact same experimental conditions was conducted. The Ni/Pt multilayer sample was exchanged with a pure nickel thin-film sample (8 nm) that has also been used for the measurements of the electronic response as shown before, Fig. 3.8.
Again the red dashed line represents the change of the XUV transmission manipulated by the intense laser pulse. Although the sub-cycle evolution is not as prominent in this measurement, it is sufficient to estimate the arrival time of the laser pulse. The blue line shows the temporal trend of the atto-MCD contrast Δ_{M}. Here in striking contrast to the multilayer sample, the magnetic moment of nickel stays, within the error of the measurement, constant during the time where the sample interacts with the strong electric field of the laser.
The missing heavy metal ad-layer of platinum seems to hinder the rapid manipulation of the magnetic properties of the ferromagnetic layer. As the magnetic moment is mostly

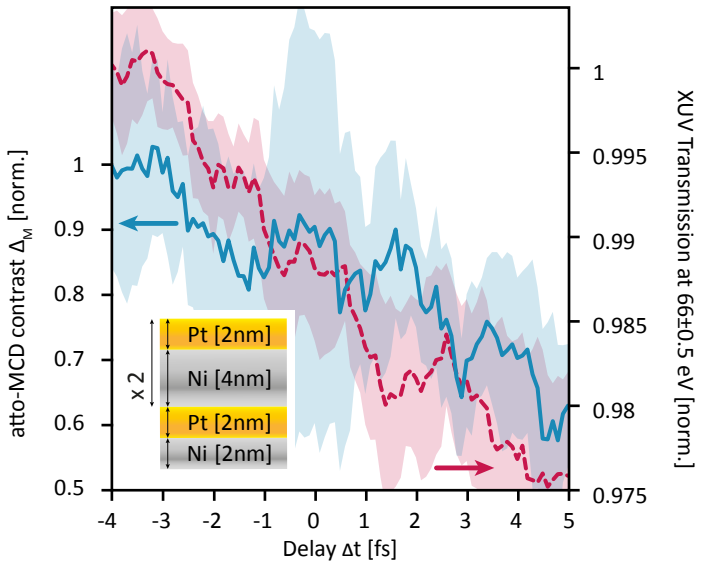

Figure 3.11: The XUV transmission of a Ni(2 nm)/Pt(2 nm)/[Pt(2 nm)/Ni(4 nm)]x2 multilayer array (dashed red line) changes in the previously shown sub-cycle manner, see Fig. 3.9. At the same time the atto-MCD contrast Δ_M of the array (solid blue line) decreases by ∼40%. This loss of magnetic moment happens during the presence of the NIR laser pulse within a few femtoseconds. A change of the magnetisation on this timescale has not been seen before. The shaded areas depict the respective standard deviation. Initial publication in [81].

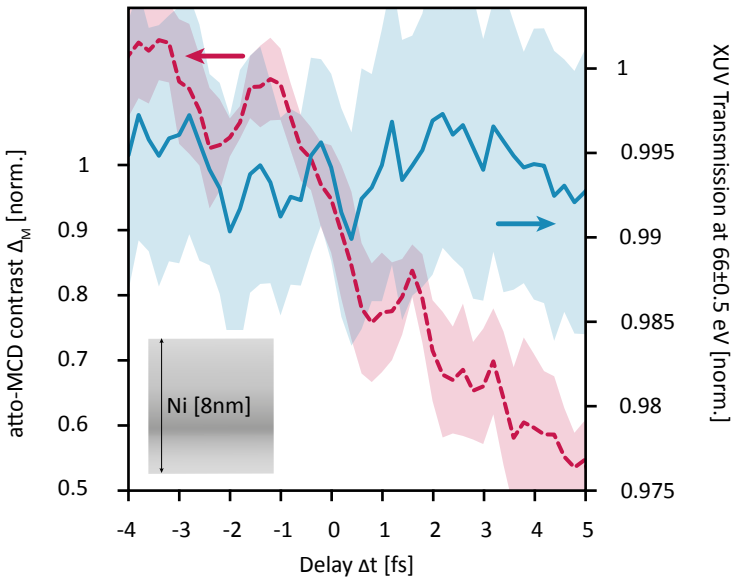

Figure 3.12: The XUV transmission of an 8 nm nickel slab (red) changes during the interaction with a strong laser pulse, compare Fig. 3.9. At the same time the atto-MCD contrast (blue) stays unchanged. The absence of the sub-fs loss of magnetic moment in nickel indicates that the previously seen effect in the Ni/Pt is sample specific and must root in the multilayer structure. The shaded areas depict the respective standard deviation. Initial publication in [81].

governed by the orientation of the electrons' spin, this unprecedented behaviour has to be attributed to a change of the spins in the material.

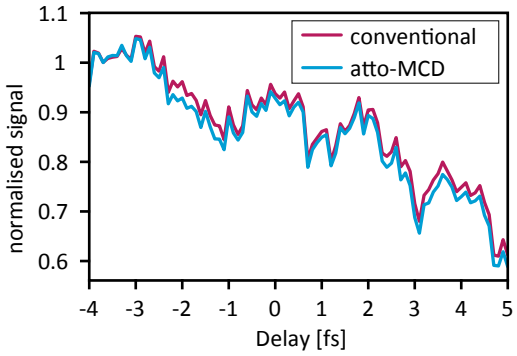

Figure 3.13: The comparison of the time-evolution for the analysis using the conventional-MCD type and the atto-MCD. The signals are basically identical, with a few small discrepancies.

Fig. 3.13 shows the comparison of the temporal evolution of atto-MCD and conventional MCD. The two traces look fairly identical with a few minor discrepancies. However, proving that the effect is indeed real and on that magnitude and not owed to the evaluation.

3.4.2 Long Timescale Behaviour of the Magnetic Moment

The question arises what happens after a few tens of femtoseconds. Do the samples level up in the change of the magnetic moment or does the early induced reduction manifest and last? Measurements were performed where the delay steps were chosen longer, on the order of 1 fs with a delay axis of up to 200 fs, to answer that question. The results of this measurement are shown in Fig. 3.14.
The figure shows the atto-MCD contrast Δ_{M} normalised to time zero for the two different samples. The measurements were done at a peak intensity of $2 \times 10^{12}\,\frac{\mathrm{W}}{\mathrm{cm}^2}$, slightly lower compared to Fig. 3.11 and 3.12. Nevertheless, this set of data shows exactly the same behaviour qualitatively. The multilayer sample responds fast to the strong laser electric field, whereas the nickel slab does not show a rapid decay. Notably, nickel exhibits a small drop of the magnetic moment ($< 5\%$), consistent throughout a series of measurements, which could not be observed that precisely in the close-up scans. This might be on account of longer integration times and generally more stable laser performance, due to the absence of the necessity to run it with a locked CE-phase.
After the initial change, the multilayer sample seems to stay in a plateau regime (10 to 35 fs), before decaying further. Nickel, however, starts to rapidly change its magnetic moment after around 30 fs, reaching the same level as Ni/Pt and then decaying at the same rate. At around 40 to 50 fs, where the change of magnetisation is independent of

the sample, the driving processes can be attributed to the interaction of electrons and spins through phonons.

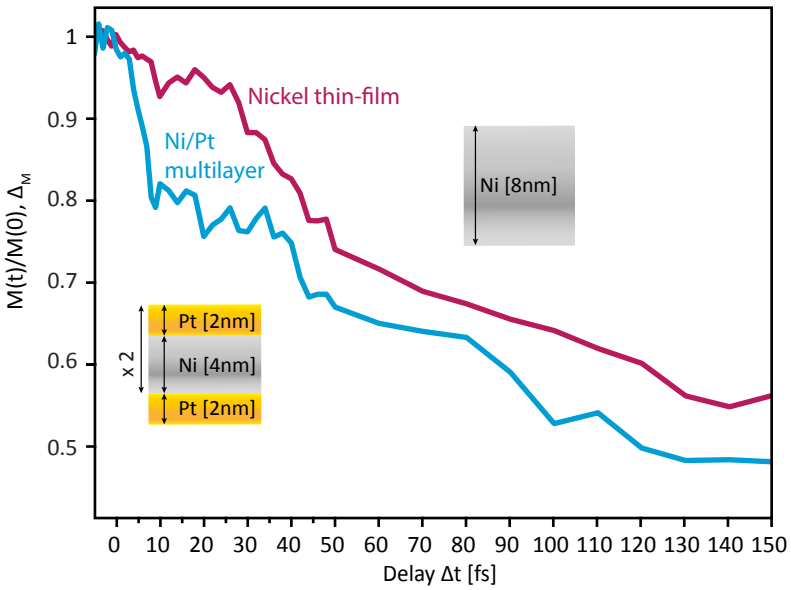

Figure 3.14: The long timescale behaviour for the two samples is shown. Multilayer (blue) exhibits a steep, rapid decrease as established in the short timescale measurement, whereas nickel slab (red) stays more or less constant in the first few femtoseconds. After 30 fs nickel's magnetic moment changes and from there on the demagnetisation appears to happen at comparable rate.

3.4.3 Comparison with TDDFT Calculations

In order to distinguish the different processes which mediate the quenching in the early stage, a full TD-DFT calculation was performed. The calculations were done by Sangeeta Sharma (MBI Berlin) using the open-source ELK code [87]. The *ab-inito* calculations give the magneto-optical function of the system. The imaginary part of the magneto-optical function is half of the conventional MCD signal [88]. The two parameters are compared in Fig. 3.15.

The two curves look similar in terms of the pre-edge feature between 62 eV and 66 eV and also agree at the main MCD peak in both magnitude and width.

The left panel of Fig. 3.16 shows five curves, the red ones correspond to nickel and the blue lines correspond to the Ni/Pt multilayer. For the nickel slab, the TD-DFT calculation (dashed-dotted line) shows a small decrease in the magnetisation of a few percent. The experimentally recorded trace, although seeing a slightly larger loss of magnetisation ($\approx 5\%$), reproduces that behaviour up to 30 fs. Here the first lattice contribution and the onset of phonons might lead to spin flips and a loss of magnetic order. Such dynamics cannot be accounted for by the calculation and may cause the discrepancy.

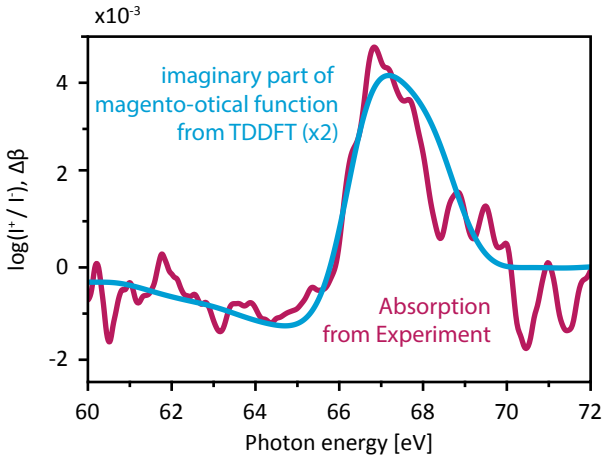

Figure 3.15: The TD-DFT calculation provides the magneto-optical function (blue). Its imaginary part is proportional to the the dichroic signal. The experiment gives the attosecond MCD contrast or the conventional MCD signal. Here the conventional MCD $\mu^+ - \mu^-$ is shown. The magneto-optical function has to be corrected by a factor of 2 [88].

In the case of the multilayer, the solid line depicts the experimental results. For the calculations, there are two results, one trace where the treatment is complete and one where the spin-orbit coupling is turned off (see labels). When the spin-orbit coupling is turned on the calculated trace agrees with the experimental data, in both temporal evolution as well as in magnitude. Turning spin-orbit coupling off makes the calculated signal level off after 10 fs, with only half the amplitude, compared to the full calculation. This means that the initial drop ($0 - 10$ fs) does not depend on the spin-orbit coupling. A different mechanism has to govern this early magnetisation change during and after laser excitation. Dewhurst *et al.* found a process where electrons and their spins coherently migrate from the ferromagnetic to the paramagnetic site, where their spin is absorbed. They named it *optically induced intersite spin transfer* (OISTR) [79]. This measurement shows that this process exists and is capable of changing the magnetic moment at unprecedented speed.

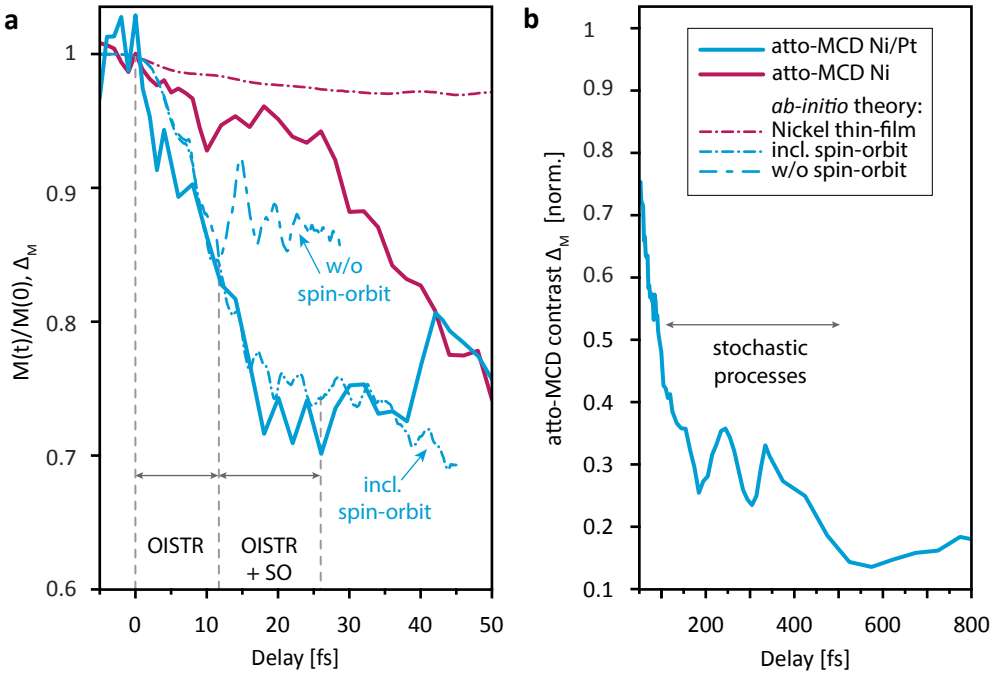

Figure 3.16: The experimental data is displayed by the solid lines, multilayer in blue, nickel slab in red. Results from TD-DFT calculation are plotted in dashed and dashed-dotted lines. The agreement for nickel slab is satisfactory up to 30 fs. For the multilayer sample, two scenarios are shown, full calculation and calculation without spin-orbit coupling. In the first few femtoseconds the two curves overlap excellently. Only after 10 fs, a further loss of magnetic moment can be observed in the full calculation. In the left panel the complete loss of magnetic moment in the multilayer after around 500 fs is shown. Initial publication in [81].

3.4.4 Optically Induced Intersite Spin Transfer

The spin selective charge transfer occurring during the interaction of the multilayer sample with the intense laser pulse can be very well understood when looking at the DOS diagram in Fig. 3.17. The calculated DOS for nickel (grey) and platinum (gold) is shown. Nickel exhibits, due to its ferromagnetic nature, a strong Stoner splitting between the DOS for spin-up and spin-down. This splitting leads to an imbalance of unoccupied states between the two spin directions. Platinum's DOS, however, is only slightly influenced by the external magnetic field, due to its paramagnetic characteristics, leaving the unoccupied states not spin selective.

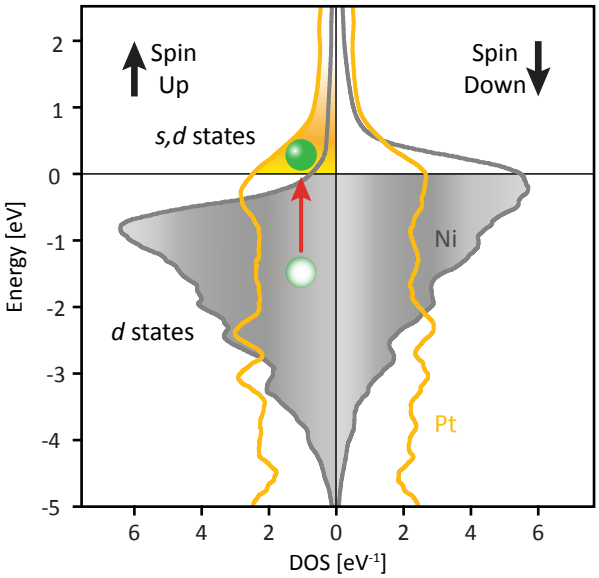

Figure 3.17: The calculated DOS for nickel (grey) and platinum (yellow). Nickel has unoccupied states for spin-down, whereas, for spin-up, nearly all states are occupied. For platinum, unoccupied states exist independently of the spin direction. This opens an excitation path for the spin-up electron from nickel into platinum (red arrow). Initial publication in [81].

As soon as the strong electric field of the laser pulse interacts with the sample, majority carriers with spin-up get excited, but the number of empty spin-up states in nickel is smaller than in platinum. For that reason, electrons with spin up migrate across the interface from the ferromagnetic into the paramagnetic layer. This transfer leads to a reduction of majority carriers, thus a reduction of the magnetic moment. At the same time, electrons from platinum can also transfer from the one into the other domain. However, as platinum has heavy spin-orbit coupling, the electrons leaving platinum do not have a distinct orientation of their spin. So these electrons cannot compensate for

the loss of magnetic moment induced by the migration of the majority carriers. Note that the net charge stays constant and no polarisation due to charge flow is induced.

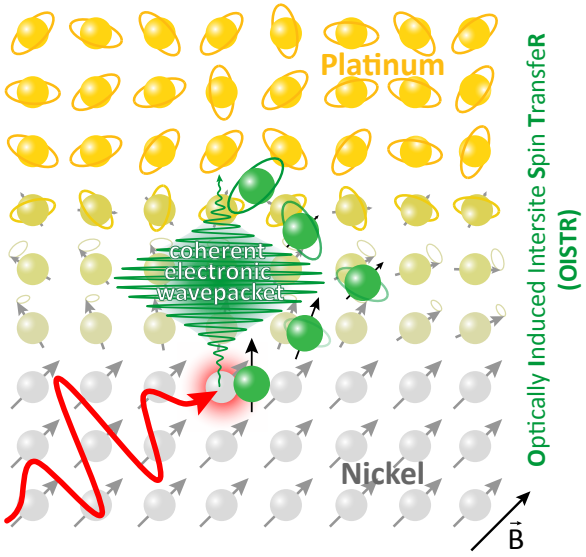

Figure 3.18: Semiclassical picture of OISTR. The spins of the electrons in nickel (grey) are aligned along the external magnetic field, in platinum strong spin-orbit coupling hinders the alignment of the spins. A laser pulse excites a coherent electron wavepacket across the interface, reducing the magnetic moment in nickel. Initial publication in [81].

Another way of looking at the OISTR process is a semiclassical somewhat real-space picture, as illustrated in Fig. 3.18. The spins of the unpaired $3d$ electrons in nickel align along the external magnetic $\vec{B}$ field. In platinum due to strong spin-orbit coupling, all angular momentum is stored in orbital momentum. The laser pulse (red) excites an electron in nickel and creates a coherent electron wavepacket (green) that can travel across the interface where it then can populate an empty state. Vice versa an electron wavepacket from platinum can propagate into nickel. As it does not have a distinct spin orientation, it does not contribute positively to the local magnetic moment.
It is worthwhile to mention that the OISTR process does not overcome fundamental limitations connected to spin flips and spin rearrangements. In OISTR the local magnetic moment of one species gets manipulated by moving charge carriers and their spins coherently.
The theoretically predicted OISTR process that leads to a change of the local magnetic moment in a ferromagnet on the timescale of the pulse duration of the driving few femtosecond pulse is experimentally confirmed here. This intersite transfer of carriers is happening on sub-exchange and sub-spin-orbit timescales. Note that this effect is a pure interface effect between two different domains. However, they are not necessarily ferromagnetic and paramagnetic, but can also be, e.g. ferromagnetic-ferromagnetic or ferromagnetic-antiferromagnetic. This will be further discussed in section 3.6.

3.5 Determination of $\langle L_z \rangle$ and $\langle S_z \rangle$ from the Sum Rules

The sum rules allow the measurement of spin and angular orbital momentum from MCD signals. Recently, these sum rules were applied to time-resolved measurements [14,66,89] to access the temporal evolution of the quantum numbers $\langle S_z \rangle$ and $\langle L_z \rangle$ during ultrafast demagnetisation. These pioneering experiments in the field of ultrafast magnetism were the first ones to apply the sum rules to time-resolved measurements. In all three studies, both $\langle S_z \rangle$ and $\langle L_z \rangle$ reduce their magnitude after the laser excitation. Interestingly the processes happen on different timescales for the two quantum numbers. This raises the question what determines the different timescales of $\langle S_z \rangle$ and $\langle L_z \rangle$ and how they behave during or directly after laser excitation. The temporal resolution of the studies so far lacked single femtosecond resolution and therefore, insights into the early stage of interaction was not gained. However, especially this early stage of the demagnetisation is of major interest. On these short timescales the lattice is quasi inactive as it reacts much more slowly and therefore does not contribute to the demagnetisation. The whole loss of magnetic moment is owed to electronic processes.
As angular momentum conservation dictates, the whole system has to have a conserved angular momentum.

$$\vec{J}_{\text{total}} = \vec{L} + \vec{S} + \vec{J}_{\text{lattice}} \tag{3.9}$$

where $\vec{J}_{\text{total}}$ denotes the total angular momentum, $\vec{L}$ the orbital angular momentum of the electrons, $\vec{S}$ the spin angular momentum and $\vec{J}_{\text{lattice}}$ the angular momentum of the lattice.
Consider, that at early times the lattice is unperturbed as it is too slow to react within a few femtoseconds, this eliminates $\vec{J}_{\text{lattice}}$ in Eq. (3.9). This means that the change in the system must be governed by $\vec{S}$ and $\vec{L}$. In this context, the sum rules are applied here, as described in chapter 2.4.
The sum rules are given by Eq. (2.39) and (2.40).

$$\langle L_z \rangle = \frac{2}{3} \frac{n_h}{P_c cos\theta} \frac{\Delta Q_3 + \Delta Q_2}{Q_3 + Q_2} \qquad \langle S_z \rangle = \frac{1}{2} \frac{n_h}{P_c cos\theta} \frac{\Delta Q_3 - 2\Delta Q_2}{Q_3 + Q_2} \tag{3.10}$$

For a detailed discussion of the formula, look at chapter 2.4. It was also discussed there that for the orbital sum rule, the overlap of the two levels is not relevant as the integral is taken over the sum of both absorption edges, see Fig. 2.6. For the spin sum rule, this does not apply. Therefore, the deconvolution of the two edges is important, as well as the right choice of the boundaries for the integral. The spin sum rule will underestimate the magnitude of $\langle S_z \rangle$, when the two absorption edges of the two levels overlap, again see Fig. 2.6.

For the deconvolution of the measured absorption spectra, the help of theoretical calculations is needed. Fig. 3.19 compares the calculated and measured absorption. Although the overall agreement is not good, the dichroic features are present in the calculation at the same position, one at $\sim 66\,\text{eV}$ and one slightly above $68\,\text{eV}$.
Calculations can be performed only considering one of the two transitions, e.g. $3p_{3/2} \rightarrow 3d$. Such a calculation can be done for both helicities, as is shown in Fig. 3.20. The

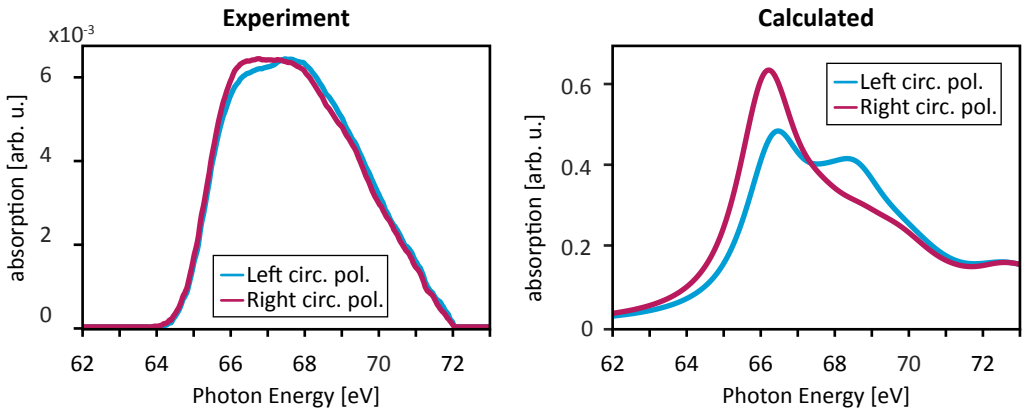

Figure 3.19: The experimentally obtained absorption spectrum (left) and calculated one (right) for opposite helicity. The experimental data shows dichroism of a few percent of the total absorption. The calculated spectra show the pronounced absorption peaks from the $3p_{1/2}$ and the $3p_{3/2}$ core level and an overall stronger dichroism. Both datasets show the main features of the dichroism. For both spectra the background is subtracted.

upper part shows the calculated absorption spectra together with the absorption spectra for only one of the core levels (purple and green). It can be seen that $3p_{1/2}$ and the $3p_{3/2}$ are not pure states but that their wavefuncitons mix, because each absorption spectrum has contributions from the other level.

The separation can be used in the context of the MCD sum rules Eq. (3.19) to decompose the measured spectra into contributions from $3p_{1/2}$ and the $3p_{3/2}$. Afterwards the dichroic signal for each core level can be calculated and then used, as described by the sum rules to calculate $\langle S_z \rangle$ and $\langle L_z \rangle$.
The lower panels of Fig. 3.20 show how the experimentally obtained data is separated into two parts. The individual parts agree quite well with the single level absorption spectra plotted in the upper panel.
With these spectra it is now possible to apply the sum rules to measured data. The result of this is plotted in Fig. 3.21. The following discussion is done under the premise that both sum rules are valid, although this can be doubted (chapter 2.4).
The results indicate an increase of L_z after laser excitation and a decrease after $\sim 30\,\text{fs}$. In contrast, as L_z increases, S_z seems to decrease rapidly and after $\sim 30\,\text{fs}$ converges slowly towards 0. This would support the theory that the system immediately reacts to external distortion, due to the laser pulse, by a rearrangement of the magnetic moment. Then after $\sim 30-50\,\text{fs}$ the lattice starts to move and L_z and S_z decrease simultaneously.

The magnitude of L_z and S_z, is due to all the assumptions made in the theory part, most likely not accurate. Therefore the plot is in arbitrary units. $\langle S_z \rangle$ is underestimated in any case.
The results are nonetheless impressive, the behaviour these measurements indicate would

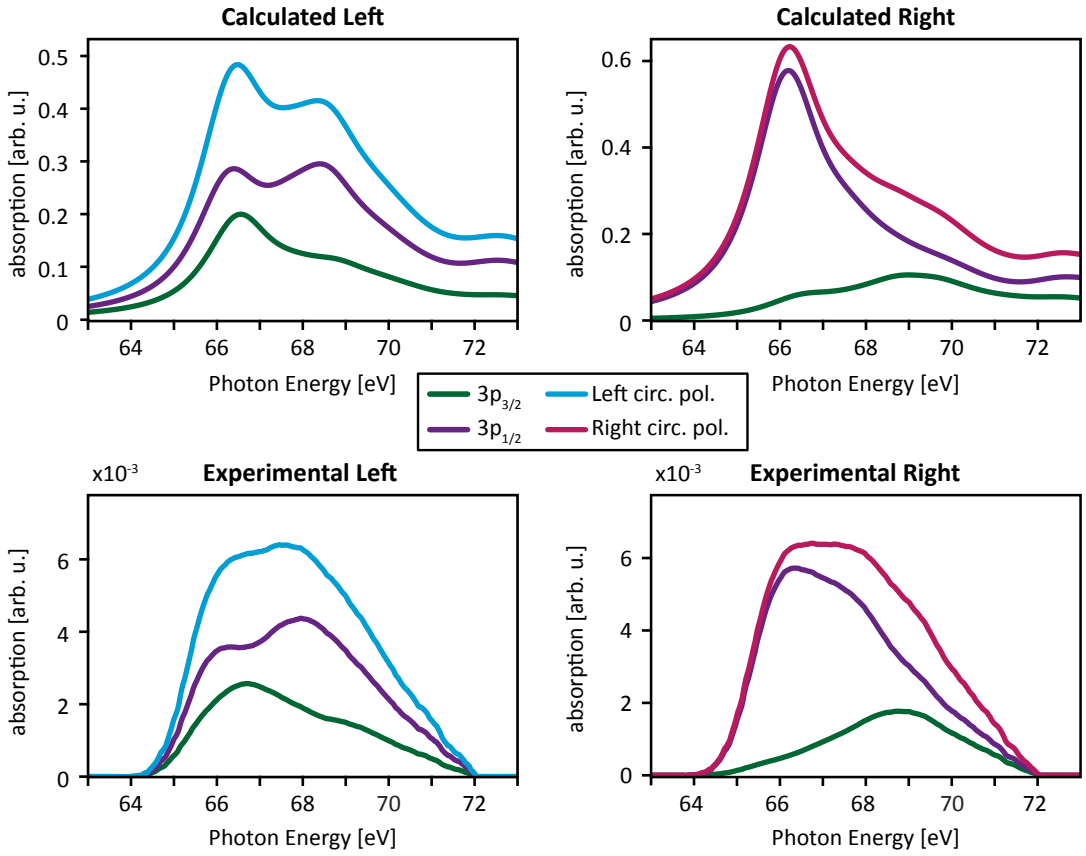

Figure 3.20: The calculated spectra can be decomposed into contributions from the two spin-split core levels $3p_{1/2}$ (green) and the $3p_{3/2}$ (purple). Due to the mixing of the states' wavefunctions each absorption spectrum has contributions from both levels. The splitting ratio is then applied to the recorded absorption spectra (lower panels). Although in Fig. 3.19 the spectra do not agree too well, the calculated ratios applied to the recorded spectra look very much alike.

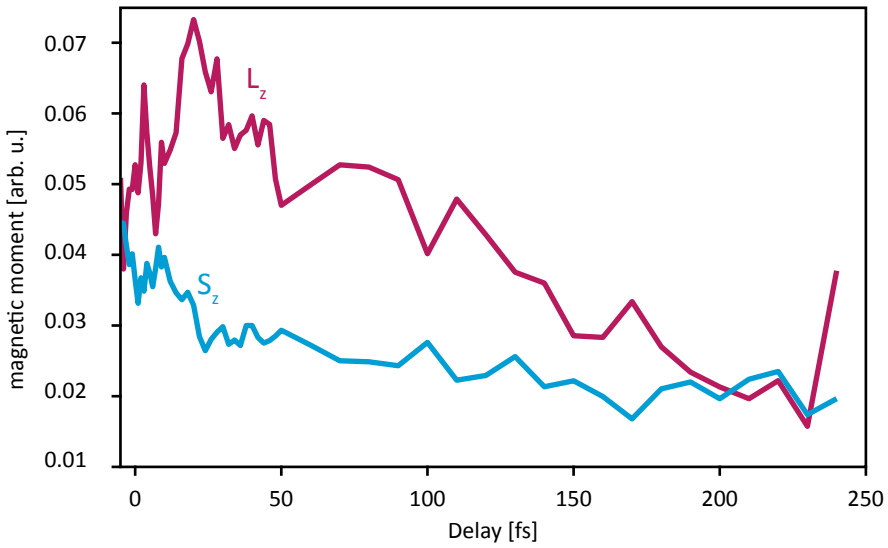

Figure 3.21: The early time evolution of S_z and L_z. Shortly after the interaction L_z seems to increase and almost doubles its numeric value. However S_z stays constant or slightly decreases after the initial excitation, and then after 15 fs starts to decrease. Also L_z decreases after the initial increase and levels with S_z after 200 fs.

allow a deeper understanding of the demagnetisation process. Moreover, in a multilayer system, as used for the OISTR measurement, it might be able to track the spin transfer manifesting itself in the time-evolution of $\langle S_z \rangle$ and $\langle L_z \rangle$.

3.6 Main Findings and Future Tasks

In this chapter, a manifold of novelties was presented. To start off with attosecond transient absorption measurements in a metallic system, in the presented case, nickel. It was shown that a change of the electronic state can be introduced by a few-cycle near-infrared laser pulse. This was manipulation manifested itself in the change of the XUV transmission of the sample. This was done with such great temporal resolution that the sub-cycle contributions due to the oscillating electric field could be resolved.
Furthermore, the relaxation of this perturbation was be successfully tracked, showing that this process indeed recovers with several hundreds of femtoseconds.
These experimental findings were obtained on the way to the actual goal of this study. The measurement of manipulation of magnetisation on a few- or even sub-femtosecond timescale. By the use of a tailored multilayer sample consisting of ferro- and paramagnetic materials, this was successfully measured. In the mentioned system, a change of the magnetic moment of the ferromagnetic material was recorded. This change happens synchronously with the electronic response of the system. Moreover, it was found that this change of magnetisation can be attributed to a process named OISTR, which describes the transport of charge carriers and their spin across an interface. This was backed up

by a control measurement, where no interface, which supports transport process, was present. Therefore the magnetisation could not be changed during the interaction of the sample with the laser pulse.
These findings were followed by an approach to retrieve information about the quantum numbers S_z and L_z that describe the spin angular and orbital angular momentum. Connecting MCD measurements to the quantum numbers through the so-called sum rules is an established method and has been done before. Here the novelty was to apply these sum rules to M- instead of L-edges and look at the temporal evolution.

For the future there are many possibilities to further develop the presented results. Regarding the electronic response a more thorough study could be done using attosecond transient absorption. Looking closer at the intensity scaling and the relaxation dynamics might enable insights into the driving effects of excitation and relaxation. Also considering a follow-up experiment that uses the attosecond polarisation sampling technique could be of interest. Attosecond polarisation sampling is mainly sensitive to states around the Fermi energy (no core levels involved), which makes it easier to model with, e.g. TD-DFT.
The magnetisation study offers many possibilities for new experiments. First of all a general improvement of the atto-MCD measurement technique with higher photon flux, leading to better signal-to-noise ratio would be highly useful for the experiment and the possible conclusions. However, this is rather a technological challenge than related to physics. From this perspective it is of large interest to use a system where the absorption edges of both elements of the multilayer can be tracked by attosecond transient absorption. As the magnetic moment in constituent changes, this should also have an influence on the other one. Probing both elements at the same time should give information about the whole system e.g does the magnetisation increase in one while it decreases in the other and how long the total magnetisation is conserved. Suitable systems for that might be CoPt or Heusler alloys [90].
Additionally, to follow-up on the sum rules and the measurement of the spin and orbital angular momentum future free-electron lasers (FEL) with attosecond resolution might provide the right infrastructure to measure it, as FELs give access to the L-edges of the transition metal elements.

Chapter 4

Electronic Excitation and Magnetic Circular Dichroism in Nanoparticles

Over the past decades, nanoparticles have emerged as a vivid and quickly growing research field. Due to their small size, typically $1 - 100\,\mathrm{nm}$ and therefore low number of atoms ($N \approx 10^5 - 10^8$), nanoparticles can behave fundamentally different than their corresponding bulk material. With size, shape and composition as tunable parameters, many phenomena have been observed, making them the subject of a vast amount of studies, e.g. in ultrafast optics, magnetism, and as well as in catalysis [91–93].
The study was performed in close collaboration with *Dr. Florian Lackner* (TU Graz). Different nanoparticles, all of them containing nickel, have been studied and compared with the results from the bulk-like experiment of the previous chapter.

4.1 Synthesis of Nanoparticles

In this study, two types of nanoparticles were investigated: spheres and nanowires. Both of them can be fabricated in a core@shell fashion [94]. This means that the particles consist of a core of one element, fully enclosed by a shell of a second constituent. Spherical core@shell nanoparticles can be synthesised using different approaches, e.g. through annealing with a femtosecond laser or galvanic exchange in a solution [95,96]. Nanowires can be fabricated using ligand control or oriented attachment [97,98]. A technique that is capable of providing the core@shell structure, as well as the nanowire dimensionality, uses superfluid helium nanodroplets. The fabrication scheme is shown in Fig. 4.1 [94].
In a first vacuum chamber, cryogenically-cooled helium ($T_{He} \approx 4\,\mathrm{K}$) is evaporated through a nozzle with a diameter of a few micrometres, where the geometry of the nozzle defines the size of the droplet. A skimmer collimates the single droplets, defines their propagation direction and focusses them into a beam into the second chamber.

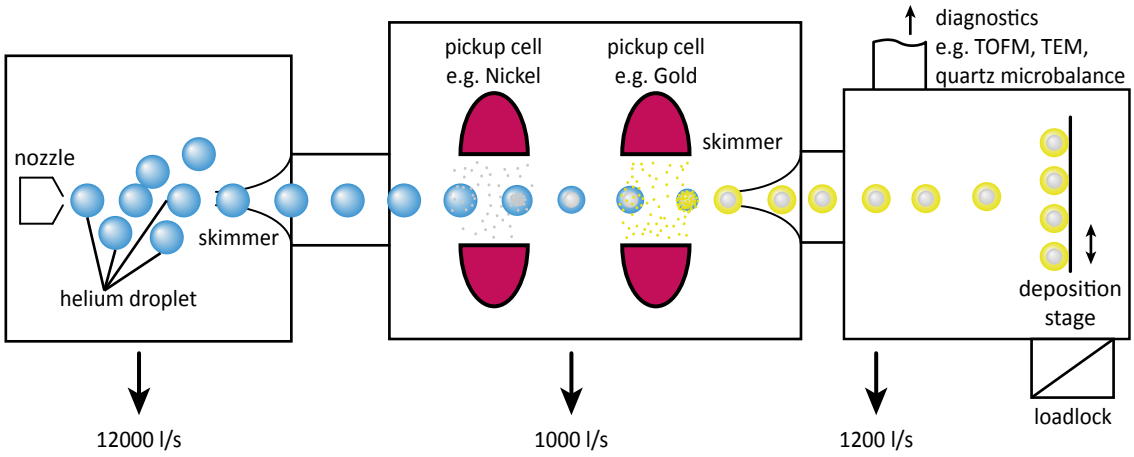

Figure 4.1: A nozzle in a vacuum chamber emits superfluid helium nanodroplets. A skimmer focusses them into a second chamber where they pass several pickup cells, equipped with, e.g. nickel and gold. The helium nanodroplets absorb the particles, which form clusters. Due to evaporation, the size of the nanodroplet reduces until there is no helium left. In a third chamber, the fabricated nanoparticles are deposited onto a substrate and can be removed from the vacuum. Several diagnostic tools allow for the characterisation of the particles. Every chamber is equipped with vacuum pumps (indicated by the arrows and the pump volume) to reduce background pressure and eliminate contamination of the nanoparticles.

In the second chamber, the actual nanoparticle is created. Several pickup cells are equipped with dopants and allow for different core@shell structures. The dopants, liquid or gaseous, collide with the nanoparticle and are absorbed by the helium droplet. During the propagation of the droplet, it can pick up several thousands of atoms. While the atoms are being incorporated, they start to form clusters and by doing so, release binding energy. The emitted binding energy is absorbed by the helium nanodroplet, leading to the evaporation of helium atoms. Therefore, the size of the helium droplet determines the final size of the nanoparticle.
After passing the second chamber, the formation of the nanoparticles is finished. In the third chamber, they can be deposited onto a substrate and then extracted from the vacuum. Several diagnostics allow for characterisation of the generated particles.

For this study, three different types of particles were produced. The following table summarises the important parameters.

Sample number	Type	Material	Substrate Coverage
I	nanowires	pure Ni, oxidised to NiO	30%
II	nanowires	Ni@Au (Ni core, Au shell)	70-100% (20-30% Ni)
III	spherical particles	Ni@Au	40%

4.2 Experimental Results

The measurements were performed in the AS2 beamline, using the same setup as is shown in Fig. 3.3. In the static absorption measurements, the polarisation of the XUV was set to linear polarisation for maximised photon flux through the phase retarder.

4.2.1 Static XUV Absorption Measurements

To examine whether an attosecond XUV source is capable of resolving element-specific information of such small particles, the static XUV absorption of each of the three samples was measured. The results are plotted in Fig. 4.2.
The graph shows the optical density (OD) of each sample. The OD is chosen over the absorption coefficient μ, as the propagation length, due to the varying coverage, is not well defined.
The first notable feature in the absorption is the more than a factor of two higher OD for sample II. The enhanced OD stems from the almost full coverage of the substrate with the Ni@Au nanowires. Qualitatively, sample II and III exhibit almost the same characteristics, the onset of the absorption edge slightly below 66 eV, as well as the increased absorption towards lower photon energy. Although the M-edge is less pronounced, it energetically overlaps, in position and width, very well with the nickel thin-film data.

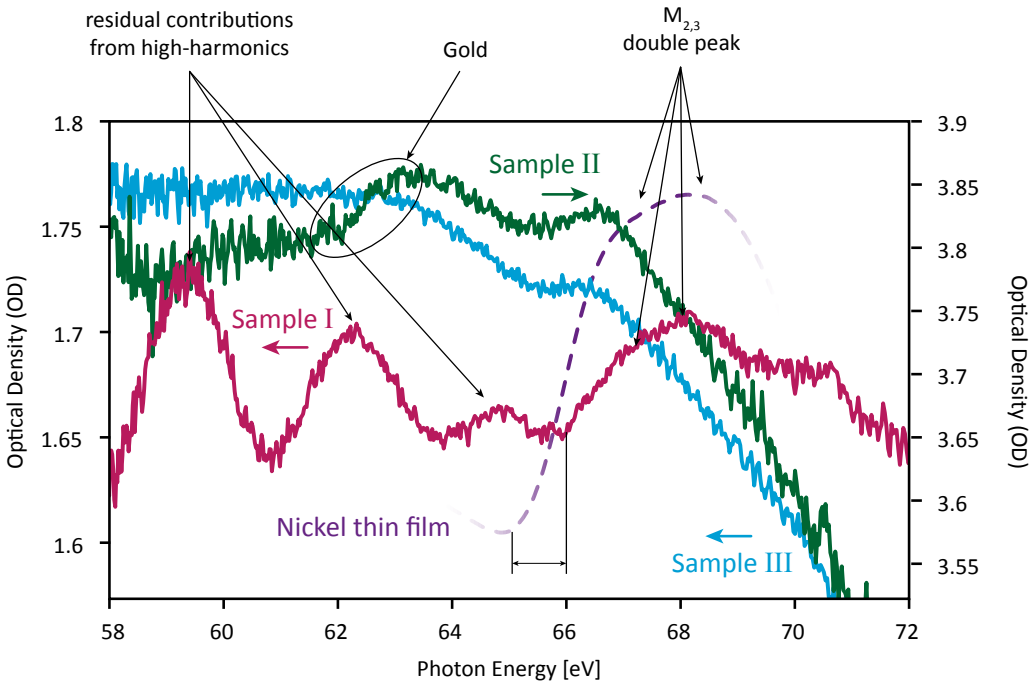

Figure 4.2: The optical density (OD) as a function of photon energy for three samples. Blue and red lines use the left y-axis, while green uses the right y-axis. The dashed purple line is data from the previous chapter from a nickel thin-film. The nickel $M_{2,3}$-edge is most prominent in the data from sample I. The curve corresponding to sample I also shows three peaks that are marked at $\sim 59\,\mathrm{eV}$, $\sim 62\,\mathrm{eV}$ and $\sim 65\,\mathrm{eV}$, their spacing indicates that they are some residual harmonics and appear due to some drift. Sample II and sample III do not exhibit such a pronounced nickel edge owing to their size and low coverage on the substrate. Moreover, sample II shows a contribution from the gold cladding at around $62\,\mathrm{eV}$. The shift indicated by the black lines is due to a chemical shift caused by the oxidisation of the nickel.

Also, sample II exhibits a slightly increased OD in the range between 62 and 64 eV, which can be attributed to absorption in the nanowires' gold cladding.
In sharp contrast, sample I shows an entirely different structure. The curve that is shown corresponds to an integration time of 800 s ($\approx$ 13 min), whereas the integration time for sample II was 300 s and for sample III 200 s respectively.
Sample I strongly absorbs at the M-edge and even displays the double-peak structure due to the spin-orbit split $3p$-level, as can be seen in the nickel thin-film data. The spacing of the three peaks at low photon energy indicates that they have their origin in the high-harmonics. In the calculation of the absorption this modulation should cancel, however, small drifts in the high-harmonics spectrum could be the reason for this.
In comparison with the nickel thin-film data, the absorption is shifted towards higher photon energies. The nickel particles have oxidised to some degree, making them Ni@NiO spheres. The oxidisation introduces a chemical shift of the absorption edge towards larger binding energies [99].
The table-top XUV attosecond source is in principle capable of measuring absorption spectra from dispersed nanoparticles on a substrate. The low repetition rate, together with low photon flux, compared to, e.g. a synchrotron source, lead to noisy spectra and long integration times. However, the significant advantage over such facilities lies in the unprecedented temporal resolution an attosecond beamline can provide. This will be utilised for time-dependent absorption studies in the following section.

4.2.2 Transient Absorption Spectroscopy

The transient behaviour of the nanoparticles during the presence of a strong electric laser field was studied as described in chapter 3.3. The XUV transmission of the nanoparticles was measured while a short, intense laser pulse manipulates the electronic structure of the particles. By introducing a varying time delay between the two beams, the time-dependent change of the XUV absorption is recorded.
Fig. 4.3 shows the results of this study for sample I. The left panel focusses on the fast dynamics, whereas, the right panel shows the slower recovery. The recorded data exhibits strong noise, due to the small overall absorption in combination with the small relative changes of this signal. Long integration times can increase the signal to noise ratio (S/N) to a certain extent. Unfortunately, longer integration times limit the minimum step width of the delay axis to 0.5 fs, in order not to exceed the period of stable laser operation.
Nevertheless, the measurement shows a distinct transient change in the XUV transmission of $< 1\%$. This is rather small compared to the 3-4% in the thin-film and multilayer sample in chapter 3.3; however, the structure of the nanoparticles is significantly different, making a varied response plausible.

Especially the long-timescale behaviour looks familiar. The initial, almost instantaneous drop is followed by a quick recovery of the electronic system within a 1 ps. This is again in good qualitative agreement with the results obtained from the bulk and thin-film sample.

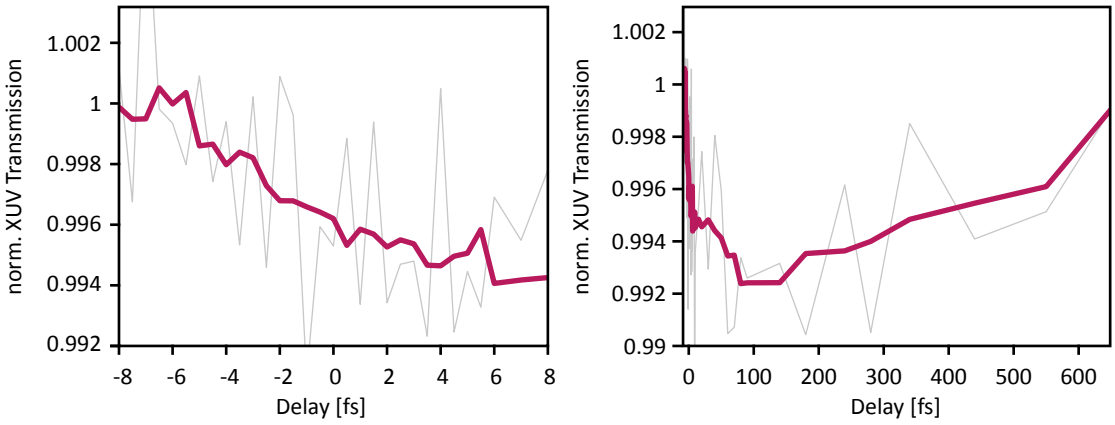

Figure 4.3: The temporal evolution of the XUV transmission of sample I. The panel on the left shows short time evolution, the panel on the right shows the long time scale. Thin lines represent raw data; thick lines are an adjacent average over seven points.

One reason for the discrepancy in the magnitude of the change of the transmission might be different intensity settings for the optical excitation of the nanoparticles. The parameters known from the experiments on the nickel bulk and multilayer sample turned out to be too high and damaged the sample. This issue was resolved by using lower intensities ($\approx 8 \times 10^{11} \frac{\mathrm{W}}{\mathrm{cm}^2}$), which then led to a smaller change of the XUV transmission. A possible reason for the lower damage threshold might be the thermal contact between the silicon substrate and the nanoparticles compared to an evaporated thin film. The spherical shape prohibits a large contact area between particle and substrate not providing sufficient heat transport away from the laser-excited nanostructures.

For sample II and III, the same experiment was performed, giving a similar trend, shown in Fig. 4.4.
Comparing with chapter 3, the results from samples II and III confirm the earlier mentioned effect of a small drop of the XUV transmission. The effect is smaller ($\sim 0.5\%$), nevertheless, it is possible to see the decrease even in the raw data (thin blue line). Applying an adjacent average filter to the data pronounces the effect.

4.2.3 Magnetic Circular Dichroism of Nanoparticles

The central part of this thesis revolves around the measurement of magnetic circular dichroism in samples containing nickel. This is also the reason why nickel was chosen as one of the nanoparticles' constituent. For the absorption measurement, the nanoparticle study already benefited from the knowledge of the bulk and thin-film measurements. The question now was, if the nanoparticles also show dichroic behaviour.
The experiment closely followed the protocol developed for the measurements in the previous chapter. The absorption was measured for alternating magnetisation, and the

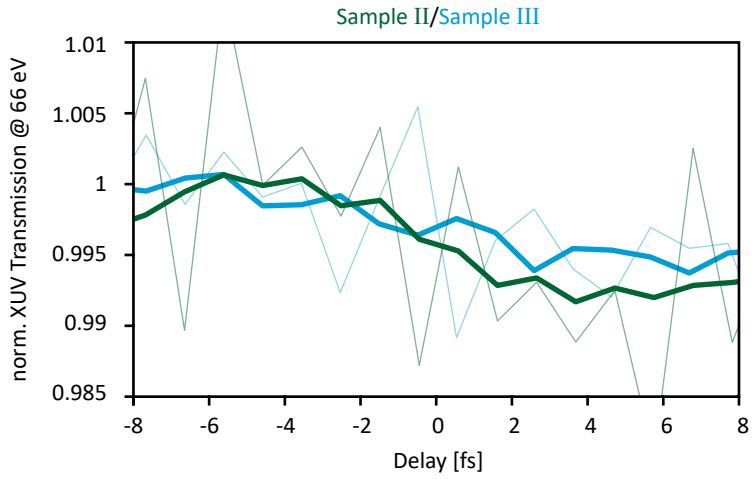

Figure 4.4: Transient absorption measurements for sample II (green) and sample III (blue). The XUV transmission decreases between −3 fs and 3 fs coinciding with the presence of the laser pulse.

atto-MCD contrast was calculated as defined in chapter 3, Eq. (3.3). Although the XUV absorption of the nanoparticles is weak as discussed above, clear signatures of MCD were found. Fig. 4.5 shows the results.
The NiO@Ni spheres and the Ni@Au nanowires show magnetic dichroism. Interestingly, the external magnetic field of around 30 mT is enough to introduce a global magnetic moment in the nanowires.
The Ni@Au spheres with a smaller coverage than sample II did not show a dichroic signal. A few reasons for that are plausible. The spheric geometry might need a larger external field to introduce a magnetic moment. Moreover, the signal might be buried in the noise as the low overall coverage, and therefore a small amount of nickel leads to a bad S/N.

The results are in agreement with earlier studies claiming X-ray MCD of nanoparticles [100, 101]. In those studies, the L-edges of the $3d$-transition metal elements were investigated.
The presented data is static MCD only. The photon flux and the long term stability of the system did not allow to measure the MCD contrast in a pump-probe manner as it was done in the previous chapter.

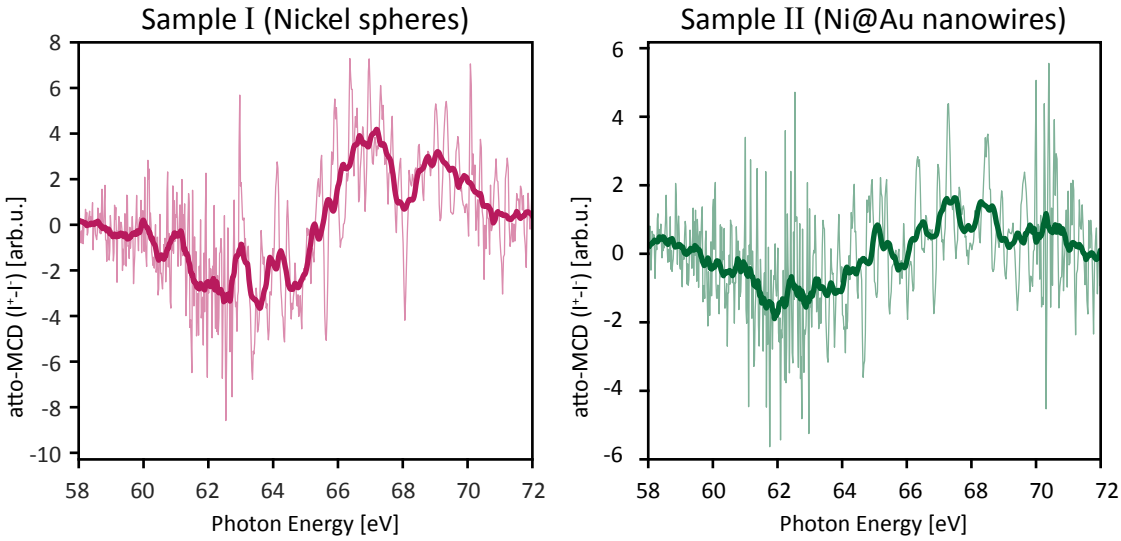

Figure 4.5: Atto-MCD contrast measured for two samples. The raw data for both samples show a clear MCD signature. Applying an adjacent average (thick lines) highlights the dichroic character of the signal. Both spectra were integrated over 5 minutes.

4.3 Main Findings and Outlook

It was shown that a table-top attosecond beamline is capable of performing spectroscopic measurements of nanoparticles. This beamline also offers the possibility to perform time-resolved measurements, not only of excitation dynamics but potentially also of magnetisation dynamics. The first one was already done in this study, whereas the latter has to be subject to future experiments.
The presented results show promising features. Nanoparticles often exhibit fundamentally different properties as bulk materials, however in the work presented here, no major differences could be found. It was possible to measure electronic excitation on a few-femtosecond timescale. The magnitude of the signal was weaker compared to the results of the bulk-like thin film samples.
Moreover, relaxation processes take place on a comparable timescale as they do in bulk. Successful measurement of MCD for two of the three samples was performed. The integration time to get conclusive spectra is long, which makes time-resolved studies, with state-of-the-art kHz laser system, challenging.

The results from this study can be used to design optimised samples for future studies. The influence of the oxidisation, could be analysed performing a control experiment with nickel nanoparticles that are transferred in vacuum conditions from the fabrication to the experiment prohibiting oxidisation.
Improvements can be made by using a layer stack of thinner silicon samples, 50 nm instead of 200 nm, and depositing nanoparticles on both sides. By stacking a few ($\sim 3-4$) of them, the OD can be significantly improved, allowing for shorter integration times.

The low photon flux and the comparably long integration times are problematic. Increasing the repetition rate and the photon flux can eliminate that problem. This could also be solved by using an FEL, however table-top sources, such as the one used in this experiment are superior in terms of availability and flexibility.

Chapter 5

Attosecond Polarisation Sampling in Silicon

The control of nonlinear processes in solids is a hot topic in fundamental research. Nonlinearities are of high interest as they hold the prospect for signal processing at unprecedented frequencies. In 2016 Sommer *et al.*, showed that the electronic structure of dielectrics, such as fused silica, and sapphire can be manipulated on a sub-femtosecond timescale.
Attosecond polarisation sampling (APS) is used to study the fundamental processes during the interaction between a strong electric field and a semiconductor [102]. This measurement technique is capable of mapping the refractive index and the polarisation inside a solid, both of them enabling the reconstruction of the electronic motion in real-time. Moreover, it gives access to the energy that is deposited inside the sample during and after the strong-field excitation. This is a measure for the energy dissipation during the interaction, which is an important quantity, when it comes to real-world applications and towards coherent control and dissipation-free switching.

5.1 Experimental Concept

The concept of APS was first introduced a few years ago by Sommer *et al.* [102]. The idea is to measure the electric field of an intense laser pulse after the interaction with matter. This is enabled by the use of attosecond streaking spectroscopy and its capability of directly measuring the oscillating electric field of light.

In Fig. 5.1, the basic principle of the sequence of measurements is shown. The attosecond streak camera records the vectorpotential $A_L(z,t)$ of the laser pulse. The electric field is obtained by taking the derivative of the vectorpotential. The unperturbed streaking trace with the superimposed vectorpotential is shown as case 1. In case 2 the 200 nm thick silicon sample is inserted under Brewster's angle in the focus. Brewster's angle is chosen to eliminate reflections at the surface of the sample. Due to the high refractive

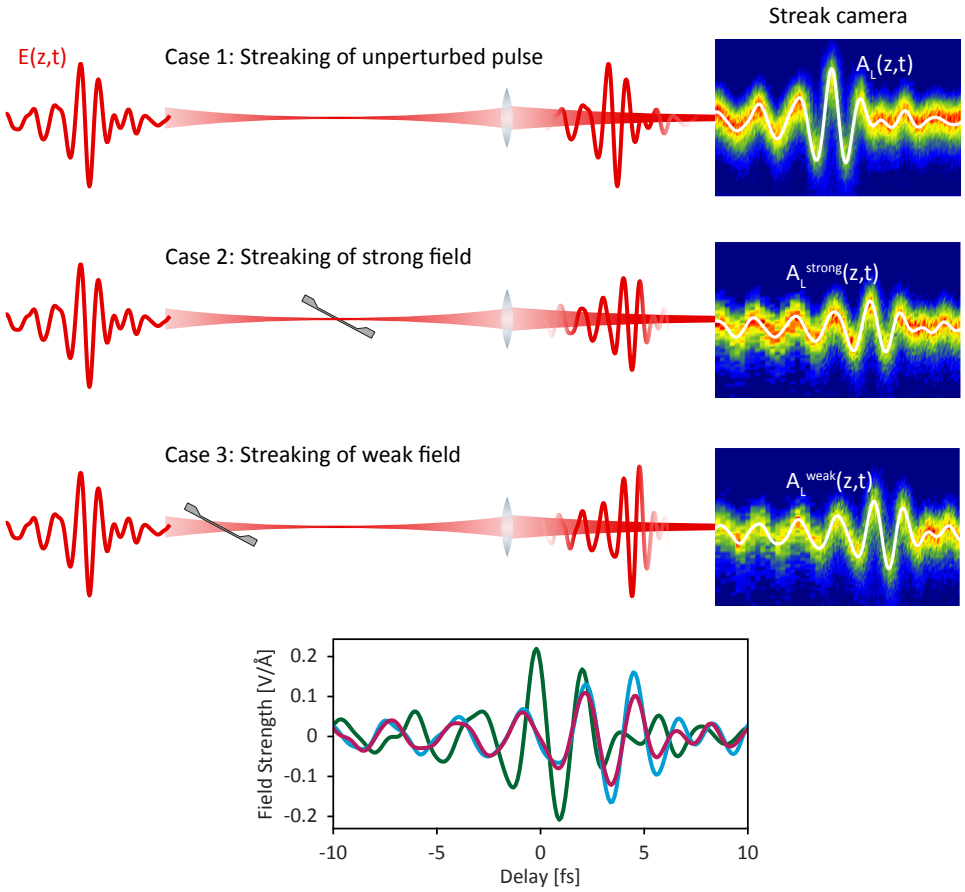

Figure 5.1: APS consists of three individual measurements. In the first measurement (case 1), the unperturbed electric field of the driving laser pulse is recorded. In the two following measurements, the silicon sample is put into the beam, once in the focus (case 2) and once out of focus (case 3). In the lower panel, the three retrieved waveforms are plotted, case 1 (green), case 2 (red) and case 3 (blue).

index of Silicon (3.71@780 nm) the reflection is about 40%. Nevertheless, reflection cannot be completely eliminated as every frequency of the laser pulse has a different Brewster's angle. However, it is minimised such that reflections from now on can be neglected.
The streaking spectrogram and the vectorpotential of the strong field $A_L^{\text{strong}}(z,t)$ after propagation through the silicon sample are illustrated in case 2. The last step in the APS measurement is the recording of the waveform of the weak field, case 3, see $A_L^{\text{weak}}(z,t)$. For this, the sample is moved out of the focus to a position where the intensity is about an order of magnitude smaller.
Taking the derivative of all three vectorpotential yields the waveform of the electric field of the ultrashort laser pulse (see the lower panel). This figure gives a first glimpse of how the nonlinearities act on the electric field. Both waves, which have propagated through the medium (blue and red line), are delayed by a few femtoseconds due to the refractive index $n > 1$. In addition, the strong field exhibits a capping of the most intense half-cycles. This measurement scheme is implemented in the experimental setup of the beamline, which was already introduced in chapter 3.

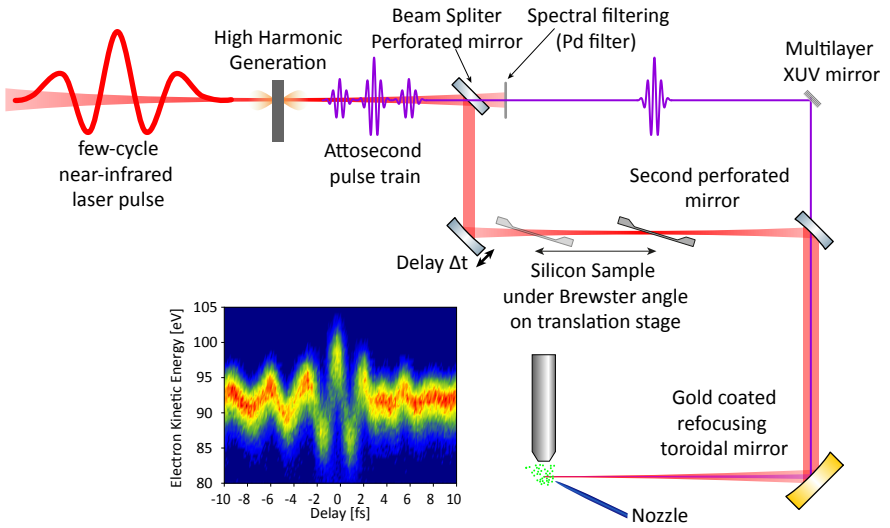

Figure 5.2: The experimental setup of APS. A Mach-Zehnder-type interferometer separates the XUV and the NIR pulse. The XUV is spectrally filtered in order to get isolated attosecond pulses. In the NIR arm, an intermediate focus is generated, where the sample is placed under Brewster's angle to eliminate reflection losses. A perforated mirror recombines both pulses, and a toroidal mirror focuses them into the attosecond streak camera. An exemplary attosecond streaking trace is shown. The false colour plot shows the number of photoelectrons as a function of delay and electron kinetic energy.

A few-cycle NIR laser pulse is focused into a neon-filled ceramics target. According to the three-step model of high-harmonic generation, the strong lase field ionised neon atoms through tunnel ionisation, the freed electrons are then subsequently accelerated

in the dressing laser field, before the electrons recombine with their parent ion under the release of high energetic photon [103]. This leads to the emission of bursts of XUV light. After the generation of the XUV, the two beams are spatially separated and sent into an interferometer. In the one arm, isolated attosecond pulses are generated through spectral filtering, realised by a thin metal foil and a multilayer XUV mirror, which acts as a Bragg reflector. In this setup the highest energetic photons were centred around 115 eV.
In this experiment the other arm of the interferometer is more important. An intermediate focus is generated, in which the silicon sample is placed. Using a translation stage, the sample can be moved along the beam. After the intermediate focus the two beams are recombined and focused into the attosecond streak camera [104]. The attosecond XUV pulse ionises neon atoms, which are sent into the vacuum chamber through a nozzle. The electrons that have the initial kinetic energy E_{kin}, which is equivalent to the difference of the photon energy $\hbar\omega$ and the binding energy E_B. After their release, the electrons experience a shift in energy, due to the external electric field, which is dependent on their birth time with respect to the electric field. A time-of-flight spectrometer (TOF) measures the final kinetic energy and produces an oscilloscope picture of the electric field. As the change of the electron's momentum integrates over the electric field from the time of birth until the pulse has passed, the recorded waveform is proportional to the vectorpotential of the laser pulse, and the derivative has to be taken to get the electric field of the pulse [105].

5.2 Nonlinear Effects

The response of a medium to an external electric field $E(t)$ can be expressed in terms of the polarisation [106]

$$P(t) = \varepsilon_0 \chi^{(1)} E(t), \tag{5.1}$$

with the vacuum permittivity ε_0 and the first order susceptibility $\chi^{(1)}$ of the medium. This is the most basic expression and satisfies conventional, linear optics. Linear in the sense that the polarisation depends linearly on the applied electric field.
When the field strength of the external electric field becomes large, a more general description is needed which also covers the nonlinear response of the system to the external field. The polarisation $P(t)$ can be Taylor expanded and split into a linear and a nonlinear part. The latter one consists of all the higher-order contributions.

$$P(t) = P_L(t) + P_{\mathrm{NL}}(t) \tag{5.2}$$
$$P(t) = \varepsilon_0(\chi^{(1)}E(t) + \chi^{(2)}E^2(t) + \chi^{(3)}E^3(t) + \mathcal{O}(E^4)) \tag{5.3}$$

Here $\chi^{(2)}$ and $\chi^{(3)}$ are the higher-order susceptibilities. They are chosen to be scalar; however, in general, the susceptibility of order n is a tensor of n+1 rank. Processes connected to $\chi^{(2)}$ are called second-order nonlinearities, and $\chi^{(3)}$ processes are named third-order nonlinearities.
Second-order nonlinearities need non-centrosymmetric materials so that the second-rank

tensor does not vanish. Only a few media lack this inversion symmetry and can exhibit second-order nonlinearities, such as second harmonic generation. However, the medium that is studied in this work, silicon is centrosymmetric. Therefore, second-order processes are not further discussed.
One third-order process that shall be discussed is the Kerr effect. The refractive index is dependent on the intensity. However, the influence of this dependence only becomes significant when the intensities of the electromagnetic wave become large. In the previously cited work by Sommer *et al.* the discovered behaviour of the nonlinear response to the applied electric field was mainly attributed to the Kerr effect.

Third Order Effects and the Refractive Index

As introduced above the third-order polarisation is given by:

$$P^{(3)}(t) = \varepsilon_0 \chi^{(3)} E^3(t). \tag{5.4}$$

Using a simplified case where the electric field as a function of time is a monochromatic wave with angular frequency ω, described by:

$$E(t) = E_0 \cos(\omega t) \tag{5.5}$$

and therefore the polarisation can be rewritten as:

$$P^{(3)}(t) = \frac{1}{4}\varepsilon_0 \chi^{(3)} E_0^3 \cos(3\omega t) + \frac{3}{4}\varepsilon_0 \chi^{(3)} E_0^3 \cos(\omega t). \tag{5.6}$$

The first term oscillates at three times the fundamental frequency, it leads to a process called third-harmonic generation, where three photons of the initial frequency are transformed into one photon of frequency 3ω. The second term has the fundamental frequency. This is the process that leads to a modification of the refractive index, the so-called Kerr effect.

Kerr Effect

The intensity dependent refractive index is given by:

$$n(I) = n_0 + n_2 I(t) \tag{5.7}$$

with the Kerr coefficient n_2, which is typically on the order of $10^{-14} - 10^{-15}\mathrm{cm}^2/\mathrm{W}$, it therefore needs large intensities of the incident radiation to become considerable. The derivation of this formula is rather straightforward and will be quickly outlined. Starting from the polarisation in the frequency domain for a centrosymmetric medium and ignoring higher orders:

$$P(\omega) = \varepsilon_0(\chi^{(1)} E(\omega) + \chi^{(3)} E^3(\omega)). \tag{5.8}$$

The part from Eq. (5.6) that oscillates at higher frequencies is also neglected and the polarisation can be rewritten and simplified to

$$\begin{aligned} P(\omega) &= \varepsilon_0(\chi^{(1)}E(\omega) + \frac{3}{4}\chi^{(3)}|E(\omega)|^2E(\omega)) \\ &= \varepsilon_0\chi_{\text{eff}}E(\omega) \end{aligned} \tag{5.9}$$

where the effective susceptibility χ_{eff} is given by:

$$\chi_{\text{eff}} = \chi^{(1)} + \frac{3}{4}\chi^{(3)}|E(\omega)|^2. \tag{5.10}$$

The fundamental relation between the refractive index n and the susceptibility χ, $n^2 = 1 + \chi$ can be applied here and yields the following relation, it is used that $I = |E|^2$.

$$(n_0 + n_2 I)^2 = 1 + \chi^{(1)} + \frac{3}{4}\chi^{(3)}|E(\omega)|^2, \tag{5.11}$$

now neglecting higher orders of n_2 on the left side and using the above mentioned, gives a term for n_2:

$$n_2 = \frac{3}{8}\frac{\chi^{(3)}}{n_0}. \tag{5.12}$$

It shall be noted that throughout literature different prefactors can be found that depend on the convention of the electric field and its intensity envelope.

Two Photon Absorption and Free Carrier Response

Another third order effect that influences the refractive index is two-photon absorption (TPA). The excited carriers in the conduction band change the refractive index, similar to a plasma. The electrons act as quasi-free particles and react to the external electric field.
The imaginary part of the susceptibility tensor is responsible for the two-photon absorption and also determines its strength [107]. The TPA coefficient is given by:

$$\beta = \frac{3\pi}{\varepsilon_0 n^2 c\lambda}\text{Im}(\chi^{(3)}) \tag{5.13}$$

It relates to the number of excited charge carriers by a laser pulse with intensity I, a fluence $\mathcal{F}$ and a carrier frequency ω through TPA as follow [108]:

$$N = \mathcal{F}\frac{\beta I}{2\hbar\omega}. \tag{5.14}$$

The spectrum of the laser pulse via TPA is resonant to the direct band gap, but also resonant to single photon absorption (SPA) over the indirect band gap. Therefore the number of free carriers is not only determined by the TPA coefficient. This will be discussed further in section 5.3.
The free carrier response can be easily understood in terms of the Drude model [109].

The Drude model describes the motion of quasi-free electrons in a metal classically. Excited electrons in silicon are also quasi-free in the potential of the conduction band and the Drude model can be applied to derive the optical properties as a function of the number of excited charge carriers.
The starting point is the equation of motion for a charged particle in an external electric field without damping. The damping is neglected in the Drude model, as the electrons are considered free particles. The equation then reads:

$$m^* \frac{d^2\vec{r}(t)}{dt^2} + m^*\omega_0^2\vec{r}(t) = -e\vec{E}(t), \tag{5.15}$$

where $\vec{r}(t)$ is the electron displacement introduced by the electric field, m^* is the effective mass and e is the unit charge. It can be used that the displacement is proportional to the polarisation $\vec{r}(t) = \frac{-\vec{P}(t)}{Ne}$. Using $\vec{P}(t) = \vec{P}_0 e^{i\omega t}$ and switching to the frequency domain Eq. (5.15) becomes:

$$-\omega\vec{P}(\omega) + \omega_0^2\vec{P}(\omega) = -\varepsilon_0\omega_p^2\vec{E}(\omega). \tag{5.16}$$

ω_p denotes the plasma frequency and is given by $\omega_p = \sqrt{Ne^2/\varepsilon_0 m^*}$. It gives an expression for the polarisation:

$$\vec{P}(\omega) = \frac{\varepsilon_0\omega_p^2}{\omega + i\gamma\omega}\vec{E}(\omega). \tag{5.17}$$

Analogously to the polarisation used in the previous section Eq. (5.4), the complex relative permittivity is directly related to the complex refractive index and is given by: [110]

$$n^2(\omega) = \varepsilon_r(\omega) = -\frac{\omega_p^2}{\omega^2+\gamma^2} + 1 + i\frac{\omega_p^2\gamma}{\omega^3+\gamma^2\omega} \tag{5.18}$$

With the definition of the plasma frequency ω_P, it can be seen from the above Eq. (5.18), how an increase in excited charge carriers leads to an increased ω_P and therefore reduces dielectric function and a reduced refractive index.
The effect of free carriers on the refractive index can also be expressed in a slightly different way using the definition of ω_P:

$$\Delta n_{\mathrm{fc}}(N) = -\frac{e^2}{2\pi n\omega^2}\frac{N}{m^*}, \tag{5.19}$$

where $n_{\mathrm{fc}}(N)$ is the change of refractive index due to the free carriers as a function of the number of the excited electrons, e is the unit charge, n the refractive index corresponding to the frequency ω and m^* the effective mass of the excited electron.

5.3 Time-Integrated Strong-Field Interaction

A time-integrated study gives a first impression of the nonlinear behaviour of silicon. The results presented in the following chapter were acquired together with a master student. Therefore, they are also presented in the master thesis of Malte Schröder [111].

The concept that is used here is based on an open aperture z-scan. The silicon sample is moved along the focus. At the same time, the transmitted pulse energy is recorded. In the fully linear regime, the position of the sample with respect to the focus position does not affect the transmitted energy. This can be expressed in terms of the Beer-Lambert law:

$$I = I_0 e^{-\alpha z} \tag{5.20}$$

where α denotes the frequency and material-dependent absorption coefficient, and z is the propagation length inside the medium. In the case of nonlinear absorption between the incoming light source and the sample, Beer-Lambert's law can be extended by an intensity dependent absorption term:

$$I = I_0 e^{-\alpha z - \beta(I) z} \tag{5.21}$$

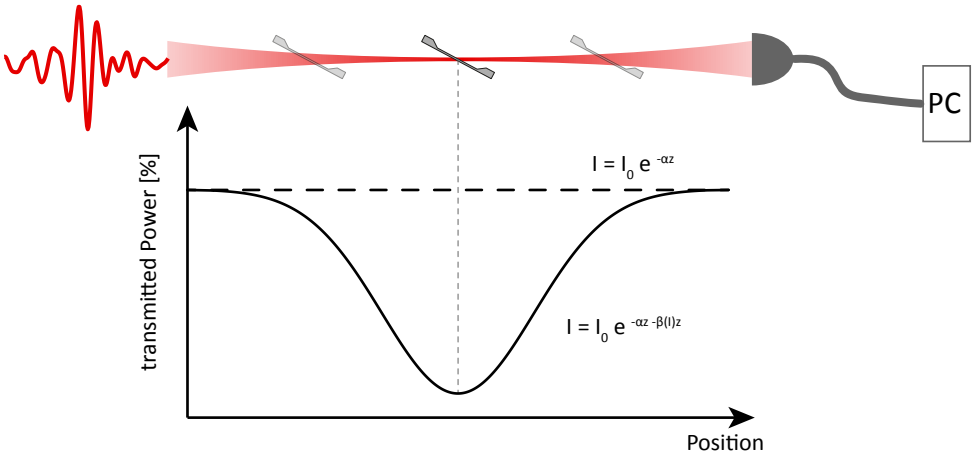

Figure 5.3: An open aperture type z-scan is performed. The transmitted power is measured as a function of the position of the sample. Due to the varying beam size, the intensity changes towards the focus. In the linear absorption case, the absorption is described by Beer-Lambert's law. If the absorption gets nonlinear, an intensity dependent absorption term can be included, leading to an enhanced absorption towards the focus, as indicated by the solid black line.

As stated in the introduction of this chapter, one main question that should be addressed by this study is the role of TPA. Using the formulas, presented in [112], a coefficient for TPA can be calculated and compared with the literature. Moreover, it allows the comparison with the direct excitation through single-photon absorption (SPA).

The attenuation coefficient α of silicon varies largely over the spectral range covered by the laser pulse, it is between $26\,630\,\mathrm{cm}^{-1}$ for 450 nm and $61.6\,\mathrm{cm}^{-1}$ for $1\,\mu$m. It reflects the band-structure quite well, as the photon energy approaches the band gap energy of silicon, the attenuation coefficient rapidly increases. The values for α give a transmission of 58% and 99.8% respectively for the 200 nm thick sample [113]. The experiment yields

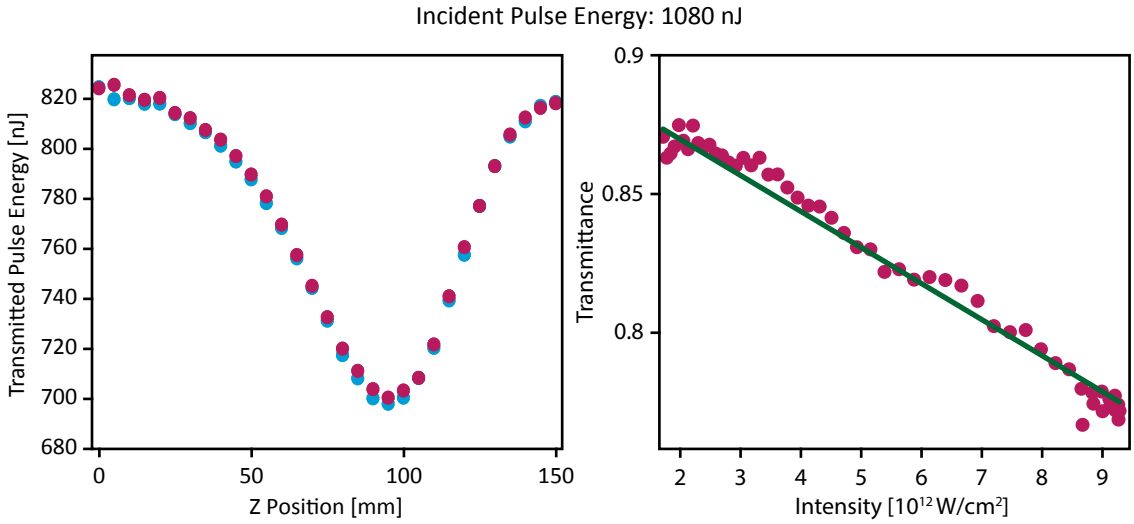

Figure 5.4: Left Panel: Transmitted Energy as a function of sample position, the incident pulse energy is 1080 nJ. Moving towards the focus at around 95 mm increases the absorption, leading to a reduced transmission. The two colours (red and blue) indicate moving the translation stage forward and backwards, ensuring that no irreversible change has been introduced to the sample. Right Panel: Transmittance as a function of intensity. The measured data (red points) agrees very well with a linear fit (green line) indicating TPA. Adapted from [111].

a transmission of 820 nJ out of focus and 700 nJ in focus, which is a relative transmission of 24% and 35% at an incident pulse energy of 1080 nJ, see Fig. 5.4.
For laser pulses weaker than the ones used in this study, a term for the number of excited charge carriers near the surface is given in [108]. In that experiment, reflectivity measurements have been performed, and the change in reflectance was connected to the excitation. Although the laser pulse parameters are not identical, that work is used to give an estimate for the number of excited carriers. It was found that the number of excited carriers can be described by:

$$N = (1-R)\mathcal{F}\left(\frac{\alpha}{\hbar\omega} + \frac{\beta(1-R)\mathcal{F}}{2\hbar\omega\tau_L},\right), \tag{5.22}$$

where R is the reflectivity according to the Fresnel equations under normal incidence, $\mathcal{F}$ is the fluence, α the absorption coefficient and $\hbar\omega$ the central photon energy, while τ_L is the laser pulse duration.
The TPA coefficient β can be determined by the z-scan measurements [112]. It is given by:

$$I(z) = \frac{I_0(1-R)e^{-\alpha z}}{1+\frac{\beta}{\alpha}I_0(1-R)(1-e^{-\alpha z})}. \tag{5.23}$$

For both, Eq. (5.22) and (5.23), it is used that the measurement was carried out under Brewster's angle, making the reflectance $R = 0$, which simplifies the equation signifi-

cantly. The coefficient for TPA can then be expressed as follows:

$$\beta = \alpha \left(I_0 e^{-\alpha z} - I(z) \right). \tag{5.24}$$

This result is quite intuitive. In the absence of reflection and TPA, that means linear absorption in the sample, the difference between the intensity at the exit of the sample $I(z)$ is equivalent to the value given by Beer-Lambert's law. which is the first term in this equation. This makes the difference zero, hence β and the TPA are also zero.
Here it shall be noted that this is a simplified model, in which every difference in absorption is attributed to TPA. This might be true for [108] and [112]; however, for the electric fields used in this study, more effects can influence the absorption, such as tunnelling or multiphoton absorption into higher conduction bands. However, for an estimation of the TPA in this study it is sufficient.
From Eq. (5.24) and a series of z-scan measurements, it is now possible to determine an intensity-dependent TPA coefficient. The results are shown in Fig. 5.5.

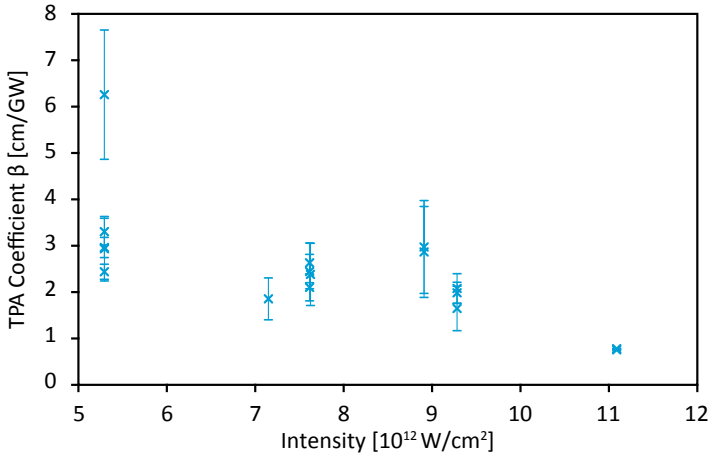

Figure 5.5: The two-photon absorption coefficient β as a function of intensity retrieved from the open aperture z-scan measurements. Over the investigated intensity range β, stays rather constant, with one outlier at low intensity, most likely due to a systematic error in the measurement. The two data points at high intensity also seem to be outliers. However, it is more likely that the two outliers are due to higher-order phenomena, such as multiphoton absorption or tunnelling, which leads a reduced β. The error bars indicate the standard deviation from the average over eleven measurements. Adapted from [111].

The average value for β is 2.5 ± 1.1 cm/GW. The comparison with literature values is challenging, as most studies are carried out in the infrared regime. There, the technological important telecommunication wavelengths are located. The closest value that was found for the TPA coefficient β was 2.0 ± 0.5 cm/GW at 850 nm [114]. In another study conducted by Lin *et al.* [115], a fund a value for $\beta < 1$cm/GW, however, in the infrared above 1 μm. Although the pulse parameters are fairly different in the experiment of Bristow *et al.*, the two results agree surprisingly well. As this result does overlap so well

with values from literature it is justifiable to carry on with the evaluation along this path.
Therefore, it is useful to go back to Eq. (5.22). This equation can be split into two parts. The first part describes the linear absorption, which leads to SPA. And a second term that describes the nonlinear absorption, in this case, TPA.

$$N_{\mathrm{SPA}} = \mathcal{F}\frac{\alpha}{\hbar\omega} \tag{5.25}$$

$$N_{\mathrm{TPA}} = \mathcal{F}\frac{\beta I}{2\hbar\omega} \tag{5.26}$$

where $I = \mathcal{F}/\tau_L$ is the intensity. The interpretation of these two formulas is again rather intuitive. The linear absorption attributed to α is scaled by the fluence F and divided by the photon energy of a single photon resulting in the number of excited carriers. The same is done for β, first the fluence connected to β is determined, scaled by the intensity and divided by the energy of two photons.

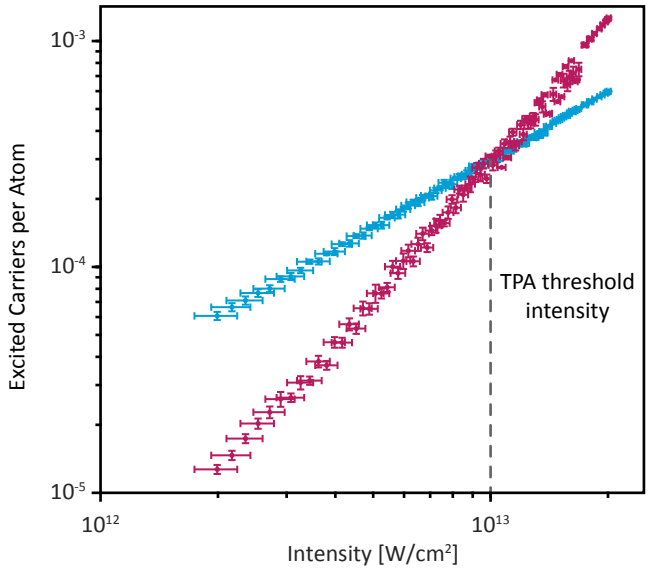

Figure 5.6: The number of excited carriers per atom is plotted as a function of intensity. At the threshold intensity (grey dashed line) two-photon absorption (red) becomes the dominating process over single-photon absorption (blue). The error bars indicate the standard deviation for the intensity as well as for the number of excited carriers from the average of eleven measurements. Adapted from [111].

Plotting the results for excited carriers as a function of intensity shows an interesting feature, see Fig. 5.6. For intensities below 10^{13} W/cm^2 excited electrons are mainly due to SPA and direct excitation across the indirect band gap. At 10^{13} W/cm^2 both processes, SPA and TPA contribute equally to excited charge carriers in the conduction band. After this point, TPA dominates. This point marks the threshold intensity, where

nonlinear processes dominate the response of the medium to the strong electric field.
It is interesting to look not only at the fraction of excited charge carriers per atom, which reaches 1‰, but also to look at the total doping concentration. Considering an atomic density of 5×10^{22} $^{\text{atoms}}/_{\text{cm}^{-3}}$ it corresponds to a doping concentration of up to 10^{19} $^{1}/_{\text{cm}^{-3}}$. This doping concentration achieved by light-matter interaction is at least one order of magnitude than what is possible using conventional doping for semiconductors [116].
Section 5.2 shows that a large number of excited charge carriers in a medium lead to a change of the refractive index. In simple words, a medium with many excited electrons becomes like a plasma. Therefore, the real part of the refractive index gets smaller. Applying Eq. (5.19), introduced before, an intensity-dependent change of the real part of the refractive index can be derived, as plotted in Fig. 5.7. The refractive index gets reduced by the value on the y-axis in Fig. 5.7.

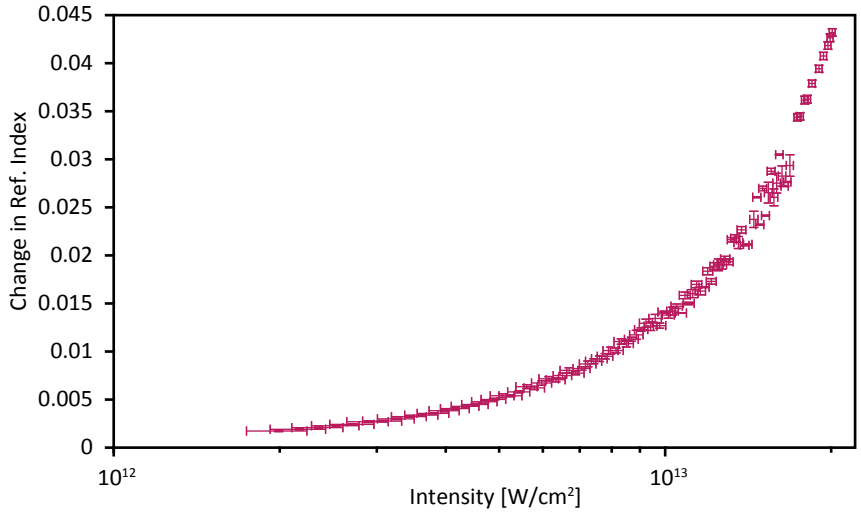

Figure 5.7: The excited free carriers in silicon lead to a negative contribution to the refractive index, which scales linearly with the intensity (semi-logarithmic plot). At an intensity inside the sample slightly above $10^{13}\,\frac{\text{W}}{\text{cm}^2}$ the change is on the order of 1% of the refractive index (3.71 @ 780 nm). The atomic density was chosen as $5 \cdot 10^{22}\text{atoms/cm}^3$. The error bars indicate the standard deviation from the average over eleven measurements. Adapted from [111].

At intensities inside the sample above $I = 10^{12}\text{W/cm}^2$ the change of refractive index Δn becomes on the order of 1%. It should be noted that the effective mass is taken into this calculation and the effective mass during the strong-field interaction can vary considerably from the equilibrium values [117]. The field strengths used here are on the lower end of the region, where these effects play a role. Therefore they are neglected, and the literature values are used.
Interestingly this negative contribution is countered by a positive contribution from the Kerr effect. The nonlinear refractive index n_2 is given in the literature as $n_2 =$

$4.6 \times 10^{-14}\text{cm}^2/W$ by Bristow *et al.* [114]. The dispersion of n_2 is supposed to be flat, as this value is for 850 nm. For an intensity of $1 \times 10^{13} W/cm^2$ the contribution due to the Kerr effect is about $\Delta n = 0.46$. This number seems too high, as it would change the refractive index by more than 10%. However, it illustrates that the free carrier contribution is countered by another nonlinear effect.

5.4 Time-Resolved Strong-Field Interaction

During the interaction of a strong laser field and a solid, many nonlinear effects can be driven, e.g. multi-photon absorption, Kerr effect and tunnelling between the valence band and the conduction band, to name a few. These nonlinearities are highly interesting, as mentioned at the beginning of this chapter.

5.4.1 Theoretical Description

The nonlinear polarisation describes the response of the system to a strong electric field and can therefore, give information about the occurring processes. The same is true for the refractive index, which will be investigated too.

Nonlinear Polarisation

The propagation of a light pulse is given by:

$$\frac{\partial^2}{\partial z^2} E(z,t) - \frac{1}{c^2}\frac{\partial^2}{\partial t^2} E(z,t) = \frac{1}{\varepsilon_0 c^2}\frac{\partial^2}{\partial t^2} P(z,t) \tag{5.27}$$

switching to the frequency domain and using:

$$E(z,t) = \int E_\omega(z) e^{-i\omega t} d\omega \tag{5.28}$$

$$P(z,t) = \int P_\omega(z) e^{-i\omega t} d\omega \tag{5.29}$$

allows to rewrite Eq. (5.27) in the following way:

$$\frac{\partial^2}{\partial z^2} E_\omega(z) - \frac{\omega^2}{c^2} E_\omega(z) = -\frac{\omega^2}{\varepsilon_0 c^2} P_\omega(z) \tag{5.30}$$

In the case of a weak pulse the polarisation has only a linear contribution and is given in terms of the linear susceptibility χ_ω.

$$P_\omega = \varepsilon_0 \chi_\omega E_\omega(z) \tag{5.31}$$

This allows Eq. (5.27) to be restated in the following way:

$$\frac{\partial^2}{\partial z^2} E_\omega(z) = -\frac{\omega^2}{c^2}(1+\chi_\omega) E_\omega(z) = -\frac{\omega^2}{c^2} n_\omega^2 P_\omega(z) \tag{5.32}$$

with the refractive index $n_\omega^2 = 1 + \chi_\omega$. A general solution for Eq. (5.30) is:

$$E_\omega(z) = F_\omega e^{ik_\omega z} + G_\omega e^{-ik_\omega z} \tag{5.33}$$

where k denotes the wavevector and is given by $k_\omega = \omega n_\omega / c$, F_ω and G_ω are the spectral amplitudes of the forward and backward propagating wave. The part of the solution propagating in the backward direction is ignored here, as only the transmitted fraction of the pulse is of interest. In the experiment, mounting the sample under Brewster's angle eliminates the backwards propagating part.
The transmitted field in the linear regime allows the complex refractive index to be determined. The field at the entrance of the medium is given by:

$$E^{\text{weak}}(0,t) = \int d\omega F_\omega e^{-i\omega t} \tag{5.34}$$

and after propagation through the thin sample of thickness L by:

$$E^{\text{weak}}(L,t) = \int d\omega F_\omega e^{-i\omega t} e^{ik_\omega L} \tag{5.35}$$

From the comparison of the two equations it becomes clear that $\tilde{n}_\omega$ can be retrieved:

$$e^{ik_\omega L} = \frac{\int E^{weak} e^{i\omega t} dt}{\int E^{weak} e^{i\omega t} dt} \tag{5.36}$$

The above described case is valid in the presence of a weak pulse. The comparison of the unperturbed electric field with the transmitted electric field gives direct access to the dielectric function of the medium.
In the next step, the electric field strength shall be high enough to cause nonlinear effects inside the medium. When nonlinearities become substantial, Eq. (5.30) no longer holds and a nonlinear polarisation contribution has to be considered. Therefore the polarisation becomes:

$$P(z,t) = \varepsilon_0 \int \chi(t-t') E(z,t') + P^{NL}. \tag{5.37}$$

Putting that into Eq. (5.27) gives in analogy to Eq. (5.30):

$$\frac{\partial^2}{\partial z^2} E_\omega(z) = -\frac{\omega^2}{c^2} n_\omega^2 P_\omega(z) - \frac{\omega^2}{\varepsilon_0 c^2} P_\omega^{NL}(z) \tag{5.38}$$

Again using the Ansatz from before, $E_\omega(z) = F_\omega(z) e^{ik_\omega z}$, here $F_\omega(z)$ exhibits a z-dependence due to the spatial dependence of the nonlinearity.
With the assumption that the spatial dependence is small, $\partial^2/\partial z^2 E_\omega(z)$ can be approximated as follows:

$$\begin{aligned} \frac{\partial^2}{\partial z^2} E_\omega(z) &= \frac{\partial^2 F_\omega(z)}{\partial z^2} e^{ik_\omega z} + 2ik_\omega \frac{\partial F_\omega(z)}{\partial z} e^{ik_\omega z} - k_\omega^2 F_\omega(z) e^{ik_\omega z} \\ &\approx 2ik_\omega \frac{\partial F_\omega(z)}{\partial z} e^{ik_\omega z} - k_\omega^2 F_\omega(z) e^{ik_\omega z} \end{aligned} \tag{5.39}$$

This leads to a simpler term for the nonlinear polarisation:

$$2ik_\omega \frac{\partial F_\omega(z)}{\partial z} = -\frac{\omega^2}{\varepsilon_0 c^2} P_\omega^N L(z) e^{-ik_\omega z}. \tag{5.40}$$

In the same way as in Eq. (5.34) and (5.35), the same thing is done here for the strong field case and the measured unperturbed field is given by:

$$E^{\text{strong}}(0,t) = \int d\omega F_\omega(0) e^{-i\omega t} \tag{5.41}$$

and the strong electric field after the interaction with the sample can be expressed as:

$$E^{\text{strong}}(L,t) = \int d\omega F_\omega(L) e^{-i\omega t} e^{ik_\omega L}, \tag{5.42}$$

again note that $F_\omega(z)$ exhibit a z-dependence due to the nonlinearity.
To find an expression that links the nonlinear polarisation P^{NL} with the measured fields $E^{\text{strong}}(0,t)$ and $E^{\text{strong}}(L,t)$, a representation of Eq. 5.41 and 5.42 is needed that can be put into Eq. 5.40. Therefore using the inverse:

$$F_\omega(0) = \frac{1}{2\pi} \int dt e^{i\omega t} E^{strong}(0,t) \tag{5.43}$$

$$F_\omega(L) = \frac{1}{2\pi} \int dt e^{-k_\omega L} e^{i\omega t} E^{strong}(L,t) \tag{5.44}$$

$$\tag{5.45}$$

and again ignoring the second derivative, as it is small, a term for the nonlinear polarisation can be formulated:

$$P_\omega^{NL} \approx -2ik_\omega \frac{\varepsilon_0 c^2}{\omega^2} \frac{F_\omega(L) - F_\omega(0)}{L} e^{ik_\omega z} \tag{5.46}$$

Using that the weak pulse is simply an attenuated replica of the incident pulse:

$$F_\omega(0) = \frac{1}{\beta} F_\omega \tag{5.47}$$

leads to final term for the nonlinear polarisation as function of the transmitted strong and weak electric field [102]:

$$P_\omega^{NL} \approx -2ik_\omega \frac{\varepsilon_0 c^2}{\omega^2} \frac{E_\omega^{\text{strong}}(L) - E_\omega^{\text{weak}}(L)/\beta}{L} e^{ik_\omega (z-L)}. \tag{5.48}$$

The determination of the nonlinear polarisation and the direct measurement of the waveform of the electric field allow the calculation of the work that was done to the sample. The transferred energy can be easily calculated as it is the integral over the electric field multiplied by the current flown into the sample. Here the current is given by the time derivative of the polarisation:

$$W(t') = \int_0^t E(t') \frac{\mathrm{d}P(t')}{\mathrm{d}t'} \mathrm{d}t' \tag{5.49}$$

Refractive Index During Strong Field Interaction

The measurement of the exact waveform before and after the propagation through a medium allows the complete reconstruction of the frequency dependent complex refractive index:

$$\tilde{n}(\omega) = n(\omega) + i\kappa(\omega). \tag{5.50}$$

In Fig. 2.3 it is shown how the real and imaginary part of the refractive index act out on the waveform. The attosecond streak camera allows the recording of the oscillating electric field of the short laser pulse. This enables the reconstruction of the amplitude and phase.
The real part $n(\omega)$ of the refractive index leads to a phase shift, whereas the imaginary part $\kappa(\omega)$ results in a modulation of the amplitude, as can be seen in the following:

$$\tilde{E}_{\omega,out} = \tilde{E}_{\omega,in}\ e^{ikz}, \text{with } k = \frac{\omega\tilde{n}(\omega)}{c_0}. \tag{5.51}$$

This can be rewritten into:

$$\tilde{E}_{\omega,out} = \tilde{E}_{\omega,in}\ e^{\frac{i\omega n(\omega)z}{c_0}} e^{\frac{-\omega\kappa(\omega)z}{c_0}}. \tag{5.52}$$

By disentangling the real and the imaginary part, it is possible to write each as a function of the incident E_{in} and transmitted waveform E_{out}:

$$\begin{aligned} n(\omega) =& i\frac{\log(\Re(\frac{E^{\omega}_{out}}{E^{\omega}_{in}}))c_0}{\omega z} \\ \kappa(\omega) =& i\frac{\log(-\Im(\frac{E^{\omega}_{out}}{E^{\omega}_{in}}))c_0}{\omega z} \end{aligned} \tag{5.53}$$

where ω is the frequency, z the propagation distance, c the speed of light.
These expressions allow in principle for a Gabor-transform a time-frequency analysis, basically a windowed Fourier transformation. This gives insight into which frequencies come at which time, and when they are preferably absorbed or in the case of new generated frequencies, when they are created.

5.4.2 Results of the Time-Resolved Study

The experimental details were described in section 5.1. One APS measurement consists of four individual scans to record four waveforms. The first scan records the unperturbed waveform, followed by the measurement of the strong and the weak field, after propagation through the sample. Finally, the unperturbed waveform is recorded once more. The last measurement is done to assure the absence of timing jitter and phase drifts within one set of APS measurements. Only so-called "quartets", where no significant drift was apparent, were used for further evaluation. From now on, the waveforms are referred to

as unperturbed, strong and weak.
The first striking result is shown in Fig. 5.1 and plotted in more detail in Fig. 5.8. The figure compares the two transmitted waveforms of the strong and the weak pulse. There is an excellent agreement between the waveforms in the weak part of the pulse, between −15 fs and −3 fs and again between 5 fs and 15 fs. However, where the electric field of the pulse is strong, a strong truncation of the waveform is evident.

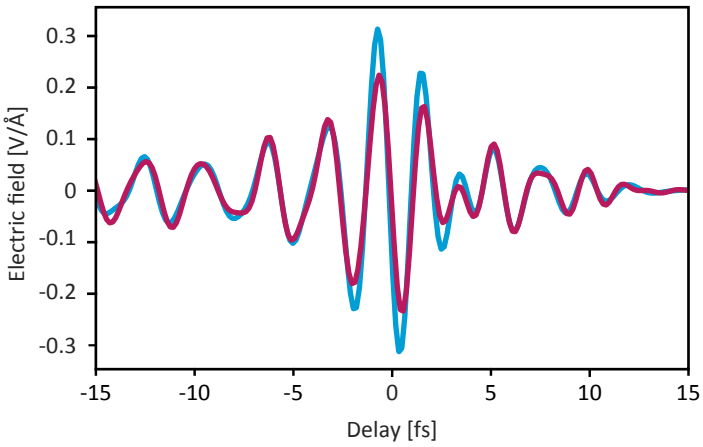

Figure 5.8: Two waveforms recorded by attosecond streaking. The waveform that was transmitted through the sample at high intensity (red) exhibits a distinct attenuation of the strong half-cycles of the electric field. Before and after the intense part of the pulse, the waveform overlaps well with the weak pulse (blue). This truncation can be attributed to nonlinear processes, such as TPA, which only happens when the electric field is strong.

It has to be noted that the Gouy phase does not play a role here. Although the waveforms when interacting in focus and out of focus have a different CEP, due to the Gouy phase, the attosecond streak camera images the waveform of the intermediate focus in Fig. 5.2. In this intermediate focus, the Gouy phase is the same (close to zero) for both waveforms and therefore does not play a role in the following discussion.

Linear vs. Nonlinear Regime

Fig. 5.8 already illustrates that the interaction between the medium and the electric field can be nonlinear. This also means that pulse with the weak electric field can already exhibit modifications of the waveform that are not only owed to linear dispersion. Numerical propagation of the unperturbed waveform trough the medium can give an answer to the question, whether there the weak field experiences nonlinearities. Literature values for silicon are used to do this numerical propagation, taken from [118]. In addition, Sommer *et al.* found, that numerical propagation to the midpoint of the sample is ideal for the comparison of the waveforms. The nonlinearities in the medium

lead to an accumulated error between the the numerical propagation direction, that cannot be compensated numerically. Therefore the midpoint was found to exhibit the least errors [102]. Fig. 5.9 compares the numerically forward propagated waveform with the

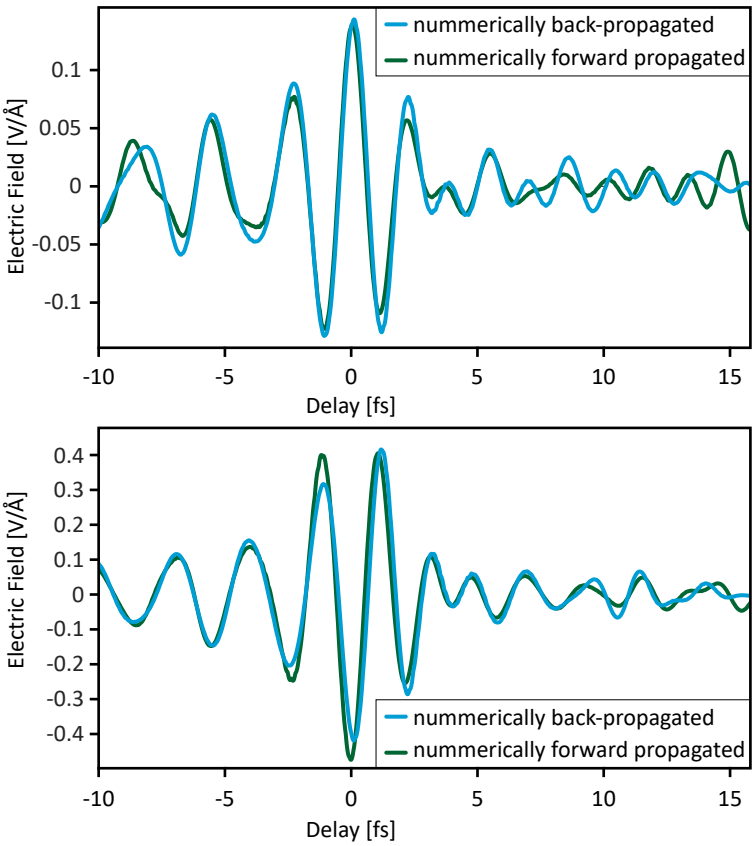

Figure 5.9: The comparison between the backpropagated weak field (blue) and the forward propagated unperturbed field (green) for two different intensities, low intensity upper panel, high intensity lower panel. If the field strengths are weak, the forward propagated and the backpropagated field (upper panel) overlap quite well, especially in the intense half-cycles. For the higher intensities (lower panel), the most intense half-cycles start to differ from each other. This is caused by nonlinear effects, as the propagation only accounts for linear dispersion. In the lower panel the oscillations before and after the pulse overlap excellent.

transmitted waveform that was numerically backpropagated. The two panels represent different intensities of the incident wave of $5 \times 10^{11}\mathrm{W/cm^2}$ and $6 \times 10^{11}\mathrm{W/cm^2}$ in the focus, for the weak field that is studied here, the intensity is an order of magnitude less. There are two points that have to be considered here when comparing the two waveforms. First, the overall agreement, which is a measure for the stability and sensitivity of the measurement, and secondly, the agreement in the intense half-cycles, which gives

information about the nonlinearities that might already occur at low intensities.
The overall agreement in the lower panel is better than in the upper panel. The attosecond streaking camera is more sensitive for larger electric field amplitudes therefore the S/N is better. The superior S/N ratio is visible, especially in the weak oscillations before and after the pulse. The agreement in the strongest half-cycles, however, is better in the upper panel. The backpropagated waveform actually overestimates the field strength at the midpoint. In the lower panel, the onset of nonlinear behaviour is evident. Two of the three most intense half-cycles already suffer from nonlinear absorption and are capped. This shows that for weak enough intensities ($< 5 \times 10^{12}\mathrm{W/cm^2}$ in the focus) the assumption holds that moving the sample is enough to probe the linear response of silicon.
From now on the terms *forward propagated* and *backward propagated* refer to the numerically propagated fields to the midpoint of the silicon sample. In particular, *forward* is the initially unperturbed field that is propagated into the sample using literature values for the refractive index, and *backward* describes the weak and strong fields that are both numerically propagated into the sample, only using linear considering linear dispersion. The terms do not state anything about the propagation direction of the electromagnetic field.

Beahviour of the Nonlinear Polarisation

The nonlinear polarisation quantifies the response of the system to a strong external perturbation. Eq. 5.48 gives an expression for the nonlinear polarisation P_{NL} depending on the transmitted weak E^{weak} and strong electric field E^{strong}. It also allows the calculation of the deposited energy in the medium as a function of time during the strong-field interaction, as described by Eq. 5.49.

Fig. 5.10 illustrates the nonlinear polarisation P_{NL} and its phase relation to the driving electric field. In the case of silicon, the nonlinear response P_{NL} is more or less zero up to the point where the electric field is strong and where nonlinear processes start. The small oscillations before and after the main pulse can be attributed to noise in the measurement. P_{NL} starts to evolve, when the electric field becomes larger than $0.05\,\mathrm{V/Å}$. It exhibits a phase-shift with respect to the driving field. This phase shift stays until the pulse is over and is on the order of $\pi/2$. This indicates a flow of energy into the sample, as the phase-shift does not change the sign, it also means that the flow is only unidirectional and that the energy remains inside the sample within the duration of the pulse.
As the experiment was carried out at multiple field strengths, the nonlinear polarisation response can be investigated as a function of electric field strength. Fig. 5.11 illustrates the four cases of the P_{NL} with increasing field strengths.

The nonlinear polarisation varies between $0.01\,\mathrm{C/m^2}$ and $0.14\,\mathrm{C/m^2}$. Following the Taylor expansion, which was introduced in the theoretical part, the effect of increased field strength on P_{NL} can be estimated. The field strength for the shown nonlinear polarisation changes by a factor of 3.7, whereas the P_{NL} changes by a factor of 14 only. This is

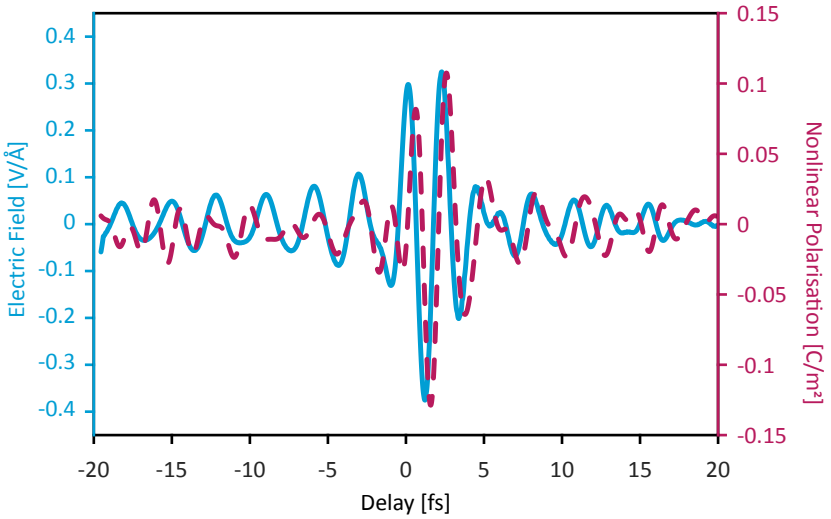

Figure 5.10: The backwards propagated weak field (blue line) and the corresponding nonlinear polarisation P_{NL} (dashed red) at an intensity of $I_0 = 4.2 \cdot 10^{12}$ W/cm^2. The nonlinear polarisation is phase shifted to later times with respect to the driving electric field. This indicates a large number of excited and therefore quasi-free electrons, which follow the electric field, similar to the control experiment in gas in the framework of Sommer *et al.* [102].

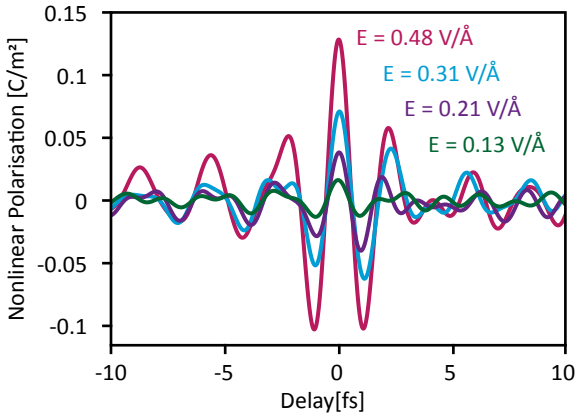

Figure 5.11: The nonlinear polarisation as a function of intensity. The measurements were performed at four different field strengths as plotted. The nonlinear polarisation increases towards higher field strengths, however it seems not to scale with the electric field to power of three.

in contradiction to the expected third-order process. If P_{NL} was caused by a third-order process, it should increase by $3.7^3 \sim 50$. This indicates a superimposed second-order process, and will be discussed later-on.

Energy Dissipation

The direct measurement of the electric field and the polarisation equips this technique to determine the amount of energy that has gone into or out of the system at every time, according to Eq. (5.49). The upper panel in Fig. 5.12 shows the deposited energy $W(t)$ as a function of time, for four different intensities of the driving laser field. With increasing field strength, the external wave moves and excites more and more electrons out of their equilibrium position. The irreversible transferred energy, the energy that is in the sample after the oscillations caused by the electric field are gone, scales linearly with the intensity.

In the lower panel the contributions from linear and nonlinear polarisation are deconvolved. The linear polarisation leads to a virtual excitation modified by double the laser frequency that is gone after the pulse. The irreversible transfer can be fully attributed to the nonlinear polarisation. The transfer has small oscillation itself, during the presence of the laser field, towards the end of the pulse at $\sim 3\,\mathrm{fs}$ (dark blue line).
The relation between the contributions from linear and nonlinear polarisation also indicate that whenever the field is strong, the slope of the irreversibly deposited energy is maximised. The lifetime of the excited carriers outlasts the interaction period.
The results look very similar to the results from earlier studies in dielectrics, indicating a somehow universal behaviour for small and wide band gap materials.

Comparison with TD-DFT Calculations

The experimental results were backed up by full *ab-inito* TD-DFT calculations by collaborators in the group of Prof. Kazuhiro Yabana from the University of Tsukuba (Japan) using the open-source code SALMON, which was developed in that group. For computational details see appendix.
In contrast to most TD-DFT calculations and theoretical models, their code is equipped with the possibility to use measured laser pulses as input into their calculations. This allows a direct comparison of the calculated and the experimental results. Moreover, they were successful in making it possible to propagate the laser pulse into the sample under oblique incident, i.e. in this case, Brewster's angle. This is relatively simple to realise in an experiment, but bears a challenge. For the calculations, again see appendix for details.

These measured pulses were then propagated in the same manner as in the experiment, once at high intensity and once at low intensity. In the low intensity case, the pulse is linearly propagated through the sample using the calculated dielectric function from TD-DFT calculations. A numerical linear, backwards propagation into the sample was

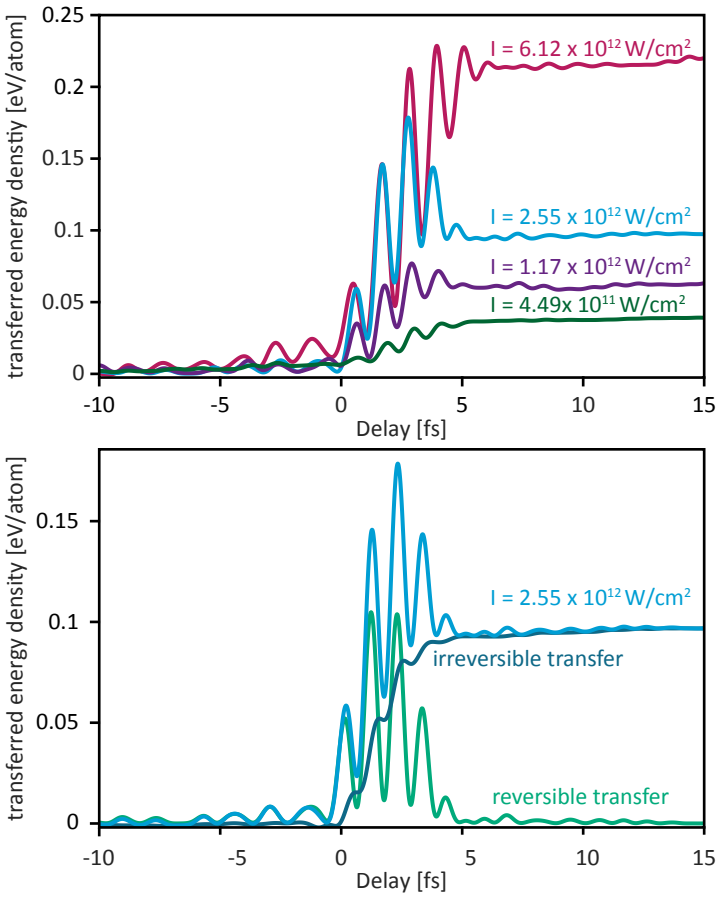

Figure 5.12: The transferred energy calculated from the integral over the electric field multiplied by the temporal derivative of the polarisation, which is the current. This can be done for different intensities (upper panel). Moreover, it allows the deconvolution of the work into a linear (green line) and a nonlinear (dark blue line) contribution, which can also be seen as virtual and permanent excitation. The lower panel deconvolves the blue curve from the upper panel ($I = 5 \cdot 10^{12}$ W/cm^2).

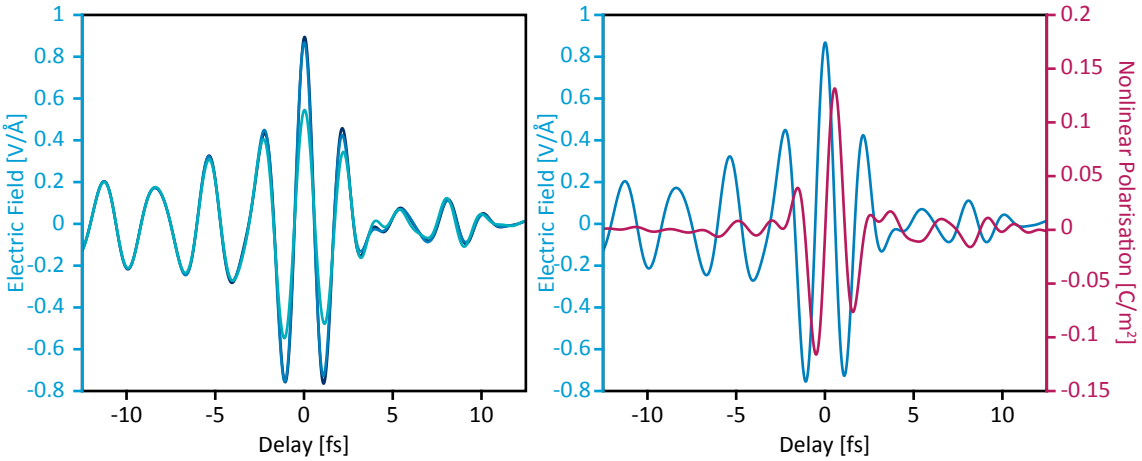

Figure 5.13: The blue curves in the left panel show the results of the TD-DFT calculations. It shows the pulse that was used as input for the calculations (dark blue), the linear propagated pulse (blue) and the strong field pulse, including nonlinear effects (light blue). The calculations reflect the experimentally observed effects excellently. The right panel shows nonlinear polarisation (red) and the driving laser pulse at the midpoingt of the sample. The nonlinear polarisation follows the driving electric field with a constant phase shift of $\pi/2$.

then applied in the same way as it was done to the experimental results. The unperturbed pulse was linearly forward propagated. The results are shown in Fig. 5.13.
The agreement with the experimental result is not only excellent in quality but also agrees quantitatively very well. It shows the truncation of the most intense half-cycles. Additionally, before and after the main part of the pulse, the oscillations align in all three cases, indicating the nonlinear nature of the effect. In the case of low intensity a slight discrepancy between the forward and backwards propagated waveform is appearing, which can be attributed to a residual reflection in the case of the TD-DFT calculations.
The retrieved nonlinear polarisation shows a delay of a quarter-wave, as seen before in the experimental data. This phase shift is constant over the whole range of the pulse.
This excellent agreement between experimental and calculated data, allows to draw further conclusion. Fig. 5.14 shows how the nonlinear polarisation, that can be derived from the calculated data, scales with the exponent of the electric field. It clearly illustrates a trend away from a third-order process towards a second-order process.

The exponent of the electric field with which the nonlinear polarisation scales as a function of intensity is plotted. In this depiction, it becomes evident that the scaling of P_{NL} follows more a second-order than a third-order process. Due to the lack of inversion symmetry in silicon, second-order processes cannot happen. However, the behaviour observed here shows a clear trend at higher field intensities towards a process that scales

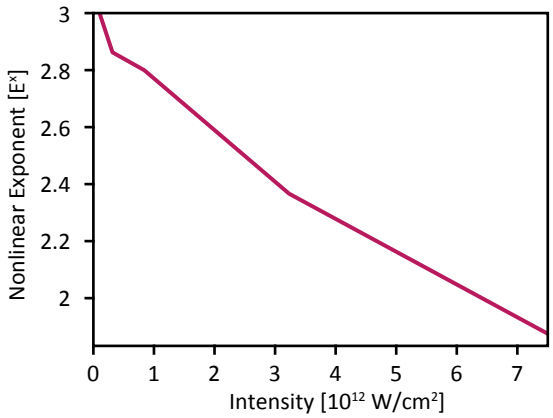

Figure 5.14: The figure shows the exponent of the electric field as a function of the nonlinear polarisation $P_{\mathrm{NL}} \propto E^x$. It shows how the dependence on the exponent changes from three to two, marking a change from a third-order to a second-order process. This can be attributed to the change from TPA to tunnelling [37].

with the electric field squared. This indicates a transition from a multiphoton process, such as TPA, to the tunnelling regime, where electrons tunnel from the valence band into the conduction band with some probability to go into higher conduction bands. This transition is described by the so-called Keldysh parameter γ [119]. For $\gamma > 1$ multiphoton absorption dominates, for values smaller than 1 tunnelling becomes the favourable process.
Additionally the deposited work inside the sample can be compared.

The deposited energy inside the sample per volume can be calculated analogously to the experimental data. The data again agrees with the experimentally obtained one. Especially the agreement with the dissipated or irreversible deposited energy is impressive.
Based on these results further statements can be made, e.g. about electronic motion upon excitation in real space, which can be derived from the calculation [120].

Refractive Index Reconstruction

In addition to the evaluation of the nonlinear response of the system, as done above and theoretically discussed in section 5.4.1, the second approach as introduced in section 5.4.1, shall be briefly presented here.
Using the Fourier transformed signal of the waveforms and comparing weak and strong fields with the incident electric field, frequency-resolved values for the refractive index can be retrieved. Note that here no forward or backward propagation is done, as this would remove the contribution from linear dispersion.
In Fig. 5.16, the results of this Fourier transformation and the refractive index retrieval are shown. The spectrum of the strong pulse shows clearly less amplitude over the whole

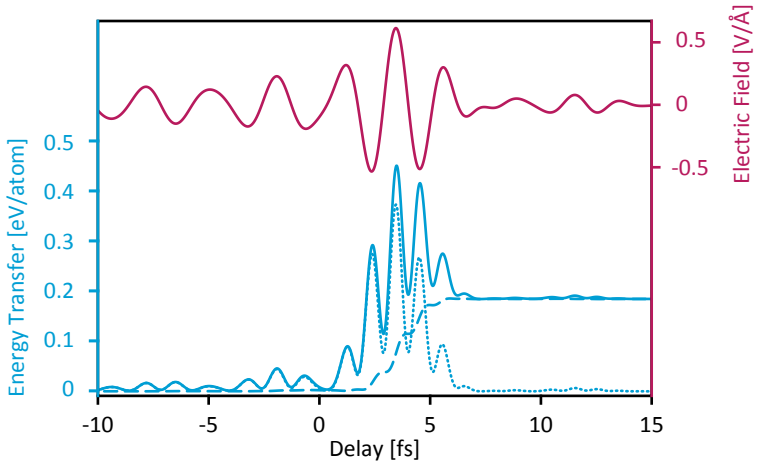

Figure 5.15: The total energy that has been transferred in the sample (solid blue line), deconvolved into linear (dotted) and nonlinear (dashed) or transient and lasting contributions. Whenever the electric field (red line) is strong, the nonlinear contribution has maximum slope. The agreement with the experimental data (Fig. 5.12) is excellent.

spectral range than the weak and unperturbed pulse. This also reflects in the lower right panel, where the extinction coefficient κ is plotted.
The retrieved spectral phase is not plotted here, as it is not comprehensive. The real part of the refractive index n is shown in the lower left panel. It agrees quite well with the literature values and does not differ much between strong and weak fields either. Although, at higher frequencies, this analysis does see a slightly higher refractive index for the strong field case.
A point that has to be taken into account here is that even if the refractive index changed by 0.1, which corresponds to about 3%, attosecond streaking would probably not see it if the sample was only 200 nm thick. This thickness does not suffice to introduce a large enough phase-shift that can be resolved by attosecond streaking.
This technique, however, suffers from the poor spectral resolution. The gathered information could also be retrieved from, e.g. a white-light interferometer. In principle, the idea was to use a time-frequency analysis (Gabor-transform) to see which frequencies are favourably absorbed and at which times, maybe even the generation of new frequencies could be observed. Limitations of this technique are the long measurement time on the one hand, and, on the other hand, the poor sensitivity of attosecond streaking, which limits the spectral resolution. Advances in the measurement of electric fields might be able to resolve this better and allow time-frequency analysis to be performed.

5.5 Main Findings and Outlook

The findings presented in this chapter clearly prove that Attosecond Polarisation Sampling does not only work in a dielectric as demonstrated a few years ago, but is also a

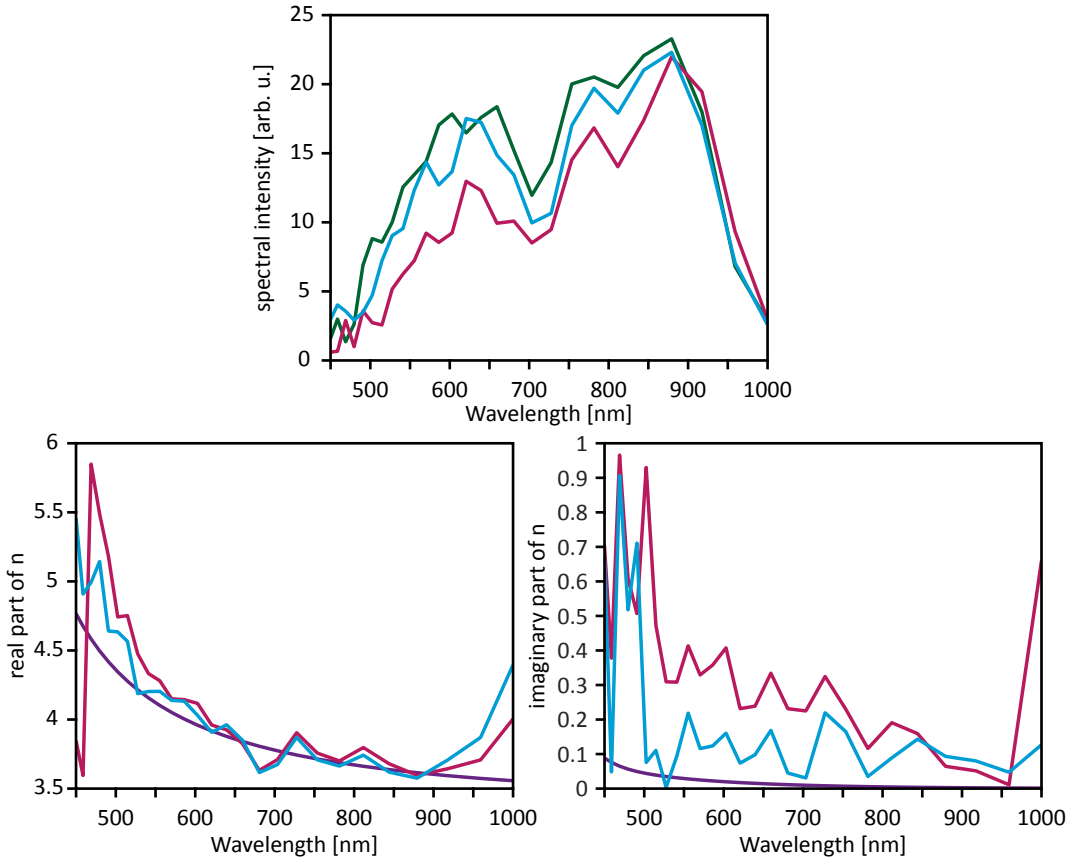

Figure 5.16: The three waveforms are Fourier transformed and this Fourier transformation is used to retrieve the spectral intensity (top panel) for the case of unperturbed (green), strong (red) and weak (blue) field. From this, the real and imaginary part of the refractive index, for the weak and strong electric field are retrieved and compared with literature values (purple). While the real part only slightly differs at short wavelengths, the imaginary part differs significantly. This is just another way to illustrate the enhanced absorption at high intensities of the incoming laser pulse.

viable tool for the real-time observation of strong-field interaction with a semiconductor. One main finding of this study is the very pronounced truncation of the electric field oscillations to the most intense half-cycles. This is a clear indication for nonlinear processes in silicon induced by the strong electric field. Moreover, indications were found that suggest the change of behaviour from a $\chi^{(3)}$ to a $\chi^{(2)}$ process, which can be explained in terms of a change from a two-photon absorption dominated process to the tunnelling regime [121]. In analogy to previous work [102], the transferred energy could be extracted from the measured data, which can be deconvolved into different contributions.
A way to retrieve the refractive index during the strong-field interaction is presented, that proves that this type of evaluation is in principle possible.

These results are highly interesting as they provide insight into the early stages of coherent excitation of electrons and track the dielectric function during the strong-field interaction. With further improvements in the existing technique or the development of new techniques in analogy to [122] measurements could be possible that allow for longer scan ranges due to shorter integration times. The recording of the pulse over a longer range provides better spectral resolution, e.g. for the retrieval of the refractive index. Additionally, a setup with two pulses, where one pulse excites the sample and a second time-delayed pulse probes the system, can provide further insights when recording the probe as function of the pump pulse. This is experimentally more challenging as it needs at least three pulses (a third one to measure the waveform of the probe pulse). However, it promises cleaner signals as excitation and induced nonlinear effects are probed independently.
Another approach is to use longer wavelength drivers or materials that do not have indirect band gaps, which are resonant to the spectrum of the laser pulse, then single-photon excitation is not possible anymore. Therefore, the signal from two-photon absorption is cleaner and additionally the transition to the tunnelling regime can be investigated.

Chapter 6

Summary and Outlook

This work demonstrates the direct manipulation of the magnetic momentum of matter by light. It establishes optical frequencies as a speed limit for magnetic manipulation, paving the way for future coherent spintronic devices. Additionally, the presented study proves that the electronic response of a metallic system follows the oscillations of a strong electromagnetic wave. Both effects are recorded with a resolution better than the half-cycle duration of the oscillations of the electric field of light.
A follow-up experiment shows that nanoparticles exhibit a similar behaviour as the bulk-like thin-film samples. Electronic excitation was measured by tracking the transient XUV absorption. The nanoparticles also show magnetic circular dichroism, when an external magnetic field is applied. This demonstrates that the nanoparticles possess a macroscopic, homogeneous magnetic moment.
The time-resolved study of strong-field interaction with a semiconductor witnesses nonlinear absorption confined to the most intense half-cycles of the electric field. The nonlinear response of silicon changes from a $\chi^{(3)}$-effect, indicating two-photon absorption, towards a $\chi^{(2)}$-effect, corresponding to tunnelling between valence and conduction band. In a non-time-resolved way the change of the refractive index, due to two-photon absorption, could be determined. The change of the refractive index is a mixed effect mainly caused by the two counteracting effects of free-carrier contributions from excited electrons and the Kerr effect. The detailed study of the change of refractive index has to be subject to future experiments with improved spectral resolution.

The results provide several possibilities for future studies a few of them shall be outlined here. The breakthrough in ultrafast magnetism is most likely the one with the most influence in the research field, as this work hopefully marks the starting point of ultrafast magnetism resolved on the attosecond timsescale. There are many directions to further develop this field and there are new questions that come up. Questions which will hopefully be answered by future research.
Computations for OISTR predict the increase of the magnetic moment in the constituent into which the spin transport happened. An experimental scheme that probes MCD in

two species at the same time could allow the measurement of this local increase.
Tailored correlated systems, such as Heusler compounds, are promising objects for ultrafast spin transfer. Specially designed nanostructures with an increased number of interfaces could maximize the OISTR effect. In principle this can enable the complete removal of magnetic moment in of the constituents within a few femtoseconds.
The extension to other measurement techniques, e.g. ARPES (angle-resolved photoelectron spectroscopy) or PEEM (photoemission electron microscopy) could give spatial information about the magnetic processes. ARPES can resolve electron dynamics in momentum space, whereas PEEM can be used to raster scan microscopic structures. Applying this to the tailored nanostructures can thus reveal valuable spatially resolved information about the magnetisation dynamics.
Free electron lasers (FEL) now provide pulses with durations below 1 fs which can cover the spectral range from the soft x-ray all the way up to the hard x-rays [123]. This enables studies at the absorption L-edges of the $3d$-transition metals. Using an FEL for time-resolved studies at the L-edges could be the right experiment to answer the question about the early time evolution of the spin and orbital angular momentum.
In future experiments on nanoparticles, the variety of the tunable parameters can be exploited. Especially the wide range of constituents allows for countless combinations and might favour unique behaviour. Special combinations of ferromagnetic and paramagnetic elements, that have been proven to allow all-optical switching of the magnetic state [124], might be able, in combination with the scalability of the nanoparticles, to pave the way towards data storage at Petahertz clock rates.

Appendix A

Appendix

A.1 FP3 Lasersystem and AS2 Beamline

The experiments were carried out at the Laboratory for Attosecond Physics (LAP) at the Max-Planck-Institute of Quantum Optics (MPQ). The lasersystem used was FP3 and the beamline was AS2, detailed descriptions of both can be found elsewhere [125, 126]. Only little modifications have been done to those systems.

Lasersystem FP3

The front-end is a Kerr lens passively mode-locked titanium-doped sapphire (Ti:Sa) oscillator. A frequency-doubled neodymium yttrium vanadate (Nd:YVO_4) CW laser (*Coherent Verdi V6*) pumps the Ti:Sapphire crystal. The output power of the Nd:YVO_4 pump laser is modulated by an acousto-optical modulator (AOM). The oscillator provides pulses with a duration of ~ 8 fs at a repetition rate of 78 MHz and a pulse energy of ~ 2.5 nJ.
The carrier-envelope-offset (CEO) of the output is stabilised using a fast loop, which adjusts the pump power by the AOM. The CEO frequency is measured by an f-to-0 scheme. The output pulse is focussed into a periodically-poled lithium-niobate crystal (PPLN) for difference frequency generation (DFG). A fast photodiode detects the beat signal between the fundamental and the DFG generated in the PPLN crystal [127]. After the oscillator and the f-to-0, the beam is directed through a 13.5 cm long SF57 glass block. This stretches the pulse duration to ~ 1 ps. The pulse is then amplified in a nine-pass chirped pulse amplifier (CPA) [128]. The gain medium of the CPA is again a Ti:Sapphire crystal, that is pumped by a frequency doubled Nd:YLF laser (*Photonics Industries DM30*). After four passes a Pockels cell reduces the repetition rate to 4 kHz a Dazzler (*FASTLITE*) corrects for higher-order dispersion effects. Subsequently the pulse passes 5 more times through the Ti:Sapphire crystal. At the exit of the CPA the pulses have an energy of 1 mJ.
The laser beam gets collimated and sent into a grating compressor, that compress the

pulse close to its Fourier limit of $\sim 20\,\text{fs}$. Due to gain narrowing the laser pulse loses significant spectral bandwidth in the amplification process. The laser pulse is then fo-

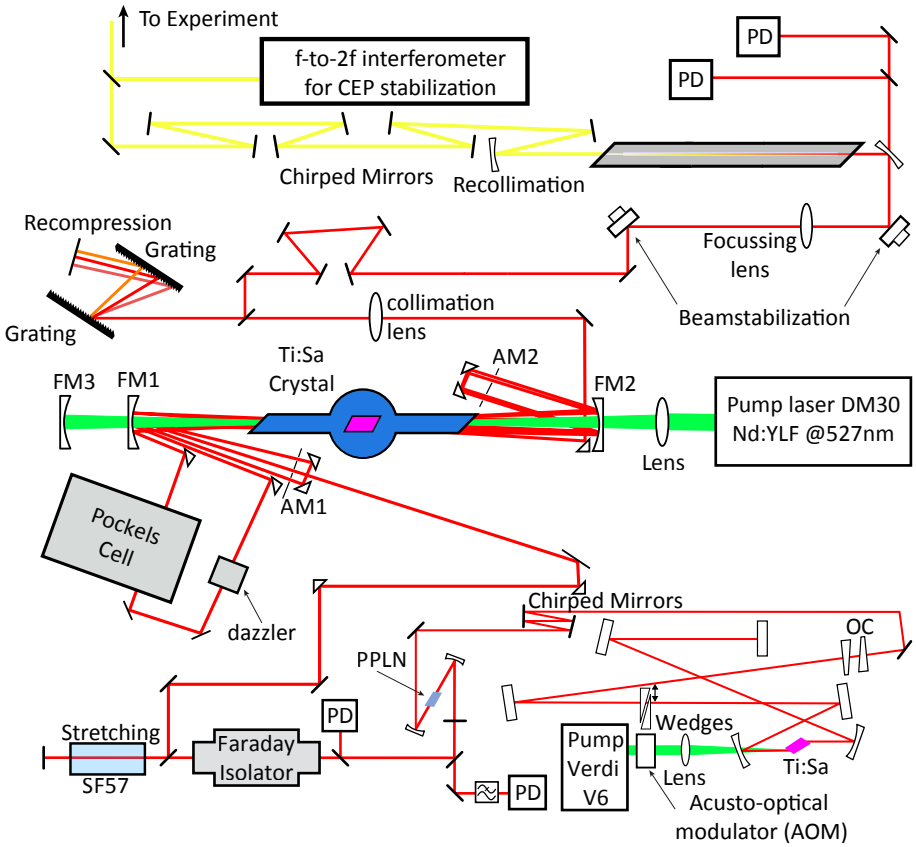

Figure A.1: The Lasersystem FP3 provides pulses with $0.5\,\mu\text{J}$ between $450 - 900\,\text{nm}$ compressed to $< 4\,\text{fs}$ at a repetition rate of $4\,\text{kHz}$. Adapted from [111].

cussed into a neon-filled hollow-core fibre (HCF), with a pressure of $\sim 1.6\,\text{bar}$. The high intensity of the laser pulse leads to new frequencies inside the HCF, due to self-phase modulation (SPM). A beam stabilization actively stabilizes the laser pulse spatially onto the entrance of the HCF.
After the $1.5\,\text{m}$ long HCF the spectrum spans from $350 - 1100\,\text{n}m$. Chirped mirrors compress frequencies between $450 - 900\,\text{nm}$ to a pulse duration below $4\,\text{fs}$, which corresponds to 1.5 cycles of the oscillating electric field at the central wavelength of $780\,\text{nm}$. Slow drifts of the CEO are compensated by a f-to-2f scheme. A fraction of the pulse is sent into a BBO crystal, generating second harmonic of the fundamental. This creates an interference in the spectral domain, where the two spectra overlap. This is fed back to the stretcher, after the oscillator, where a glass wedge compensates for the slow drifts.

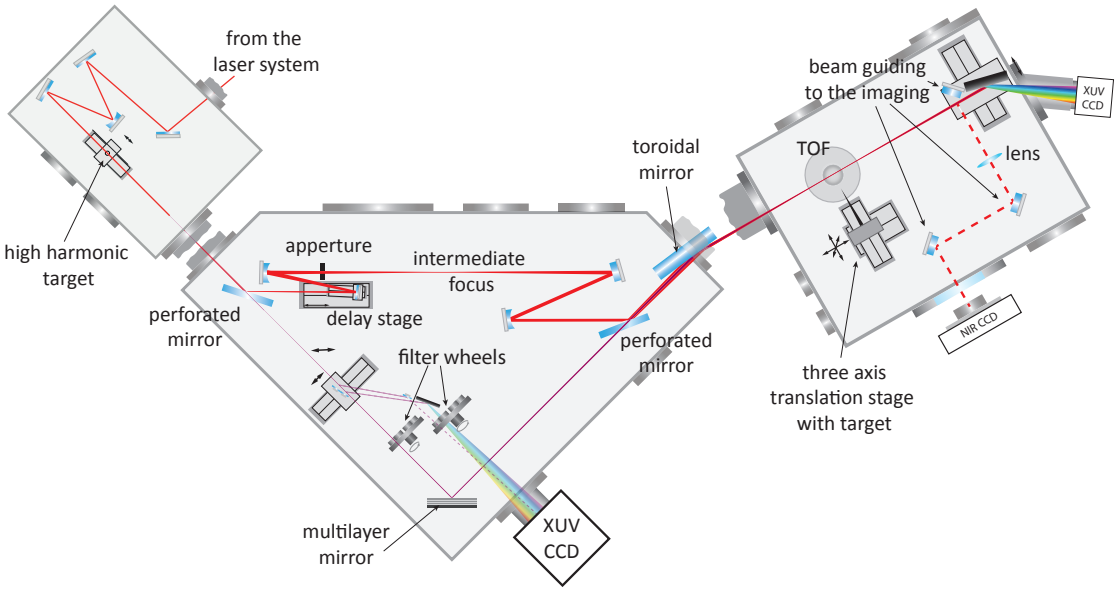

Figure A.2: The beamline of AS2 consists of three vacuum chamber: a chamber where the high-harmonic radiation is generated, a second chamber where the delay between the NIR pulse and the XUV pulse is introduced and a third chamber in which a time-of-flight and a grating spectrometer is located. Adapted from [129].

Beamline AS2

In the first chamber the near-infrared pulse (NIR) is focused into a ceramics target with a hole of $\sim 300\,\mu$m. The target is filled with a noble gas, typically neon for photon energies around 100 eV and above or argon for photon energies in the range between $60 - 80$ eV. The driving NIR and the generated XUV then propagate colinearly into the delay chamber.
A perforated mirror separates the NIR and the XUV, using that the XUV has lower divergence, due to the shorter wavelength. The XUV can be sent onto a XUV sensitive CCD camera, where it is imaged by a mirror and characterised using a diffraction grating. Metal foils serve as spectral filter, to filter the cut-off region and provide isolated attosecond pulses. A multilayer mirror for XUV further selects the desired spectrum and corrects for atto-chirp [130]. The XUV pulse is guided through a second perforated mirror, where it is recombined with the NIR.
The NIR that is reflected off the first perforated mirror, is intermediately focused to allow measurement such as APS. A mirror on a translation and a piezoelectric stage introduces a variable delay between the NIR and the XUV allowing for pump-probe measurements.
After the recombination, the two beams, are focused by a toroidal mirror under gracing incidence into the experimental chamber. Gracing incidence is chosen to minimize the reflection losses for the XUV.
In the experimental chamber a time-of-flight spectrometer can measure photoelectrons, e.g. for the attosecond streak camera. Another possible target are thin foils that can be investigated by attosecond transient absorption spectroscopy. For this purpose a toroidal grating is located in the experimental chamber that, diffracts the light onto a another XUV sensitive CCD camera. For alignment and diagnostics a CCD camera is installed outside the chamber. A beam guiding system can send the beam onto it.

A.2 Sample Preparation and Characterisation

The nickel thin-film and the nickel/platinum multilayer were grown on silicon membranes in fcc structure. The 8 nm Ni film and Pt(2)[Ni(4)Pt(2)]x2 Ni(2nm) multilayer were deposited on 200 nm thick polycrystalline silicon membranes (Norcada) at room temperature by electron beam evaporation under ultrahigh vacuum conditions. The individual layer thickness in the multilayer stack were optimized to increase the number of active interfaces for OISTR while maintaining sufficient XUV transmittance and providing maximized atto-MCD contrast. Additionally they had to be designed in a way that they sill magnetise homogeneously in-plane. The multilayer sample was protected by an inert 2 nm thick platinum capping layer and a 2 nm thick nickel seed layer was grown on the substrate to provide identical surrounding to all platinum layers and ensure uniform growth of the layer stack.
The in-plane magnetic properties were characterised by a standard longitudinal Magneto-Optical Kerr Effect (MOKE) setup with a 3 mW HeNe cw-laser, a photoelastic modulator and Glan-laser prisms in longitudinal geometry. Measurements on both, the frame and the samples membrane window, yield similar ferromagnetic properties. For both types of samples, we found coercive fields of a few mT and a remanence around 60-70 of the saturation magnetisation. MOKE measurements confirm the absence of ferromagnetism in the nickel seed layer at room temperature validating that the layer does not affect the magnetic moment of the sample. Sample production, sample shipping and experiments are performed under vacuum to prevent oxidation. Nevertheless, we confirmed that no change of the MOKE signal is observed after 48 hours exposure of the samples to air, ensuring that the ferromagnetic properties persist and do not suffer from an assumed oxidic passivation of the sample surface.

A.3 Computational Details for Magnetisation Dynamics TD-DFT Calculations

Computations rely on the Runge-Gross theorem establishing that the time-dependent external potential is a unique functional of the time dependent density, given the initial state [131]. Based on this theorem, a system of non-interacting particles can be chosen such that the density of this non-interacting system is equal to that of the interacting system for all times. The wave function is represented as a Slater determinant of single-particle Kohn-Sham (KS) orbitals. A fully non-collinear spin-dependent version of this theorem entails that these KS orbitals are two-component Pauli spinors determined by the equations:

$$i\hbar\frac{\partial\psi(\vec{r},t)}{\partial t} = \left(\frac{1}{2}\left(-i\nabla + \frac{1}{c}\vec{A}_{ext}(t)\right)^2 + v_s(\vec{r},t) + \frac{1}{2c}\sigma\vec{B}_s(\vec{r},t) + \frac{1}{2c}\sigma\Big(\nabla v_s(\vec{r},t)\times -i\nabla\Big)\right)\psi_j(\vec{r},t) \tag{A.1}$$

where the first term is the kinetic term and responsible for the flow of current across the interface [**?**]. $A_{ext}(t)$ is a vector potential representing the applied laser field, and σ are the Pauli matrices. The KS effective potential

$$v_s(\vec{r},t) = v_{ext}(\vec{r},t) + v_H(\vec{r},t) + v_{XC}(\vec{r},t) \tag{A.2}$$

is decomposed into the external potential $v_s(r,t)$, the classical electrostatic Hartree potential $v_H(r,t)$ and the exchange-correlation (XC) potential $v_{XC}(r,t)$. Similarly, the KS magnetic field is written as

$$B_s(r,t)(\vec{r},t) = B_{ext}(\vec{r},t) + B_H(\vec{r},t) + B_{XC}(\vec{r},t) \tag{A.3}$$

where $B_{ext}(\vec{r},t)$ is the magnetic field of the applied laser pulse plus possibly an additional magnetic field and $B_{XC}(\vec{r},t)$ is the XC magnetic field. The final term is the spin-orbit coupling term.

Calculations of a magneto-optical function for Ni/Pt layer were performed by a 3 step process: (i) The ground-state of Ni/Pt multilayers was determined using DFT, (ii) a fully spin-polarised GW calculation was performed to determine the correct position and width of nickel $3p$ states and (iii) finally the response function was calculated on top of GW-corrected Kohn-sham ground-state. This response function is calculated within linear response TD-DFT in which the excitonic effects [132] and local field effects can be easily included. The magneto-optical function was determined without any experimental parameter.

For a periodic sequence of 3 monolayers of nickel on 7 monolayers of platinum, a fully non-collinear version of TD-DFT as implemented within the Elk code [87] is used for all calculations presented here. Computational cost prohibits inclusion of more monolayers in the calculation. The results presented for Ni/Pt required 240 Xeon processors

constantly running for 47 days.
A regular mesh in k-space of 8x8x1 is used and a time step of t=2 as is employed for the time-propagation algorithm. To mimic experimental resolution, a Gaussian energy broadening is applied with spectral width of 0.027 eV. The laser pulse used in the present work is linearly polarised (out of plane polarisation) with central frequency of 1.55 eV, full-width-at-half-maximum duration 8 fs and fluence of 5.4 $\mathrm{mJ/cm^2}$.

A.4 Computational Details for Silicon TD-DFT Calculations

The calculations were performed in a coupled scheme, similar to the work for Sommer *et al.* [102]. The propagation of the laser pulse in vacuum is done by one-dimensional wave equation. The interaction with silicon was done by time dependent density functional theory, which is capable of calculating electron dynamics, as proposed by Yabana *et al.* [121].
The propagation of the of the pulse with the vector potential $A_z(t)$ of the wave along the z-axis is described by the wave-equation:

$$\frac{1}{c^2}\frac{\partial^2 A_z(t)}{\partial t^2} - \frac{\partial^2 A_z}{\partial z^2} = -\frac{4\pi e}{c} J_z(t) \tag{A.4}$$

$J_z(t)$ is the electric current and is obtained from the TD-DFT calculation. At each point z the electron orbitals $u_{nk}(r,t)$ are determined, that follow the Kohn-Sham equation.

$$i\hbar\frac{\partial}{\partial t}u_{nk}(\vec{r},t) = \left(\frac{1}{2m}\left(-\vec{p}+\hbar\vec{k}+\frac{e}{c}\vec{A}(t)\right)^2 + V_{ion} + V_H + V_{XC}\right)u_{nk}(\vec{r},t) \tag{A.5}$$

here e, m and $\hbar$ are the electron charge, its mass and the reduced Planck constant. u_{nk} is the Bloch orbital of the band with index n and the crystalline wave number k. V_{ion}, V_H and V_{XC} are the ionic potential, the Hartree potential and the exchange correlation potential. The vetorpotential $\vec{A}$ is given by the integral over the electric field of the laser pulse. To reproduce the band gap of the material, it is important that the exchange-correlation interaction is chosen good. Here, the MetaGGA is used [133].
The electronic current can be calculated from the Bloch orbitals according to [120]. the polarisation is then obtained by integrating the electric current density $\vec{J}(t)$ over time.

$$\vec{P}(t) = \int_t \vec{J}(t')dt'. \tag{A.6}$$

The oblique incidence problem is solved by reducing the equation depending on three variables x, y, t to two variables:

$$A(x,y,t) = A(x,\tau = t - \frac{y\sin\theta}{c}). \tag{A.7}$$

This gives expressions fot the 3-dimensional current density only depending on two variables and can be solved.
The input electric field was the waveform retrieved from the experiment. The calculations were performed on the Oakforest PACS supercomputer using 50 nodes. The real space grid consists of 16x16x16 points and the k-space grid has 8x8x8 points. The time steps are 1.92 as.

Appendix B

Data Preservation

The data is preserved in one folder and stored on MPQ's AFS server. Every figure has its own folder. For every figure there is the pure figure either as .eps or as .pdf file. The different chapters are organized slightly different.

Chapter 2
The .eps files are saved, no data was presented in this chapter.

Chapter 3
Each figure folder contains a ReadMe.txt data that explains how the results from the raw data were obtained. Most of them use the GUI that is in the chapter 3 folder. It can be run from this folder. The settings for the GUI are given either in screenshots or in separate .txt files. The data is in each of the figures folder.
Some Figures are then created in the GUI directly and can be exported from there, some datasets are exported from the GUI and then separately plotted. Those scripts are also stored in the individual folders.

Chapter 4
Each folder has the preprocessed data together with the script that creates the plot. The pdf are the plots as they are in the thesis.
The preprocessing happens with the GUI v3.m as it is in the folder of chapter 4. Each dataset in the folder has screenshot that shows the settings that were used for the evaluation with the GUI. Importing the data and evaluating it with the GUI according to the settings shown in the screenshot. This gives the results that are saved in the .txt files (TA.txt, XMCD.txt, Energy.txt).

Chapter 5
The raw data is processed by the DissStreakingSpectrogramEvaluation.m script. From

the Figure folder it is apparent which data set was used. This data set has to be imported into this script entering in line 28 the data in the format "YYYYMMDD" and in the following line the number of the scans. This data set can be exported and imported into the "DissPropertyEvaluation.m".
Then the the DissPropertyEvaluation.m is run to get the porperties from the datasets. Each folder contains the preprocessed data that then can be evaluated with the DissPropertyEvaluation.m, The relevant figures are produced by that script.

Bibliography

[1] Moore, G. E. Cramming more components onto integrated circuits, Reprinted from Electronics, volume 38, number 8, April 19, 1965, pp.114 ff. *IEEE Solid-State Circuits Society Newsletter* **11**, 33–35 (2009). URL `http://ieeexplore.ieee.org/document/4785860/`.

[2] IBM. IBM News room - 2017-06-05 IBM Research Alliance Builds New Transistor for 5nm Technology (2019) - date accessed (2019-12-06). URL `https://www-03.ibm.com/press/us/en/pressrelease/52531.wss`.

[3] Samsung. Samsung Electronics' Leadership in Advanced Foundry Technology Showcased with Latest Silicon Innovations and Ecosystem Platform (2019) - date accessed (2019-12-06). URL `https://news.samsung.com/global/samsung-electronics-leadership-in-advanced-foundry-technology-showcased-with-latest-silicon-innovations-and-ecosystem-platform`.

[4] Arute, F. *et al.* Quantum supremacy using a programmable superconducting processor. *Nature* **574**, 505–510 (2019). URL `http://www.nature.com/articles/s41586-019-1666-5`.

[5] Wolf, S. A. Spintronics: A Spin-Based Electronics Vision for the Future. *Science* **294**, 1488–1495 (2001). URL `http://www.sciencemag.org/cgi/doi/10.1126/science.1065389`.

[6] Baibich, M. N. *et al.* Giant magnetoresistance of (001)Fe/(001)Cr magnetic superlattices. *Physical Review Letters* **61**, 2472–2475 (1988). URL `https://link.aps.org/doi/10.1103/PhysRevLett.61.2472`.

[7] Binasch, G., Grünberg, P., Saurenbach, F. & Zinn, W. Enhanced magnetoresistance in layered magnetic structures with antiferromagnetic interlayer exchange. *Physical Review B* **39**, 4828–4830 (1989). URL `https://link.aps.org/doi/10.1103/PhysRevB.39.4828`.

[8] Ørstedt, J. C. Experimenta circa effectum Conflictus electrici in Acum magneticam. *Journal für Chemie und Physik* **29**, 275–281 (1820). URL `https://reader.digitale-sammlungen.de/de/fs1/object/display/bsb10073853_00255.html`.

[9] Faraday, M. I. Experimental researches in electricity.—Nineteenth series. *Philosophical Transactions of the Royal Society of London* **136**, 1–20 (1846). URL http://www.royalsocietypublishing.org/doi/10.1098/rstl.1846.0001.

[10] Maxwell, J. C. VIII. A dynamical theory of the electromagnetic field. *Philosophical Transactions of the Royal Society of London* **155**, 459–512 (1865). URL http://www.royalsocietypublishing.org/doi/10.1098/rstl.1865.0008.

[11] Beaurepaire, E., Merle, J.-C., Daunois, A. & Bigot, J.-Y. Ultrafast Spin Dynamics in Ferromagnetic Nickel. *Physical Review Letters* **76**, 4250–4253 (1996). URL https://link.aps.org/doi/10.1103/PhysRevLett.76.4250.

[12] Stamm, C. *et al.* Femtosecond modification of electron localization and transfer of angular momentum in nickel. *Nature Materials* **6**, 740–743 (2007). URL http://www.nature.com/articles/nmat1985.

[13] Bigot, J.-Y., Vomir, M. & Beaurepaire, E. Coherent ultrafast magnetism induced by femtosecond laser pulses. *Nature Physics* **5**, 515–520 (2009). URL http://www.nature.com/articles/nphys1285.

[14] Boeglin, C. *et al.* Distinguishing the ultrafast dynamics of spin and orbital moments in solids. *Nature* **465**, 458–461 (2010). URL http://www.nature.com/articles/nature09070.

[15] La-O-Vorakiat, C. *et al.* Ultrafast Demagnetization Measurements Using Extreme Ultraviolet Light: Comparison of Electronic and Magnetic Contributions. *Physical Review X* **2**, 011005 (2012). URL https://link.aps.org/doi/10.1103/PhysRevX.2.011005.

[16] Eschenlohr, A. *et al.* Ultrafast spin transport as key to femtosecond demagnetization. *Nature Materials* **12**, 332–336 (2013). URL http://www.nature.com/articles/nmat3546.

[17] Kirilyuk, A., Kimel, A. V. & Rasing, T. Ultrafast optical manipulation of magnetic order. *Reviews of Modern Physics* **82**, 2731–2784 (2010). URL https://link.aps.org/doi/10.1103/RevModPhys.82.2731.

[18] Hellman, F. *et al.* Interface-induced phenomena in magnetism. *Reviews of Modern Physics* **89**, 025006 (2017). URL http://link.aps.org/doi/10.1103/RevModPhys.89.025006.

[19] Battiato, M., Carva, K. & Oppeneer, P. M. Superdiffusive Spin Transport as a Mechanism of Ultrafast Demagnetization. *Physical Review Letters* **105**, 027203 (2010). URL https://link.aps.org/doi/10.1103/PhysRevLett.105.027203.

[20] Melnikov, A. *et al.* Ultrafast transport of laser-excited spin-polarized carriers in Au/Fe/MgO(001). *Physical Review Letters* **107**, 076601 (2011). URL https://link.aps.org/doi/10.1103/PhysRevLett.107.076601.

[21] Schellekens, A. J., Kuiper, K. C., De Wit, R. R. & Koopmans, B. Ultrafast spin-transfer torque driven by femtosecond pulsed-laser excitation. *Nature Communications* **5**, 4333 (2014). URL http://www.nature.com/articles/ncomms5333.

[22] Choi, G.-M., Min, B.-C., Lee, K.-J. & Cahill, D. G. Spin current generated by thermally driven ultrafast demagnetization. *Nature Communications* **5**, 4334 (2014). URL http://www.nature.com/articles/ncomms5334.

[23] He, W., Zhu, T., Zhang, X. Q., Yang, H. T. & Cheng, Z. H. Ultrafast demagnetization enhancement in CoFeB/MgO/CoFeB magnetic tunneling junction driven by spin tunneling current. *Scientific Reports* **3**, 2883 (2013). URL http://www.nature.com/articles/srep02883.

[24] Khorsand, A. R., Savoini, M., Kirilyuk, A. & Rasing, T. Optical excitation of thin magnetic layers in multilayer structures. *Nature Materials* **13**, 101–102 (2014). URL http://www.nature.com/articles/nmat3850.

[25] Eschenlohr, A. *et al.* Reply to 'Optical excitation of thin magnetic layers in multilayer structures' (2014). URL http://www.nature.com/articles/nmat3851.

[26] Stanciu, C. D. *et al.* All-optical magnetic recording with circularly polarized light. *Physical Review Letters* **99**, 047601 (2007). URL https://link.aps.org/doi/10.1103/PhysRevLett.99.047601.

[27] Krausz, F. & Ivanov, M. Attosecond physics. *Reviews of Modern Physics* **81**, 163–234 (2009). URL https://link.aps.org/doi/10.1103/RevModPhys.81.163.

[28] Krausz, F. The birth of attosecond physics and its coming of age. *Physica Scripta* **91**, 063011 (2016). URL http://stacks.iop.org/1402-4896/91/i=6/a=063011?key=crossref.cc53814acc79f842f3bef70739b5e96e.

[29] Hentschel, M. *et al.* Attosecond metrology. *Nature* **414**, 509–513 (2001). URL http://www.nature.com/articles/35107000.

[30] Itatani, J. *et al.* Attosecond streak camera. *Physical review letters* **88**, 173903 (2002). URL http://link.aps.org/doi/10.1103/PhysRevLett.88.173903.

[31] Itatani, J. *et al.* Tomographic imaging of molecular orbitals. *Nature* **432**, 867–871 (2004). URL http://www.nature.com/articles/nature03183.

[32] Kling, M. F. Control of Electron Localization in Molecular Dissociation. *Science* **312**, 246–248 (2006). URL http://www.sciencemag.org/cgi/doi/10.1126/science.1126259.

[33] Uiberacker, M. *et al.* Attosecond real-time observation of electron tunnelling in atoms. *Nature* **446**, 627–632 (2007). URL http://www.nature.com/doifinder/10.1038/nature05648.

[34] Goulielmakis, E. *et al.* Real-time observation of valence electron motion. *Nature* **466**, 739–743 (2010). URL http://www.nature.com/articles/nature09212.

[35] Cavalieri, A. L. *et al.* Attosecond spectroscopy in condensed matter. *Nature* **449**, 1029–1032 (2007). URL http://www.nature.com/doifinder/10.1038/nature06229.

[36] Schultze, M. *et al.* Controlling dielectrics with the electric field of light. *Nature* **493**, 75–78 (2013). URL http://www.nature.com/articles/nature11720.

[37] Schultze, M. *et al.* Attosecond band-gap dynamics in silicon. *Science* **346**, 1348–1352 (2014). URL http://www.sciencemag.org/content/346/6215/1348.abstract.

[38] Lucchini, M. *et al.* Attosecond dynamical Franz-Keldysh effect in polycrystalline diamond. *Science* **353**, 916–919 (2016). URL http://www.sciencemag.org/cgi/doi/10.1126/science.aag1268.

[39] Ghimire, S. *et al.* Strong-field and attosecond physics in solids. *Journal of Physics B: Atomic, Molecular and Optical Physics* **47**, 204030 (2014). URL http://stacks.iop.org/0953-4075/47/i=20/a=204030?key=crossref.668e45d6bb321024e73e867b72ee7aa4.

[40] Luu, T. T. *et al.* Extreme ultraviolet high-harmonic spectroscopy of solids. *Nature* **521**, 498–502 (2015). URL http://www.nature.com/articles/nature14456.

[41] Garg, M. *et al.* Multi-petahertz electronic metrology. *Nature* **538**, 359–363 (2016). URL http://www.nature.com/articles/nature19821.

[42] Höchst, H., Patel, R. & Middleton, F. Multiple-reflection phase shifter: A viable alternative to generate circular-polarized synchrotron radiation. *Nuclear Instruments and Methods in Physics Research Section A: Accelerators, Spectrometers, Detectors and Associated Equipment* **347**, 107–114 (1994). URL https://linkinghub.elsevier.com/retrieve/pii/0168900294918643.

[43] Vodungbo, B. *et al.* Laser-induced ultrafast demagnetization in the presence of a nanoscale magnetic domain network. *Nature Communications* **3**, 999 (2012). URL http://www.nature.com/articles/ncomms2007.

[44] Gross, R. & Marx, A. *Festkoerperphysik* (De Gruyter, 2014).

[45] Baberschke, K., Nolting, W. & Donath, M. (eds.) *Band-Ferromagnetism*, vol. 580 of *Lecture Notes in Physics* (Springer Berlin Heidelberg, Berlin, Heidelberg, 2001). URL http://link.springer.com/10.1007/3-540-44610-9.

[46] Bloch, F. Über die Quantenmechanik der Elektronen in Kristallgittern. *Zeitschrift für Physik* **52**, 555–600 (1929). URL http://link.springer.com/10.1007/BF01339455.

[47] Mott, N. F. A discussion of the transition metals on the basis of quantum mechanics (1935). URL http://stacks.iop.org/0959-5309/47/i=4/a=305?key=crossref.649ebea76cb5a52612211df15483886b.

[48] Slater, J. C. The ferromagnetism of nickel. *Physical Review* **49**, 537–545 (1936). URL https://link.aps.org/doi/10.1103/PhysRev.49.537.

[49] Stoner, E. Collective electron ferronmagnetism. *Proceedings of the Royal Society of London. Series A. Mathematical and Physical Sciences* **165**, 372–414 (1938). URL http://www.royalsocietypublishing.org/doi/10.1098/rspa.1938.0066.

[50] Schwabl, F. *Statistical mechanics* (Springer, 2006).

[51] Stöhr, J. & Siegmann, H. C. *Magnetism* (Springer Berlin Heidelberg, Berlin, Heidelberg, 2006). URL http://link.springer.com/10.1007/978-3-540-30283-4.

[52] Stöhr, J. & Wu, Y. X-Ray Magnetic Circular Dichroism: Basic Concepts and Theory for 3D Transition Metal Atoms. In *New Directions in Research with Third-Generation Soft X-Ray Synchrotron Radiation Sources*, 221–250 (Springer Netherlands, Dordrecht, 1994). URL http://link.springer.com/10.1007/978-94-011-0868-3_9.

[53] Bethe, H. A. & Salpeter, E. E. *Quantum Mechanics of One- and Two-Electron Atoms* (Springer US, Boston, MA, 1977). URL http://link.springer.com/10.1007/978-1-4613-4104-8.

[54] Erskine, J. L. & Stern, E. A. Calculation of the M 2,3 magneto-optical absorption spectrum of ferromagnetic nickel. *Physical Review B* **12**, 5016–5024 (1975). URL https://link.aps.org/doi/10.1103/PhysRevB.12.5016.

[55] Schütz, G. *et al.* Absorption of circularly polarized x-rays in iron. *Physical Review Letters* **58**, 737–740 (1987). URL https://link.aps.org/doi/10.1103/PhysRevLett.58.737.

[56] Schütz, G. *et al.* Spin-dependent photoabsorption at the L-edges of ferromagnetic Gd and Tb metal. *Zeitschrift für Physik B Condensed Matter* **73**, 67–75 (1988). URL http://link.springer.com/10.1007/BF01312156.

[57] Kittel, C. *Einführung in die Festkoerperphysik* (Oldenbourg, 2002). URL https://www.degruyter.com/view/product/231310.

[58] Thole, B. T., Carra, P., Sette, F. & van der Laan, G. X-ray circular dichroism as a probe of orbital magnetization. *Physical Review Letters* **68**, 1943–1946 (1992). URL https://link.aps.org/doi/10.1103/PhysRevLett.68.1943.

[59] Carra, P., Thole, B. T., Altarelli, M. & Wang, X. X-ray circular dichroism and local magnetic fields. *Physical Review Letters* **70**, 694–697 (1993). URL https://link.aps.org/doi/10.1103/PhysRevLett.70.694.

[60] Wu, R., Wang, D. & Freeman, A. J. First principles investigation of the validity and range of applicability of the x-ray magnetic circular dichroism sum rule. *Phys-*

ical Review Letters **71**, 3581–3584 (1993). URL https://link.aps.org/doi/10.1103/PhysRevLett.71.3581.

[61] Wu, R. & Freeman, A. J. Limitation of the Magnetic-Circular-Dichroism Spin Sum Rule for Transition Metals and Importance of the Magnetic Dipole Term. *Physical Review Letters* **73**, 1994–1997 (1994). URL https://link.aps.org/doi/10.1103/PhysRevLett.73.1994.

[62] Stöhr, J. X-ray magnetic circular dichroism spectroscopy of transition metal thin films. *Journal of Electron Spectroscopy and Related Phenomena* **75**, 253–272 (1995). URL https://www.sciencedirect.com/science/article/pii/0368204895025375.

[63] Peschel, G. Landolt-Börnstein, Zahlenwerte und Funktionen aus Physik, Chemie, Astronomie, Geophysik und Technik. *Zeitschrift für Physikalische Chemie* **76**, 111–111 (1971). URL https://www.springer.com/series/284.

[64] Sorg, C. *Magnetic Properties of 3d and 4f Ferromagnets Studied by X-Ray Absorption Spectroscopy.* Phd thesis, Freie Universität Berlin (2005).

[65] Chen, C. T. *et al.* Experimental Confirmation of the X-Ray Magnetic Circular Dichroism Sum Rules for Iron and Cobalt. *Physical Review Letters* **75**, 152–155 (1995). URL https://link.aps.org/doi/10.1103/PhysRevLett.75.152.

[66] Stamm, C., Pontius, N., Kachel, T., Wietstruk, M. & Dürr, H. A. Femtosecond x-ray absorption spectroscopy of spin and orbital angular momentum in photoexcited Ni films during ultrafast demagnetization. *Physical Review B* **81**, 104425 (2010). URL https://link.aps.org/doi/10.1103/PhysRevB.81.104425.

[67] Ebert, H., Stöhr, J., Parkin, S. & Samant, M. L-edge x-ray absorption in fcc and bcc Cu metal: Comparison of experimental and first-principles theoretical results. *Physical Review B - Condensed Matter and Materials Physics* **53**, 16067–16073 (1996). URL https://link.aps.org/doi/10.1103/PhysRevB.53.16067.

[68] Koide, T., Shidara, T., Yuri, M., Kandaka, N. & Fukutani, H. Production and direct measurement of circularly polarized vacuum-ultraviolet light with multireflection optics. *Applied Physics Letters* **58**, 2592–2594 (1991). URL http://aip.scitation.org/doi/10.1063/1.104832.

[69] Shin, S., Suga, S., Kanzaki, H., Shibuya, S. & Yanaguchi, T. Multiplet structures of the inner core absorption spectra of KMnF3 and KCoF3 measured by synchrotron radiation. *Solid State Communications* **38**, 1281–1284 (1981). URL https://www.sciencedirect.com/science/article/pii/0038109881910061.

[70] Wang, X., Leung, T. C., Harmon, B. N. & Carra, P. Circular magnetic x-ray dichroism in the heavy rare-earth metals. *Physical Review B* **47**, 9087–9090 (1993). URL https://link.aps.org/doi/10.1103/PhysRevB.47.9087.

[71] Ankudinov, A. L., Rehr, J. J., Wende, H., Scherz, A. & Baberschke, K. Spin-dependent sum rules for X-ray absorption spectra. *Europhysics Letters (EPL)* **66**, 441–447 (2004). URL http://stacks.iop.org/0295-5075/66/i=3/a=441?key=crossref.e9dd030dc4b21b0e8977620710003142.

[72] Scherz, A. *Spin-dependent X-ray Absorption Spectroscopy of 3d Transition Metals: Systematics and Applications*. Phd thesis, Freie Universität Berlin (2003).

[73] Teramura, Y., Tanaka, A. & Jo, T. Effect of Coulomb Interaction on the X-Ray Magnetic Circular Dichroism Spin Sum Rule in 3d Transition Elements. *Journal of the Physical Society of Japan* **65**, 1053–1055 (1996). URL http://journals.jps.jp/doi/10.1143/JPSJ.65.1053.

[74] Scherz, A. *et al.* Limitations of Integral XMCD SumRules for the Early 3d Elements. *Physica Scripta* **2005**, 586 (2005). URL http://www.physica.org/xml/article.asp?article=t115a00586.xml.

[75] Wu, Y., Stöhr, J., Hermsmeier, B. D., Samant, M. G. & Weller, D. Enhanced orbital magnetic moment on Co atoms in Co/Pd multilayers: A magnetic circular x-ray dichroism study. *Physical Review Letters* **69**, 2307–2310 (1992). URL https://link.aps.org/doi/10.1103/PhysRevLett.69.2307.

[76] Vogel, J. & Sacchi, M. Polarization and angular dependence of the L 2 , 3 absorption edges in Ni(110). *Physical Review B* **49**, 3230–3234 (1994). URL https://link.aps.org/doi/10.1103/PhysRevB.49.3230.

[77] Böske, T., Clemens, W., Carbone, C. & Eberhardt, W. Circular magnetic x-ray dichroism of 3d impurities in Ni. *Physical Review B* **49**, 4003–4009 (1994). URL https://link.aps.org/doi/10.1103/PhysRevB.49.4003.

[78] Chen, C. T., Sette, F., Ma, Y. & Modesti, S. Soft-x-ray magnetic circular dichroism at the L 2,3 edges of nickel. *Physical Review B* **42**, 7262–7265 (1990). URL https://link.aps.org/doi/10.1103/PhysRevB.42.7262.

[79] Dewhurst, J. K., Elliott, P., Shallcross, S., Gross, E. K. U. & Sharma, S. Laser-Induced Intersite Spin Transfer. *Nano Letters* **18**, 1842–1848 (2018). URL http://pubs.acs.org/doi/10.1021/acs.nanolett.7b05118.

[80] Dewhurst, J. K., Shallcross, S., Gross, E. K. & Sharma, S. Substrate-Controlled Ultrafast Spin Injection and Demagnetization. *Physical Review Applied* **10**, 044065 (2018). URL https://link.aps.org/doi/10.1103/PhysRevApplied.10.044065.

[81] Siegrist, F. *et al.* Light-wave dynamic control of magnetism. *Nature* **571**, 240–244 (2019). URL http://www.nature.com/articles/s41586-019-1333-x.

[82] Vodungbo, B. *et al.* Polarization control of high order harmonics in the EUV photon energy range. *Optics Express* **19**, 4346 (2011). URL https://www.osapublishing.org/oe/abstract.cfm?uri=oe-19-5-4346.

[83] Hecht, E. *Optik* (De Gruyter, Berlin, Boston, 2018). URL http://www.degruyter.com/view/books/9783110526653/9783110526653/9783110526653.xml.

[84] Rabinovitch, K., Canfield, L. R. & Madden, R. P. A Method for Measuring Polarization in the Vacuum Ultraviolet. *Applied Optics* **4**, 1005 (1965). URL https://www.osapublishing.org/abstract.cfm?URI=ao-4-8-1005.

[85] Chang, Y.-P. *Circularly Polarized Attosecond Pulses for Time-Resolved XUV Spectroscopy*. Master thesis, Ludwig-Maximilians-Universität München (2017).

[86] Volkov, M. *et al.* Attosecond screening dynamics mediated by electron localization in transition metals. *Nature Physics* 1–5 (2019). URL http://www.nature.com/articles/s41567-019-0602-9.

[87] Dewhurst, J., Sharma, S. & Gross, E. The Elk Code. URL http://elk.sourceforge.net/.

[88] Willems, F. *et al.* Magneto-Optical Functions at the 3p Resonances of Fe, Co, and Ni: Ab initio Description and Experiment. *Physical Review Letters* **122**, 217202 (2019). URL https://link.aps.org/doi/10.1103/PhysRevLett.122.217202.

[89] Bergeard, N. *et al.* Ultrafast angular momentum transfer in multisublattice ferrimagnets. *Nature Communications* **5**, 3466 (2014). URL http://www.nature.com/articles/ncomms4466.

[90] Elliott, P., Müller, T., Dewhurst, J. K., Sharma, S. & Gross, E. K. U. Ultrafast laser induced local magnetization dynamics in Heusler compounds. *Scientific Reports* **6**, 38911 (2016). URL http://www.nature.com/articles/srep38911.

[91] Link, S. & El-Sayed, M. A. Optical Properties and Ultrafast Dynamics of Metallic Nanocrystals. *Annual Review of Physical Chemistry* **54**, 331–366 (2003). URL http://www.annualreviews.org/doi/10.1146/annurev.physchem.54.011002.103759.

[92] Bansmann, J. *et al.* Magnetic and structural properties of isolated and assembled clusters. *Surface Science Reports* **56**, 189–275 (2005). URL https://www.sciencedirect.com/science/article/pii/S0167572904001001.

[93] Heiz, U. & Landmann, U. (eds.) *Nanocatalysis* (Springer-Verlag, Berlin, Heidelberg, 2007).

[94] Thaler, P. *et al.* Synthesis of nanoparticles in helium droplets - A characterization comparing mass-spectra and electron microscopy data. *Journal of Chemical Physics* **143**, 134201 (2015). URL http://scitation.aip.org/content/aip/journal/jcp/143/13/10.1063/1.4932182.

[95] Boyer, P., Mènard, D. & Meunier, M. Nanoclustered Co-Au particles fabricated by femtosecond laser fragmentation in liquids. *Journal of Physical Chemistry C* **114**, 13497–13500 (2010). URL https://pubs.acs.org/doi/10.1021/jp1037552.

[96] Ban, Z., Barnakov, Y. A., Li, F., Golub, V. O. & O'Connor, C. J. The synthesis of core-shell iron@gold nanoparticles and their characterization. *Journal of Materials Chemistry* **15**, 4660–4662 (2005). URL http://xlink.rsc.org/?DOI=b504304b.

[97] Xia, Y. *et al.* One-Dimensional Nanostructures: Synthesis, Characterization, and Applications. *Advanced Materials* **15**, 353–389 (2003). URL http://doi.wiley.com/10.1002/adma.200390087.

[98] Cademartiri, L. & Ozin, G. A. Ultrathin Nanowires-A Materials Chemistry Perspective. *Advanced Materials* **21**, 1013–1020 (2009). URL http://doi.wiley.com/10.1002/adma.200801836.

[99] Biesinger, M. C., Payne, B. P., Lau, L. W. M., Gerson, A. & Smart, R. S. C. X-ray photoelectron spectroscopic chemical state quantification of mixed nickel metal, oxide and hydroxide systems. *Surface and Interface Analysis* **41**, 324–332 (2009). URL http://doi.wiley.com/10.1002/sia.3026.

[100] Brice-Profeta, S. *et al.* Magnetic order in γ-Fe2O3 nanoparticles: A XMCD study. *Journal of Magnetism and Magnetic Materials* **288**, 354–365 (2005). URL https://www.sciencedirect.com/science/article/pii/S0304885304010649.

[101] Yang, S. *et al.* Robust Ferromagnetism of Chromium Nanoparticles Formed in Superfluid Helium. *Advanced Materials* **29**, 1604277 (2017). URL http://doi.wiley.com/10.1002/adma.201604277.

[102] Sommer, A. *et al.* Attosecond nonlinear polarization and light–matter energy transfer in solids. *Nature* **534**, 86–90 (2016). URL http://www.nature.com/doifinder/10.1038/nature17650.

[103] Corkum, P. B. Plasma perspective on strong field multiphoton ionization. *Physical Review Letters* **71**, 1994–1997 (1993). URL http://journals.aps.org/prl/abstract/10.1103/PhysRevLett.71.1994.

[104] Kienberger, R. *et al.* Atomic transient recorder. *Nature* **427**, 817–821 (2004). URL http://www.nature.com/articles/nature02277.

[105] Goulielmakis, E. Direct Measurement of Light Waves. *Science* **305**, 1267–1269 (2004). URL http://www.sciencemag.org/cgi/doi/10.1126/science.1100866.

[106] Boyd, R. W. *Nonlinear optics* (Academic Press, 2008).

[107] Sutherland, R. L., McLean, D. G. & Kirkpatrick, S. *Handbook of nonlinear optics.* (Marcel Dekker, 2003). URL https://www.crcpress.com/Handbook-of-Nonlinear-Optics/Sutherland/p/book/9780824742430.

[108] Sabbah, A. J. & Riffe, D. M. Femtosecond pump-probe reflectivity study of silicon carrier dynamics. *Physical Review B - Condensed Matter and Materials Physics* **66**, 1–11 (2002). URL https://link.aps.org/doi/10.1103/PhysRevB.66.165217.

[109] Drude, P. Zur Elektronentheorie der Metalle. *Annalen der Physik* **306**, 566–613 (1900). URL http://doi.wiley.com/10.1002/andp.19003060312.

[110] Wooten, F. F. Optical properties of solids. (Academic Press, 1972).

[111] Schröder, M. C. *Ultrafast Electron Dynamics in Semiconductor and Ferromagnetic Materials*. Master thesis, Ludwig-Maximilians-Universität (2018).

[112] Dragonmir, A., McInerney, J. G. & Nikogosyan, D. N. Femtosecond measurements of two-photon absorption coefficients at $\lambda = 264$ nm in glasses, crystals, and liquids (2002). URL https://www.osapublishing.org/abstract.cfm?URI=ao-41-21-4365.

[113] Schinke, C. *et al.* Uncertainty analysis for the coefficient of band-to-band absorption of crystalline silicon. *AIP Advances* **5**, 067168 (2015). URL http://aip.scitation.org/doi/10.1063/1.4923379.

[114] Bristow, A. D., Rotenberg, N. & van Driel, H. M. Two-photon absorption and Kerr coefficients of silicon for 850–2200nm. *Applied Physics Letters* **90**, 191104 (2007). URL http://aip.scitation.org/doi/10.1063/1.2737359.

[115] Lin, Q. *et al.* Dispersion of silicon nonlinearities in the near infrared region. *Applied Physics Letters* **91**, 021111 (2007). URL http://aip.scitation.org/doi/10.1063/1.2750523.

[116] Yu, P. Y. & Cardona, M. *Fundamentals of Semiconductors*. Graduate Texts in Physics (Springer Berlin Heidelberg, Berlin, Heidelberg, 2010). URL http://link.springer.com/10.1007/978-3-642-00710-1.

[117] Qasim, M., Wismer, M. S., Agarwal, M. & Yakovlev, V. S. Ensemble properties of charge carriers injected by an ultrashort laser pulse. *Physical Review B* **98**, 214304 (2018). URL https://link.aps.org/doi/10.1103/PhysRevB.98.214304. 1804.09030.

[118] Green, M. A. & Keevers, M. J. Optical properties of intrinsic silicon at 300 K. *Progress in Photovoltaics: Research and Applications* **3**, 189–192 (1995). URL http://doi.wiley.com/10.1002/pip.4670030303.

[119] Keldysh, L. V. Ionization in the field of a strong electromagnetic wave. *Soviet Physics JETP* **20**, 1307–1314 (1965). URL http://www.jetp.ac.ru/cgi-bin/e/index/e/20/5/p1307?a=list.

[120] Uemoto, M., Kuwabara, Y., Sato, S. A. & Yabana, K. Nonlinear polarization evolution using time-dependent density functional theory. *Journal of Chemical*

Physics **150**, 094101 (2019). URL http://aip.scitation.org/doi/10.1063/1.5068711. 1810.06500.

[121] Yabana, K., Sugiyama, T., Shinohara, Y., Otobe, T. & Bertsch, G. F. Time-dependent density functional theory for strong electromagnetic fields in crystalline solids. *Physical Review B* **85**, 045134 (2012). URL https://link.aps.org/doi/10.1103/PhysRevB.85.045134.

[122] Schiffrin, A. *et al.* Optical-field-induced current in dielectrics. *Nature* **493**, 70–74 (2013). URL http://www.nature.com/articles/nature11567.

[123] Duris, J. *et al.* Tunable isolated attosecond X-ray pulses with gigawatt peak power from a free-electron laser. *Nature Photonics* 1–7 (2019). URL http://www.nature.com/articles/s41566-019-0549-5. 1906.10649.

[124] Lalieu, M. L. M., Lavrijsen, R. & Koopmans, B. Integrating all-optical switching with spintronics. *Nature Communications* **10**, 110 (2019). URL http://www.nature.com/articles/s41467-018-08062-4.

[125] Schweinberger, W. *et al.* Waveform-controlled near-single-cycle milli-joule laser pulses generate sub-10 nm extreme ultraviolet continua. *Optics Letters* **37**, 3573 (2012). URL https://www.osapublishing.org/abstract.cfm?URI=ol-37-17-3573.

[126] Fiess, M. *et al.* Versatile apparatus for attosecond metrology and spectroscopy. *Review of Scientific Instruments* **81**, 093103 (2010). URL http://scitation.aip.org/content/aip/journal/rsi/81/9/10.1063/1.3475689.

[127] Fuji, T. *et al.* Monolithic carrier-envelope phase-stabilization scheme. *Optics Letters* **30**, 332 (2005). URL https://www.osapublishing.org/abstract.cfm?URI=ol-30-3-332.

[128] Strickland, D. & Mourou, G. Compression of amplified chirped optical pulses. *Optics Communications* **56**, 219–221 (1985). URL http://linkinghub.elsevier.com/retrieve/pii/0030401885901208.

[129] Siegrist, F. *Attosecond Dynamics Based on Electron Correlation and Excitation.* Master's thesis, TU München (2016).

[130] Guggenmos, A., Cui, Y., Heinrich, S. & Kleineberg, U. Attosecond pulse shaping by multilayer mirrors (2018). URL http://www.mdpi.com/2076-3417/8/12/2503.

[131] Runge, E. & Gross, E. K. U. Density-Functional Theory for Time-Dependent Systems. *Physical Review Letters* **52**, 997–1000 (1984). URL https://link.aps.org/doi/10.1103/PhysRevLett.52.997.

[132] Sharma, S., Dewhurst, J. K., Sanna, A. & Gross, E. K. U. Bootstrap Approximation for the Exchange-Correlation Kernel of Time-Dependent Density-

Functional Theory. *Physical Review Letters* **107**, 186401 (2011). URL https://link.aps.org/doi/10.1103/PhysRevLett.107.186401.

[133] Tran, F. & Blaha, P. Accurate band gaps of semiconductors and insulators with a semilocal exchange-correlation potential. *Physical Review Letters* **102**, 226401 (2009). URL https://link.aps.org/doi/10.1103/PhysRevLett.102.226401.

Danksagung

Mein größter Dank gebührt Martin Schultze, für die Unterstützung, die schon während der Masterarbeit begann und nun schon über vier Jahre andauert. Von ihm habe unendlich viel gelernt, im Labor und außerhalb. Glücklicherweise hat er mich für Experimente ermuntert, auch wenn es so wirkte, als werde es nie funktionieren.

Des Weiteren möchte ich mich bei Prof. Ferenc Krausz bedanken, der mir die außergewöhnliche Möglichkeit gab, in seiner Gruppe zu forschen und mich über die ganze Zeit unterstützt hat. Er hatte in zahlreichen Diskussionen immer wieder geniale Ideen, die die Experimente signifikant voranbrachten.

Mein nächster Dank gilt Julia Gessner, die das Magnetismus Experiment vorangetrieben hat und sehr großen Anteil an dessen Gelingen hatte. Danke für die Unterstützung im Labor, die Diskussionen über die Ursache des XMCD Effekt und die Schnittmasken.

Ein weiterer extrem großer Dank gilt Dr. Marcus Ossiander, der mir schon während meiner Masterarbeit mit Rat und Tat zur Seite stand. Für seine unzähligen ausführlichen Erklärungen, seine Unterstützung in Software Fragen (LabView, Matlab, ...) und seine schier endlose Geduld, nicht nur beim Korrekturlesen dieser Arbeit.

Außerdem möchte mich bei Prof. Markus Münzenberg bedanken, für die Zusammenarbeit und die zahlreichen Erklärungen über Magnetismus, sondern auch dafür, dass er sich freundlicherweise bereit erklärte, die Arbeit als Zweitgutachter, zu beurteilen.

Darüber hinaus ein Dank an Dr. Sangeeta Sharma und Prof. Kazuhiro Yabana für die Rechnungen und die Zusammenarbeit, sowie die Physik, die ich von ihnen lernen durfte.

Vielen Dank an Dr. Florian Lackner für die gute Zusammenarbeit und die tollen Nanopartikel.

Danke Keyhan, für die Hilfe im Labor, deine Erklärungen und die Kirschen.

Als nächstes ein Dank an die ehemaligen Masterstudenten Yi-Ping, Tobi und Malte, die mir die Arbeit im Labor erleichtert haben und großen Einfluss auf den Fortschritt der Experimente hatten.

Danke auch an die Techniker Harald Hass für die ein oder andere Reparatur kaputter Elektronik und Martin Triphan für die häufig spontan benötigte Hilfe.

Und ein ganz herzlicher Dank an alle auch ehemaligen (Büro-)Kollegen, mit denen ich während der letzten Jahre viel Zeit verbracht habe und die immer für ein angenehmes Arbeitsklima sorgten: Kevin, Lukas, Simon, Enrico, Matt, Qasim, Vlad, Nick, Moritz, Clemens, Dima, Mihail, Yang, Yik-Long, Shuba, und alle die ich vergessen habe.

Ich möchte mich bei all meinen Freunden bedanken, ganz besonders bei Noack und Jared, sowie dem RCU. Außerdem bei allen anderen die mich privat während der Doktorarbeit unterstützt haben.

Als letztes möchte ich mich bei meiner Familie bedanken, bei meiner Schwester Valerie, sowie meinen Eltern, Heidi und Marco, ohne Euch wäre das alles nicht möglich gewesen. Danke.